Techniques for Carotid Artery Feature Characterization for Cardiovascular Disease Risk Assessment using Ultrasound Elastography

By

Maxwell J. Kiernan

A dissertation submitted in partial fulfillment of the requirements

for the degree of

Doctor of Philosophy

(Medical Physics)

At the

UNIVERSITY OF WISCONSIN-MADISON

2025

Date of final oral examination: June 9th, 2025

The dissertation is approved by the following members of the Final Oral Committee:

Tomy Varghese, Professor, Department of Medical Physics.

Carol Mitchell, Assistant Professor, Department of Medicine

Bryan Bednarz, Professor, Medical Physics

Michael Speidel, Professor, Department of Medical Physics

Ivan Rosado-Mendez, Assistant Professor, Department of Medical Physics

Acknowledgments

This dissertation would not have been possible without the support and guidance of many individuals, to whom I am immensely grateful.

First, I would like to express my deepest gratitude to my advisor, Dr. Tomy Varghese, for giving me the opportunity to pursue my doctoral studies and introducing me to the fascinating field of ultrasound strain imaging. His mentorship, encouragement, and unwavering support have been invaluable to my academic and professional growth, guiding me through the complexities of technical writing and the publication process. His unwavering support and encouragement have been essential to my academic and professional growth.

I would like to sincerely thank Dr. Carol Mitchell for her continuous support and invaluable crucial insights into the clinical aspects of my research. Her expertise and guidance were instrumental in broadening my understanding of the clinical relevance of strain imaging. Dr. Mitchell's dedication to the clinical research study, including data stewardship, scanning countless volunteers, and performing manual segmentations for training the machine learning models, was truly extraordinary. I would also like to thank Erica Fletcher for assisting with some of the segmentations, thus contributing to the success of this project.

My sincere appreciation goes to Dr. Rashid Al Mukaddim for laying the groundwork with segmentation models before my arrival and for providing excellent documentation, making it easier for me to get started. His willingness to discuss ideas, troubleshoot issues, and offer guidance throughout my research has been a tremendous help.

I am grateful to Amber Possell for her cooperation in scanning volunteers in WIMR, as well as to Holly Hage, the study coordinator, for her exceptional organizational skills and dedication to the

volunteer study. I would also like to extend my thanks to everyone who has been part of the study, both current and past members, whose hard work and commitment made this research possible.

I extend my thanks to Dr. Timothy Hess for his invaluable assistance with biostatistical analyses, comparing strain and cardiovascular risk factors. His expertise greatly enriched the analytical components of this work.

I would like to acknowledge my fellow lab members Yurim Lee, Yimeng Dou, and Zhiwei Zhang for their camaraderie, collaboration, and friendship throughout my time in the lab. Their support, along with their help in data collection, made the lab an engaging and productive environment.

To my parents, John and Michelle Kiernan, thank you for your endless love, support, and encouragement throughout my academic journey. Your belief in me has been my foundation, and I am forever grateful.

I wish to express my gratitude to my great-aunt, Susan Robillard, for her generosity in allowing me to stay with her during my time in Madison. Her support and kindness made my experience more enjoyable and less stressful.

I am also deeply grateful to all of my family for their unwavering support, encouragement, and belief in me throughout my academic journey.

Finally, I would like to honor my late grandfather, Dr. Donald F. Kiernan, who was the last Dr. Kiernan before me. The dedication, integrity, and passion he showed in his work served as an inspiring example. His legacy continues to motivate me, and I strive to carry forward his spirit of curiosity and commitment through my own journey.

To all of those who have supported me along the way—thank you. This accomplishment is as much yours as it is mine.

Abstract

The goal of this dissertation is to develop and evaluate ultrasound-based methods for assessing carotid artery strain and its association with cardiovascular disease (CVD) risk. Cardiovascular disease is a leading cause of morbidity and mortality worldwide, with atherosclerosis playing a significant role in its progression. Carotid artery intima-media thickness (CIMT) and arterial wall stiffness are established indicators of cardiovascular health, and ultrasound strain imaging has emerged as a noninvasive tool to evaluate changes in arterial mechanics associated with atherosclerosis.

This work presents methods to automatically perform carotid segmentations using a Mask R-CNN network trained on manually segmented sonographer data. Accurate carotid segmentation is essential for developing advanced techniques to quantify plaque stability and vessel wall strain. Our proposed model achieved a mean bounding box intersection over union (IoU) of 0.81 and a mean lumen segmentation IoU of 0.75, using a single-channel B-mode training input. Errors primarily occurred when the jugular vein was more prominent than the carotid artery in the B-mode image, highlighting the need for more diverse training data. Automatic lumen and plaque segmentation facilitates efficient processing of high-resolution strain estimations and lays the groundwork for developing automated CVD risk assessment.

Additionally, this dissertation investigates the relationship between carotid strain indices and CVD risk factors in both healthy volunteers and patients with carotid atherosclerosis. In a cohort of healthy individuals, age, systolic blood pressure, and hemoglobin A1c were significantly associated with axial and shear strain, suggesting early mechanical changes in the arterial wall. In a separate cohort of volunteers, 25% of whom had carotid atherosclerosis, strain indices were

significantly reduced compared to non-atherosclerotic individuals, consistent with increased arterial stiffness.

Our findings demonstrate that carotid strain imaging is a promising tool for evaluating arterial stiffness and its association with cardiovascular risk. The combination of automated carotid wall/ plaque segmentation and strain analysis could improve CVD risk stratification and contribute to more targeted prevention strategies.

Table of Contents

Table of Figures

List of Tables

Chapter 1: Introduction

1.1 Background and Motivation

Cardiovascular and cerebrovascular diseases are leading causes of morbidity and mortality worldwide, with atherosclerosis being the most prevalent systemic vascular disease and a significant contributor to these conditions.[1, 2] Among cerebrovascular diseases, ischemic stroke—often resulting from plaque-related complications—is the most common.[3] Carotid atherosclerosis, characterized by the presence of plaque within the carotid arteries, is considered a major risk factor for ischemic stroke. This risk arises because the plaque may either obstruct cerebral blood flow, leading to hypoperfusion, or become unstable, releasing emboli that can occlude cerebral vessels and cause hypoxic damage to brain tissue.

Carotid ultrasound is a commonly used imaging modality to evaluate plaque presence, characteristics (such as echogenicity and surface features), and percent stenosis, thereby informing clinical decision-making in carotid disease management.[2, 4, 5] An advanced application of carotid ultrasound is ultrasound elastography, which quantifies tissue strain and deformation, offering insight into plaque stability.[6-9]

Our research group utilizes the ultrasound elastography protocol with Lagrangian strain estimation detailed by McCormick et al. (2012)[10] and adapted for GPU acceleration by Meshram et al. (2018)[11] to calculate the strain distribution and obtain quantitative strain indices on manually segmented plaque.

Increased strain within plaques, often associated with softer, echolucent tissue, indicates a higher risk of rupture.[9, 12-14] This correlation is further supported by intravascular ultrasound (IVUS) elastography studies of coronary arteries, which demonstrate that plaques exhibiting higher strain

are typically more vulnerable, particularly those composed of fatty rather than fibrous or calcific tissue.[15, 16] Moreover, thin-cap fibroatheromas, characterized by high-strain regions, are often associated with macrophage infiltration, marking them as prone to rupture.[15, 16]

In arterial segments without evident plaque, lower strain values, indicating stiffer arterial walls, are linked to inflammation and may serve as potential sites for future plaque development.[17] Quantifying strain accurately requires precise segmentation of the arterial wall and plaque from ultrasound B-mode images, tracked throughout the cardiac cycle.[18] The current methodology relies on manual segmentation by trained sonographers, which is time-consuming and limits the ability to conduct extensive analysis, especially among populations not already identified as high risk.[19]

To address this limitation, this dissertation aims to develop a robust and automated method for accurately segmenting plaque and vessel walls in longitudinal ultrasound images derived from radiofrequency (RF) data. The proposed approach will enable the efficient generation of quantitative strain metrics, facilitating comprehensive assessments of carotid artery health and identifying characteristic patterns within a healthy population sample.

1.2 Specific Research Aims

Aim 1: Develop a method for obtaining automatic carotid plaque and vessel wall segmentations using a Mask R-CNN network. The process of manual carotid feature segmentation is a time-consuming process and must be performed by a trained sonographer. This limits the speed at which our existing strain imaging workflow can process and the amount of available datasets for analysis. We sought to identify whether a machine learning approach can

accurately segment anatomical features of the carotid artery to aid in our strain workflow, using manually segmented regions as ground truth.

Aim 2: Compare quantifiable health metrics using collected carotid intima-media thickness (CIMT) measurements versus Lagrangian strain estimation. CIMT has been used to evaluate risk for cardiovascular disease (CVD)[20, 21] and is hypothesized to represent a change in arterial wall structure due to fibromuscular hyperplasia and smooth muscle hypertrophy associated with aging and hypertension.[22] We sought to identify what the relationship between CIMT and Lagrangian strain indices in relation to CVD risk factors.

Aim 3: Identify clinically relevant trends using collected strain metrics alongside demographic and health data collected from volunteer scans. We hypothesized that in individuals with atherosclerosis, arterial wall strain should decrease with atherosclerosis as the vessel stiffens due to arterial remodeling and plaque buildup. We sought to identify trends between carotid vessel wall strain and CVD risk factors in a dataset of healthy volunteers, using statistical analysis, and explored the use of Lagrangian strain indices in assessing CVD risk using an XGBoost machine leaning model.

1.3 Dissertation Outline

This dissertation is structured to explore the development and validation of a novel cardiovascular risk assessment metrics using Lagrangian strain indices derived from ultrasound imaging. The following chapters provide a comprehensive review of relevant literature, detailed methodologies, and analytical results to establish the utility of strain indices in cardiovascular risk prediction.

Chapter 2, the Literature Review, outlines the current state of knowledge regarding cardiovascular disease (CVD), including its prevalence, risk factors, and commonly used predictive models. It

also discusses atherosclerosis, covering its prevalence, pathophysiology, and treatment options. Furthermore, it reviews existing ultrasound-based techniques for assessing CVD risk, such as intima-media thickness (IMT), grayscale median analysis, and Doppler ultrasound imaging. The chapter concludes by examining ultrasound elastography, focusing on carotid strain estimation and its relationship to vascular pathophysiology.

Chapter 3 presents methodologies for automatic carotid feature segmentation with a focus on deep learning techniques. The chapter details semi-automatic and automatic segmentation methods, highlighting the use of the Mask R-CNN architecture for carotid lumen and plaque segmentation. Results include performance comparisons between lumen and plaque segmentation approaches, with statistical analysis of the segmentation accuracy.

Chapter 4 compares carotid intima-media thickness measurements with Lagrangian strain estimation to evaluate their effectiveness in assessing cardiovascular risk. The chapter outlines the motivation for using strain estimation and provides statistical correlations between IMT, strain indices, and known cardiovascular risk factors.

Chapter 5 investigates the potential of Lagrangian strain indices to assess arterial stiffness in carotid atherosclerosis. It examines strain as a surrogate for vessel compliance and an indicator of arterial remodeling.

Chapter 6 explores the relationship between hypertension and Lagrangian strain indices, focusing on how strain measurements can differentiate between atherosclerotic changes and cardiovascular risk factors in a volunteer dataset.

Chapter 7 details the development of explainable artificial intelligence (xAI) models incorporating Lagrangian strain indices for cardiovascular disease risk prediction. Utilizing XGBoost and

random forest algorithms, the chapter evaluates the performance of models designed to predict plaque presence and estimate the 10-year ASCVD risk score incorporating strain indices.

Finally, Chapter 8 summarizes the research contributions, discusses future work, and highlights related publications, including conference presentations and peer-reviewed articles.

1.4 References

[1] C. Stefanadis, C. K. Antoniou, D. Tsiachris, and P. Pietri, "Coronary Atherosclerotic Vulnerable Plaque: Current Perspectives," *J Am Heart Assoc,* vol. 6, no. 3, 03 17, 2017.

[2] A. J. Lusis, "Atherosclerosis," *Nature,* vol. 407, no. 6801, pp. 233-41, Sep 14, 2000.

[3] C. W. Tsao, A. W. Aday, Z. I. Almarzooq, A. Alonso, A. Z. Beaton, M. S. Bittencourt, A. K. Boehme, A. E. Buxton, A. P. Carson, Y. Commodore-Mensah, M. S. V. Elkind, K. R. Evenson, C. Eze-Nliam, J. F. Ferguson, G. Generoso, J. E. Ho, R. Kalani, S. S. Khan, B. M. Kissela, K. L. Knutson, D. A. Levine, T. T. Lewis, J. Liu, M. S. Loop, J. Ma, M. E. Mussolino, S. D. Navaneethan, A. M. Perak, R. Poudel, M. Rezk-Hanna, G. A. Roth, E. B. Schroeder, S. H. Shah, E. L. Thacker, L. B. VanWagner, S. S. Virani, J. H. Voecks, N.-Y. Wang, K. Yaffe, and S. S. Martin, "Heart Disease and Stroke Statistics—2022 Update: A Report From the American Heart Association," *Circulation,* vol. 145, no. 8, pp. e153-e639, 2022.

[4] P. N. T. Wells, "Current status and future technical advances of ultrasonic imaging," *IEEE Engineering in Medicine and Biology Magazine,* vol. 19, no. 5, pp. 14-20, 2000.

[5] G. L. ten Kate, E. J. Sijbrands, D. Staub, B. Coll, F. J. ten Cate, S. B. Feinstein, and A. F. Schinkel, "Noninvasive imaging of the vulnerable atherosclerotic plaque," *Curr Probl Cardiol,* vol. 35, no. 11, pp. 556-91, Nov, 2010.

[6] C. L. de Korte, S. Fekkes, A. J. Nederveen, R. Manniesing, and H. R. Hansen, "Review: Mechanical Characterization of Carotid Arteries and Atherosclerotic Plaques," *IEEE Trans Ultrason Ferroelectr Freq Control,* vol. 63, no. 10, pp. 1613-1623, 10, 2016.

[7] G. Geroulakos, G. Ramaswami, A. Nicolaides, K. James, N. Labropoulos, G. Belcaro, and M. Holloway, "Characterization of symptomatic and asymptomatic carotid plaques using high-resolution real-time ultrasonography," *Br J Surg,* vol. 80, no. 10, pp. 1274-7, Oct, 1993.

[8] N. H. Meshram, T. Varghese, C. C. Mitchell, D. C. Jackson, S. M. Wilbrand, B. P. Hermann, and R. J. Dempsey, "Quantification of carotid artery plaque stability with multiple region of interest based ultrasound strain indices and relationship with cognition," *Phys Med Biol,* vol. 62, no. 15, pp. 6341-6360, Jul 17, 2017.

[9] X. Wang, D. C. Jackson, C. C. Mitchell, T. Varghese, S. M. Wilbrand, B. G. Rocque, B. P. Hermann, and R. J. Dempsey, "Classification of Symptomatic and Asymptomatic Patients with and without Cognitive Decline Using Non-invasive Carotid Plaque Strain Indices as Biomarkers," *Ultrasound Med Biol,* vol. 42, no. 4, pp. 909-18, Apr, 2016.

[10] M. McCormick, T. Varghese, X. Wang, C. Mitchell, M. A. Kliewer, and R. J. Dempsey, "Methods for robust in vivo strain estimation in the carotid artery," *Phys Med Biol,* vol. 57, no. 22, pp. 7329-53, Nov 21, 2012.

[11] N. H. Meshram, and T. Varghese, "GPU Accelerated Multilevel Lagrangian Carotid Strain Imaging," *IEEE Trans Ultrason Ferroelectr Freq Control,* vol. 65, no. 8, pp. 1370-1379, Aug, 2018.

[12] N. H. Meshram, D. Jackson, T. Varghese, C. C. Mitchell, S. M. Wilbrand, R. J. Dempsey, and B. P. Hermann, "A Cross-Sectional Investigation of Cognition and Ultrasound-Based Vascular Strain Indices," *Arch Clin Neuropsychol,* vol. 35, no. 1, pp. 46-55, Jan 24, 2019.

[13] M. H. Roy Cardinal, M. H. G. Heusinkveld, Z. Qin, R. G. P. Lopata, C. Naim, G. Soulez, and G. Cloutier, "Carotid Artery Plaque Vulnerability Assessment Using Noninvasive Ultrasound Elastography: Validation With MRI," *AJR Am J Roentgenol,* vol. 209, no. 1, pp. 142-151, Jul, 2017.

[14] A. A. Khan, S. Sikdar, T. Hatsukami, J. Cebral, M. Jones, J. Huston, G. Howard, and B. K. Lal, "Noninvasive characterization of carotid plaque strain," *J Vasc Surg,* vol. 65, no. 6, pp. 1653-1663, Jun, 2017.

[15] C. L. de Korte, J. A. Schaar, F. Mastik, P. W. Serruys, and A. F. van der Steen, "Intravascular elastography: from bench to bedside," *J Interv Cardiol,* vol. 16, no. 3, pp. 253-9, Jun, 2003.

[16] R. A. Baldewsing, J. A. Schaar, C. L. de Korte, F. Mastik, P. W. Serruys, and A. F. van der Steen, "Intravascular Ultrasound Elastography: A Clinician's Tool for Assessing Vulnerability and Material Composition of Plaques," *Stud Health Technol Inform,* vol. 113, pp. 75-96, 2005.

[17] J. C. Kohn, M. C. Lampi, and C. A. Reinhart-King, "Age-related vascular stiffening: causes and consequences," *Front Genet,* vol. 6, pp. 112, 2015.

[18] N. H. Meshram, C. C. Mitchell, S. Wilbrand, R. J. Dempsey, and T. Varghese, "Deep Learning for Carotid Plaque Segmentation using a Dilated U-Net Architecture," *Ultrason Imaging,* vol. 42, no. 4-5, pp. 221-230, 2020 Jul-Sep, 2020.

[19] M. Xie, Y. Li, Y. Xue, L. Huntress, W. Beckerman, S. Rahimi, J. Ady, and U. Roshan, "Vessel lumen segmentation in carotid artery ultrasounds with the U-Net convolutional neural network." pp. 2680-2684.

[20] M. C. Tattersall, A. Gassett, C. E. Korcarz, A. D. Gepner, J. D. Kaufman, K. J. Liu, B. C. Astor, L. Sheppard, R. A. Kronmal, and J. H. Stein, "Predictors of carotid thickness and plaque progression during a decade: the Multi-Ethnic Study of Atherosclerosis," *Stroke,* vol. 45, no. 11, pp. 3257-62, Nov, 2014.

[21] J. Andersson, J. Sundström, T. Gustavsson, J. Hulthe, A. Elmgren, K. Zilmer, M. Zilmer, and L. Lind, "Echogenecity of the carotid intima-media complex is related to cardiovascular risk factors, dyslipidemia, oxidative stress and inflammation: the Prospective Investigation of the Vasculature in Uppsala Seniors (PIVUS) study," *Atherosclerosis,* vol. 204, no. 2, pp. 612-8, Jun, 2009.

[22] P. Greenland, J. Abrams, G. P. Aurigemma, M. G. Bond, L. T. Clark, M. H. Criqui, J. R. Crouse, L. Friedman, V. Fuster, D. M. Herrington, L. H. Kuller, P. M. Ridker, W. C. Roberts, W. Stanford, N. Stone, H. J. Swan, K. A. Taubert, and L. Wexler, "Prevention Conference V: Beyond secondary prevention: identifying the high-risk patient for primary prevention: noninvasive tests of atherosclerotic burden: Writing Group III," *Circulation,* vol. 101, no. 1, pp. E16-22, Jan 04, 2000.

Chapter 2: Literature Review

2.1 Cardiovascular Disease

2.1.1 Prevalence

Cardiovascular disease (CVD) is the leading cause of death globally, accounting for approximately 20 million deaths annually. In 2019, an estimated 17.9 million people died from CVD, representing 32% of all global deaths.[1] Of these deaths, 85% were attributable to heart attack and stroke. Recent studies indicate that the number of deaths caused by CVD has been increasing over the years. For instance, global death due to CVD increased from 12.4 million in 1990 to 19.8 million in 2022, reflecting global population growth and aging.[2]

The global burden of cardiovascular disease (CVD) is significant in both developed and developing countries, though the contributing factors vary. In high-income countries, the increasing proportion of elderly individuals elevates CVD risk, as aging is a primary risk factor. A recent study suggested that 60% of the 10-year predicted atherosclerotic CVD risk was attributed to aging alone.[3] Additionally, high-income regions often experience sedentary behaviors, which are linked to increased CVD risk. Sedentary behavior and physical inactivity are among the leading modifiable risk factors worldwide for cardiovascular disease and all-cause mortality.[4] For low and middle-income countries (LMICs), urbanization has led to lifestyle changes, such as reduced physical activity and dietary shifts, increasing CVD risk. Factors like urbanization, globalization, westernization, and industrialization result in the emergence of modern risks due to lifestyle changes (e.g., physical inactivity, obesity, other diet-related factors, and smoking and alcohol-related risks) that are strong behavioral risk factors and increase the incidence and burden of CVDs in LMICs.[5] Inadequate healthcare infrastructure in LMICs also hamper effective CVD prevention and management. The persistently high prevalence of CVD in LMICs largely reflects

the burden of key risk factors, including hypertension, tobacco use, dietary factors, and limited access to healthcare.[6]

In the United States alone, nearly half of all adults are estimated to have some form of CVD, including coronary artery disease (CAD), heart failure, and stroke.[7] This high prevalence is mirrored in Europe and parts of Asia, albeit with regional variations influenced by lifestyle, genetics, and healthcare infrastructure. Efforts to curb this trend have focused on early detection and lifestyle interventions, but challenges persist due to socioeconomic disparities and the complex interplay of risk factors.[8]

2.1.2 Risk Factors

Cardiovascular diseases are associated with a wide range of modifiable and non-modifiable risk factors. Non-modifiable factors include age, sex, family history, and genetic predisposition. The risk increases with age, making it a significant factor in the development of cardiovascular disease Men generally have a higher risk of developing CVD at an earlier age, while women's risk increases after menopause due to hormonal changes that affect lipid profiles and vascular function.[9, 10] Family history also plays a role in the genetic predisposition to heart disease, with individuals who have close relatives with CVD being at a higher risk.[11, 12]

Modifiable risk factors include hypertension, hyperlipidemia, smoking, physical inactivity, unhealthy diet, and diabetes.[13] Hypertension is one of the most significant risk factors for cardiovascular disease, as it puts additional strain on the heart and blood vessels, leading to atherosclerosis, heart failure, and stroke.[14] Similarly, elevated levels of cholesterol and triglycerides can contribute to plaque buildup in the arteries, increasing the risk of CAD. Smoking is a well-established risk factor for CVD, as it damages the endothelial cells lining blood vessels, accelerates the process of atherosclerosis, and increases the risk of blood clots.

Physical inactivity and poor diet contribute to the development of obesity, which is a major risk factor for cardiovascular diseases.[4] Obesity leads to insulin resistance, inflammation, and an increased burden on the heart, all of which promote the development of CVD. Diabetes, especially when poorly controlled, also significantly increases the risk of cardiovascular disease.[15] High blood sugar levels can damage blood vessels, leading to atherosclerosis and other cardiovascular complications. Addressing these modifiable risk factors through lifestyle changes, medication, and early interventions is crucial for preventing and managing cardiovascular disease.

In addition to these factors, psychosocial factors such as stress, depression, and socioeconomic status have been shown to influence the risk of CVD. Chronic stress can lead to elevated levels of cortisol and inflammation, both of which contribute to cardiovascular damage.[16] Depression has been linked to poor health behaviors, including lack of exercise and poor diet, which in turn increase the risk of developing CVD.[17, 18] Socioeconomic status affects access to healthcare, education, and healthy lifestyle choices, making it an influential factor in the development of cardiovascular diseases.

The identification and management of risk factors are fundamental to preventing cardiovascular disease.[19] Regular screening for blood pressure, cholesterol levels, and blood glucose, combined with lifestyle modifications and pharmacological interventions, can help reduce the impact of these risk factors. Public health efforts aimed at reducing smoking, improving diet, and promoting physical activity are essential to reducing the global burden of cardiovascular diseases. [20]

In conclusion, the prevention and management of cardiovascular disease depend heavily on understanding and addressing both modifiable and non-modifiable risk factors. A multi-pronged approach, including early identification of at-risk individuals, promoting healthy lifestyle choices,

and managing underlying health conditions, is crucial in reducing the prevalence of CVD worldwide.

2.1.3 Models for Predicting Risk

Over the years, numerous models have been developed to predict the risk of cardiovascular disease in individuals. These models are based on the identification of various risk factors, and they aim to provide healthcare professionals with tools to assess an individual's likelihood of developing CVD. The Framingham Risk Score, one of the most widely used models, estimates the 10-year risk of coronary heart disease (CHD) based on factors such as age, sex, smoking status, blood pressure, cholesterol levels, and diabetes.[21, 22] It has been instrumental in guiding clinical decisions and prioritizing interventions for individuals at high risk of cardiovascular events.

Another common model is the Atherosclerotic Cardiovascular Disease (ASCVD) Risk Calculator, which is used to estimate the 10-year risk of atherosclerotic cardiovascular disease in adults aged 40-79.[23, 24] It incorporates similar risk factors as the Framingham Risk Score but includes considerations for ethnicity and other cardiovascular conditions, such as chronic kidney disease. The ASCVD model has been shown to be effective in predicting cardiovascular risk across diverse populations, making it a valuable tool in both clinical practice and research.[24]

Despite the success of these traditional risk models, they have limitations. These models rely heavily on population-level data, which may not always reflect individual variations in genetics, lifestyle, and other factors.[25, 26] As a result, some individuals with elevated risk may not be accurately identified, while others who are classified as low-risk may still develop cardiovascular events. This has led to a push for more personalized and precise risk prediction tools, such as genetic risk scores,[27] which take into account individual genetic profiles and their interaction with environmental factors.

Recent advancements in machine learning and artificial intelligence (AI) have further enhanced the potential for risk prediction models.[28, 29] AI algorithms can analyze large datasets, incorporating complex variables such as imaging findings, biomarkers, and lifestyle factors, to provide more accurate and individualized risk assessments.[30] These technologies hold promise for improving the precision of cardiovascular disease prediction and enabling earlier interventions, potentially preventing adverse cardiovascular events.

In addition to risk calculators, biomarkers and imaging techniques are increasingly being integrated into cardiovascular risk prediction models.[31] Biomarkers such as C-reactive protein (CRP), N-terminal pro B-type natriuretic peptide (BNP), and lipoprotein(a) can provide additional information on an individual's cardiovascular risk, particularly when traditional risk factors are inconclusive.[32, 33] Similarly, advanced imaging technologies, including coronary artery calcium scoring [34] and cardiac magnetic resonance imaging, offer more detailed insights into an individual's cardiovascular health and can aid in refining risk predictions.

2.2 Atherosclerosis

Atherosclerosis is a chronic inflammatory disease of the arteries characterized by the buildup of plaque within the arterial walls.[35] This process is driven by the accumulation of lipids, inflammatory cells, and smooth muscle cells, which over time form atherosclerotic plaques.[36] These plaques can obstruct blood flow and contribute to the development of various cardiovascular diseases, including CAD, stroke, and peripheral artery disease. Atherosclerosis begins early in life and progresses slowly over decades, often without symptoms until significant plaque accumulation leads to major cardiovascular events such as heart attacks or strokes.

The progression of atherosclerosis involves several stages, starting with endothelial dysfunction, which is commonly triggered by risk factors like hypertension, smoking, and diabetes.[37] Vascular endothelial cells line the blood vessels and help regulate vascular tone and blood flow. When these cells are damaged, they become more permeable to low-density lipoproteins (LDL), which then accumulate in the vessel walls.[38, 39] The retained LDL particles undergo oxidation, triggering an inflammatory response that attracts immune cells, primarily macrophages, to the site. These macrophages attempt to engulf the oxidized LDL, but when they become overloaded, they transform into foam cells, contributing to the formation of fatty streaks.[39]

As the disease progresses, smooth muscle cells from the inner layers of the blood vessel wall migrate to the intima, where they proliferate and secrete extracellular matrix components, leading to the formation of a fibrous cap over the plaque.[40] The fibrous cap serves as a protective barrier, but it can also become unstable over time. If the fibrous cap ruptures, it exposes the underlying thrombogenic material, such as lipids, collagen and tissue factor (coagulation factor III),[41] to the bloodstream, leading to the formation of a blood clot (thrombus).[40, 42-45] This clot can obstruct the flow of blood to vital organs, causing myocardial infarction (heart attack) or ischemic stroke.

Atherosclerosis is influenced by various risk factors, including hyperlipidemia, hypertension, smoking, and diabetes.[46] High levels of LDL cholesterol contribute to the formation of plaque, while high blood pressure can accelerate the damage to the endothelial cells, making it easier for lipids to penetrate the vessel walls. Smoking exacerbates the process by promoting inflammation and endothelial dysfunction,[47] and diabetes increases the risk by enhancing oxidative stress and altering lipid metabolism.[15] These factors, when combined, create a perfect storm for the development of atherosclerosis and its complications.

2.2.1 Prevalence

Atherosclerosis is one of the most common underlying causes of CVD, affecting millions of people worldwide. Its occurrence increases with age, and it is estimated that nearly half of adults in developed countries show signs of the condition by middle age. However, accurately gauging how widespread atherosclerosis is can be difficult, as it often progresses silently for years before symptoms appear. Early-stage atherosclerosis may even be present in adolescents, though it typically becomes clinically significant later in life when arterial blockages lead to heart attacks, strokes, or other cardiovascular complications.

Factors such as diet, lifestyle, and genetics play a major role in how common atherosclerosis is within a population. In regions with high rates of smoking, unhealthy diets rich in saturated fats, and low physical activity, the condition tends to be more widespread.[48] In contrast, countries that implement strong public health initiatives promoting healthy habits generally experience lower incidence rates of atherosclerosis-related disease.[49] Furthermore, the global rise in obesity and type 2 diabetes has contributed to a growing number of cases, particularly among younger populations.[50]

Sex-based differences in how frequently atherosclerosis develops are also important. Men are generally affected earlier than women, due in part to the protective effects of estrogen before menopause. However, after menopause, the risk in women increases sharply, and by age 70, the proportion of men and women with atherosclerosis is roughly equal. [51, 52] This highlights the importance of sex-specific strategies for prevention and treatment, especially for women after midlife.

Ethnic background further influences how often atherosclerosis occurs. Research shows that individuals of African, Hispanic, and South Asian descent face a heightened risk, particularly when

conditions such as hypertension, diabetes, and obesity are present.[53, 54] These groups also have a higher likelihood of experiencing cardiovascular events at a younger age, due to earlier onset and faster progression of the disease. Ongoing studies continue to investigate the genetic and environmental contributors to these disparities.

Given how widespread atherosclerosis is globally, public health efforts must prioritize both prevention and early detection. Educating individuals on the benefits of a healthy lifestyle—such as balanced nutrition, regular physical activity, and smoking cessation—remains essential in lowering the burden of disease. Additionally, routine screening for risk factors like elevated blood pressure, cholesterol, and glucose can help identify at-risk individuals early, allowing for timely intervention that may prevent major cardiovascular events.[55, 56]

2.2.2 Pathophysiology

The pathophysiology of atherosclerosis involves a complex interplay of lipid accumulation, inflammation, endothelial dysfunction, and smooth muscle cell proliferation.[57] The initial stage of atherosclerosis begins with endothelial injury or dysfunction, often caused by factors like high blood pressure, smoking, or elevated cholesterol. This dysfunction makes the endothelium more permeable to lipids, particularly low-density lipoproteins (LDL), which accumulate within the arterial walls. These oxidized LDL particles trigger an inflammatory response, attracting immune cells such as monocytes and T lymphocytes to the site of injury.

Monocytes differentiate into macrophages, which attempt to engulf the oxidized LDL particles. [35] However, when macrophages become overloaded with lipids, they transform into foam cells, contributing to the formation of fatty streaks within the artery walls.[58] Over time, smooth muscle cells migrate from the medial layer of the artery to the intima, where they proliferate and secrete

extracellular matrix components such as collagen and elastin. This process leads to the formation of a fibrous cap over the developing plaque, stabilizing it and preventing its rupture.[59, 60]

As the plaque matures, the accumulation of lipids and foam cells continues to expand the lesion.[58] The fibrous cap can become weakened by ongoing inflammation, resulting in a higher risk of rupture. When the fibrous cap ruptures, the contents of the plaque, including lipids, collagen, and tissue factor, are exposed to the bloodstream, triggering the coagulation cascade.[36, 61] This leads to the formation of a thrombus or blood clot, which can obstruct blood flow and cause ischemia in downstream tissues, potentially leading to a heart attack or stroke.

Chronic inflammation plays a central role in the pathophysiology of atherosclerosis. Inflammatory mediators, such as cytokines and chemokines, are released by immune cells, endothelial cells, and smooth muscle cells, further promoting the recruitment of immune cells and the formation of foam cells. In addition, these inflammatory signals contribute to the destabilization of the fibrous cap, increasing the likelihood of plaque rupture and thrombosis. Oxidative stress, caused by the imbalance between reactive oxygen species and antioxidant defenses, also contributes to endothelial dysfunction and promotes the progression of atherosclerosis.[62, 63]

Other factors that influence the pathophysiology of atherosclerosis include the mechanical forces exerted by blood flow and the shear stress on the arterial walls.[64, 65] Regions of arteries exposed to turbulent flow are more likely to develop atherosclerotic lesions, as the disturbed flow contributes to endothelial injury and subsequent plaque formation. In contrast, laminar flow in healthy arteries helps maintain endothelial integrity and prevents the accumulation of lipids.[66]

2.2.3 Treatment

The treatment of atherosclerosis focuses on preventing the progression of plaque formation, stabilizing existing plaques to prevent rupture, and addressing the underlying risk factors that contribute to its development.[67] The primary strategy is to modify lifestyle factors and manage conditions such as hypertension, hyperlipidemia, and diabetes through the use of lifestyle interventions, including a heart-healthy diet, regular physical activity, and smoking cessation.[19, 68] These interventions not only help to reduce the risk of plaque formation but also improve the overall health of the cardiovascular system.[69]

Pharmacological treatment plays a crucial role in managing atherosclerosis, particularly in high-risk individuals. Statins, a class of drugs that lower LDL cholesterol, are commonly prescribed to reduce lipid levels and stabilize plaques. Statins also have pleiotropic effects, including reducing inflammation, improving endothelial function, and stabilizing atherosclerotic plaques, which aid in preventing cardiovascular events like heart attacks and strokes.[70] Other lipid-lowering medications such as ezetimibe, bile acid sequestrants, and proprotein convertase subtilisin/kexin type 9 (PCSK9) inhibitors may be used in patients who do not respond adequately to statins alone.[71]

For individuals with hypertension, controlling blood pressure is another key aspect of managing atherosclerosis. Antihypertensive medications, such as angiotensin-converting enzyme (ACE) inhibitors, angiotensin II receptor blockers (ARBs), and calcium channel blockers, are commonly used to lower blood pressure and reduce the strain on the arterial walls.[72] Managing blood pressure helps prevent further endothelial injury and reduces the risk of plaque rupture and thrombosis. Similarly, patients with diabetes are often treated with medications that control blood

glucose levels, as uncontrolled diabetes accelerates the development of atherosclerosis by promoting inflammation and oxidative stress.[73]

In some cases, antiplatelet drugs, such as aspirin or clopidogrel, are prescribed to reduce the risk of blood clot formation, particularly in individuals with advanced atherosclerosis or a history of cardiovascular events. These medications inhibit platelet aggregation, which helps prevent the formation of thrombi in the event of plaque rupture.[74] In patients at high risk of cardiovascular events, dual antiplatelet therapy (using both aspirin and another antiplatelet drug) may be employed, especially following procedures like stent placement or coronary artery bypass surgery.[74, 75]

When atherosclerosis becomes symptomatic or results in severe arterial blockages that impede blood flow, surgical interventions may be necessary. Percutaneous coronary intervention (PCI), which includes procedures such as angioplasty and stent placement, is commonly used to open narrowed or blocked coronary arteries.[76] These interventions help restore blood flow to the heart and relieve symptoms like chest pain (angina). In more severe cases, coronary artery bypass grafting (CABG) may be performed to bypass blocked arteries and ensure adequate blood supply to the heart muscle.[77] These procedures can significantly improve symptoms and reduce the risk of heart attacks.

2.3 Assessing Cardiovascular Disease Risk Using Ultrasound

Ultrasound imaging is a valuable tool for assessing CVD risk, offering a non-invasive, cost-effective method for evaluating the structure and function of the heart and blood vessels. Several ultrasound techniques, such as measuring intima-media thickness (IMT), grayscale median analysis, and Doppler ultrasound imaging, are widely used in clinical practice and research to

identify individuals at high risk for developing cardiovascular events. These methods assist in detecting early signs of atherosclerosis, monitor disease progression, and guide treatment decisions.

2.3.1 Intima-Media Thickness

IMT is a widely used ultrasound measurement that provides valuable information about the presence of subclinical atherosclerosis. IMT refers to the combined thickness of the intima and media layers of the arterial wall, particularly in the carotid arteries, which are easily accessible for non-invasive measurement. The thickness of these layers can increase prior to or alongside atherosclerotic plaque development, making IMT a useful marker for detecting early vascular changes associated with cardiovascular disease.[78] IMT measurements are typically performed using high-frequency ultrasound, which provides high-resolution images of the carotid artery and allows for accurate assessment of wall thickness.

Several studies have demonstrated that increased IMT is associated with an elevated risk of cardiovascular events, such as myocardial infarction, stroke, and peripheral artery disease.[79-81] IMT is considered a predictor of both total cardiovascular risk and the risk of specific cardiovascular events. It has been shown that individuals with increased IMT are more likely to have significant atherosclerotic changes in other arteries and are at greater risk for developing clinical CVD later in life.[82] As a result, IMT measurement has been incorporated into risk stratification algorithms to identify individuals at high risk of cardiovascular events, even in the absence of symptoms.

IMT measurement is particularly valuable for assessing individuals who may not yet exhibit overt signs of cardiovascular disease but are at risk due to other factors such as hypertension, diabetes, smoking, or a family history of heart disease. By detecting increased IMT early, clinicians can

intervene with lifestyle modifications and pharmacological treatments to reduce the risk of future cardiovascular events.[80, 83] Through this approach IMT measurement serves as an early-warning system, allowing for proactive management of cardiovascular risk.

However, there are some limitations to IMT measurement. The technique is highly operator-dependent, meaning that the accuracy of measurements can vary based on the experience and skill of the ultrasound technician.[84, 85] Additionally, IMT may not capture all aspects of plaque burden, as it primarily reflects changes in the arterial wall thickness rather than the actual size or composition of plaques.[86] While IMT is a useful tool for detecting early atherosclerosis, it should be used in conjunction with other imaging techniques or risk assessments to provide a more complete evaluation of cardiovascular health.

Despite these limitations, IMT remains a widely accepted and valuable method for assessing cardiovascular risk.[87] It is a simple, non-invasive procedure that can be performed in outpatient settings and provides valuable insights into early vascular changes that may signal the onset of atherosclerosis. In combination with other risk factors and diagnostic tools, IMT measurement can help identify individuals at high risk for cardiovascular disease and guide treatment decisions.

2.3.2 Grayscale Median Analysis

Grayscale median (GSM) analysis is an advanced ultrasound technique used to assess the composition and stability of atherosclerotic plaques, providing deeper insights into the quality of arterial plaques beyond simple thickness measurements. GSM analysis quantifies the texture of the plaque by evaluating the distribution of grayscale values in ultrasound images, with lower GSM values indicating softer, more vulnerable plaques, and higher GSM values representing denser, more stable plaques.[88] This technique has emerged as a promising tool in cardiovascular

risk assessment because it can help predict plaque rupture, a key event in acute cardiovascular incidents like heart attacks and strokes.[89]

The principle behind GSM analysis lies in the correlation between plaque composition and grayscale intensity. Atherosclerotic plaques are heterogeneous, with areas of fibrous tissue, calcification, and lipid-rich necrotic cores. These components have different echogenic properties, leading to variations in grayscale values in ultrasound images. By analyzing these grayscale values, GSM analysis provides a quantitative measure of plaque stability, allowing clinicians to identify potentially dangerous plaques that are more likely to rupture and cause thrombosis.[88, 90] This capability adds a layer of sophistication to ultrasound imaging, complementing traditional methods such as intima-media thickness measurement.

Several studies have demonstrated the clinical value of GSM analysis in predicting cardiovascular events. Research has shown that lower GSM values are associated with an increased risk of plaque rupture and subsequent cardiovascular events, such as myocardial infarction and stroke.[88, 90, 91] GSM analysis, when used in conjunction with other risk assessment tools, has been shown to improve the predictive accuracy of cardiovascular disease models.[89] By identifying plaques that are more likely to rupture, GSM analysis can help clinicians target high-risk patients for more aggressive management, including the use of statins, antiplatelet therapy, or interventional procedures like stent placement.

One potential benefit of Gray-Scale Median (GSM) analysis is its ability to characterize plaque composition non-invasively using widely available ultrasound imaging. Compared to modalities like MRI or CT, ultrasound is more accessible and cost-effective, making GSM a practical option in routine clinical workflows—particularly in primary care or screening settings where early identification of potentially vulnerable plaques can aid preventive cardiovascular care [92,93].

GSM can also be integrated into standard carotid ultrasound protocols and reviewed during or after acquisition, offering clinicians an efficient way to extract compositional information.

However, GSM analysis is not without limitations. Its reliability is influenced by factors such as scanner settings, gain calibration, and image acquisition technique, all of which can vary between systems and operators. This user- and machine-dependence introduces variability that can affect the consistency and reproducibility of measurements across different sites or studies [94]. Additionally, while GSM offers insight into plaque echogenicity, a proxy for composition, it does not directly assess other contributors to plaque vulnerability, such as inflammation, fibrous cap integrity, or local hemodynamics [95]. Therefore, GSM results should be interpreted in the context of a broader diagnostic framework when evaluating cardiovascular risk.

2.3.3 Doppler Ultrasound Imaging

Doppler ultrasound imaging is a widely used technique for assessing blood flow dynamics and detecting abnormalities in the vasculature, making it an important tool in the evaluation of cardiovascular disease.[96] By measuring the velocity and direction of blood flow, Doppler ultrasound can provide critical information about the presence of arterial blockages, stenosis, and other flow-related abnormalities.[97] The technique relies on the Doppler effect, which occurs when sound waves are reflected off moving blood cells, allowing clinicians to visualize blood flow patterns in real-time and detect changes that may signal the presence of cardiovascular disease.[98]

Doppler ultrasound can detect changes in blood flow velocity that occur as a result of stenosis. When the artery is narrowed, blood flow becomes turbulent and the velocity of increases. Doppler ultrasound can measure these changes in velocity and provide an estimate of the degree of stenosis, which is crucial for determining the appropriate treatment strategy.[99, 100] By analyzing the blood flow patterns, clinicians can assess the functional impact of atherosclerosis on the

cardiovascular system and determine the need for interventions such as angioplasty, bypass surgery, or lifestyle changes.[100] Doppler ultrasound can also be used to monitor changes in blood flow over time, providing valuable information about disease progression and treatment effectiveness.

Additionally, Doppler ultrasound is used to evaluate the risk of thromboembolism, a condition in which blood clots form in the arteries and travel to other parts of the body. Thromboembolism is a major complication of atherosclerosis, as ruptured plaques can lead to the formation of blood clots, which may obstruct blood flow to vital organs.[101] Doppler ultrasound can detect signs of clot formation, such as reduced or absent blood flow in certain areas, and can help guide decisions about the use of anticoagulant therapy to prevent thromboembolic events.[102]

However, Doppler ultrasound does have some limitations. The technique is highly operator-dependent, and accurate measurements require skilled technicians who are trained in interpreting blood flow patterns.[103] Additionally, Doppler ultrasound may not be as effective in assessing smaller vessels or in patients with severe obesity, where imaging quality can be compromised.[104, 105] Despite these challenges, Doppler ultrasound remains an invaluable tool in cardiovascular disease assessment, particularly for evaluating blood flow, detecting stenosis, and guiding therapeutic interventions.

2.4 Ultrasound Elastography for Assessing Risk

2.4.1 Basic Principles

The basic principle behind ultrasound elastography is the combination of high-frequency ultrasound imaging with elastography, a technique that measures the mechanical deformation of the arterial wall.[106] Ultrasound imaging is used to visualize the structure of the arterial wall,

while elastography tracks the changes in the shape and strain of the wall during the cardiac cycle. The arterial wall undergoes periodic stretching and recoil with each heartbeat, driven by the pulsatile flow of blood. These deformations, or strains, are measured in real time using ultrasound, which can track the movement of the vessel wall as it responds to the pressure generated by the pumping heart.

Elastography allows for the quantification of strain and elasticity in the arterial wall by recording the deformation of the artery during systole and diastole. The changes in the shape of the artery are measured by the ultrasound system, which calculates strain by comparing the positions of the vessel wall during the different phases of the cardiac cycle. By analyzing these changes, clinicians can calculate key biomechanical indices, such as pulse wave velocity (PWV), which reflects the speed at which the pressure wave generated by the heart travels through the arterial system. A faster PWV indicates greater arterial stiffness, which is associated with an increased risk of cardiovascular disease.[107]

Ultrasound elastography involves the measurement of vascular strain, which is the relative deformation of the arterial wall in response to the pulsatile blood flow. Strain is an important indicator of arterial elasticity, with greater strain corresponding to greater arterial compliance.[108] Reduced strain, on the other hand, suggests stiffened arteries, which are less capable of expanding and contracting with the heartbeat. This loss of elasticity is one of the key features of atherosclerosis and other forms of vascular disease, making the measurement of strain an important aspect of cardiovascular risk assessment.[109] Strain measurements can be used to assess the mechanical properties of the arteries, providing valuable information about their health and function.

Another important principle of ultrasound elastography is the ability to assess endothelial function, which plays a critical role in vascular health. Endothelial cells line the blood vessels and regulate vascular tone by releasing substances that cause the blood vessels to dilate or constrict. In healthy arteries, endothelial cells respond to stimuli such as changes in blood pressure or shear stress by releasing nitric oxide, a potent vasodilator. Ultrasound elastography can measure changes in arterial diameter in response to these stimuli, providing an indication of endothelial function. Impaired endothelial function is an early sign of cardiovascular disease and is associated with an increased risk of atherosclerosis and other vascular disorders.

2.4.2 Carotid Strain Estimation

Carotid strain estimation involves measuring the deformation of carotid artery walls during the cardiac cycle. Reduced strain is indicative of increased arterial stiffness, a hallmark of early vascular aging and a predictor of adverse cardiovascular events.[110] This metric complements traditional risk factors and provides additional prognostic value.

Carotid strain estimation is a key application of ultrasound elastography, focusing on the assessment of the mechanical properties of the carotid artery. The carotid artery is a major vessel that supplies blood to the brain, and changes in its elasticity are strongly correlated with overall cardiovascular health. Carotid strain is a measure of the deformation of the carotid artery wall in response to the pulsatile blood flow driven by each heartbeat. This strain is influenced by factors such as arterial stiffness, endothelial function, and the presence of atherosclerotic plaques, making carotid strain estimation a valuable indicator of cardiovascular risk. [47, 111-118]

The measurement of carotid strain is performed using high-resolution ultrasound, which allows for precise tracking of the arterial wall as it expands and contracts during the cardiac cycle. The strain is calculated by comparing the arterial diameter during systole (when the heart pumps blood)

and diastole (when the heart relaxes). The degree of strain is inversely related to arterial stiffness; in healthy arteries, the strain is greater because the walls are more elastic and can expand and contract more easily. Conversely, stiffened arteries exhibit reduced strain, indicating decreased compliance and increased cardiovascular risk.[108, 119, 120]

Carotid strain estimation is particularly useful for detecting early signs of vascular dysfunction before the onset of overt cardiovascular disease. By identifying individuals with reduced carotid strain, clinicians can intervene early with lifestyle modifications and pharmacological treatments aimed at improving arterial health.[121] In patients with risk factors such as hypertension, diabetes, or a family history of cardiovascular disease, carotid strain estimation can help assess the impact of these risk factors on the arterial wall and guide preventive strategies.

Several studies have shown that carotid strain is a useful predictor of cardiovascular events, such as stroke and myocardial infarction.[112, 117] Reduced carotid strain has been associated with an increased risk of plaque rupture, thrombosis, and other cardiovascular complications. By measuring carotid strain, ultrasound elastography can help identify individuals who are at high risk for these events, even in the absence of symptoms. This early identification can lead to more aggressive risk management, such as the use of statins, antihypertensive medications, or antiplatelet therapy, to prevent adverse outcomes.

Lagrangian strain estimation was initially proposed by Shi et al. (2008)[122] and incorporated into a comprehensive approach in McCormick et al. (2012) [117]. The algorithm was then adapted for GPU acceleration by Meshram et al. (2018)[113]. The strain estimation algorithm utilizes radiofrequency (RF) data collected using an Acuson S2000/S3000 system (Siemens Ultrasound, Mountain View, CA, USA) to calculate strain distribution and quantitative strain indices within defined regions. This process relies on binary segmentations of plaque regions performed on RF-

derived B-mode images and employs a three-level pyramidal hierarchy for displacement tracking, ultimately resulting in the calculation of the Lagrangian strain tensor from the accumulated displacements. The GPU implementation is executed using an NVIDIA K40 GPU with CUDA programming, as described by Meshram et al. (2018)[113].

The hierarchical approach, as described by McCormick, [117] involves three levels, each with a different degree of decimation corresponding to a Gaussian filter with a variance of $(f/2)^2$ where (f) is the decimation factor. Higher levels of decimation are possible in the axial or beam direction due to denser image content, with broader structures being retained at higher levels, while finer structures are preserved at the lowest level, which consists of RF data. Envelope data is used at higher levels to maintain the overall structure and adhere to the Nyquist criterion. The matching blocks within each level decrease in size linearly from coarse to fine, without overlapping with neighboring blocks. This non-overlapping approach reduces computational burden and aids in regularization.

Displacement matching involves interpolating displacements at coarser levels to initialize searches at lower levels. To prevent peak-hopping errors, which occur when the correlation coefficient peaks select speckle decorrelation peaks instead of the true peak, large strain errors are generated. Pixels with strain magnitudes exceeding a 7.5% threshold are marked for replacement, with these pixels being linearly interpolated across errant regions or extrapolated from valid data near the edges.

Block scaling addresses decorrelation across frames within a block, partially due to strain. Strain at higher levels can be used to stretch or compress the matching block before cross-correlation, reducing decorrelation by resampling the matching blocks with a scaling factor and windowed-sinc interpolation. The scaling factor is adjusted based on the normal strain in the relevant

direction, particularly when strain is low, resulting in an improved strain signal-to-noise ratio (SNR).

The algorithm uses Dynamic frame skipping, where the amount of deformation between images in a sequence influences the overall SNR. Due to varying loads on the region of interest (ROI) throughout the cardiac cycle, the frame skip length must adjust according to the cardiac phase—shorter during high strain rates and longer when strain rates are low. At the lowest level, strain is estimated using a least squares gradient over a 3x3 pixel region. The strain sequence is calculated over the cardiac cycle, using the end-diastolic state as a reference. Accumulated displacement and Lagrangian strain are calculated according to a mesh created from the binary segmentation mask provided by an expert sonographer, with strain and displacement for each point interpolated and added to the accumulated values for every frame.

The visualization of strain within the vessel walls is crucial for identifying vulnerable sections that may rupture, with the plaque's composition, size, and location influencing its susceptibility. Scalar strain indices are obtained from the Lagrangian strain tensor via Eigen analysis. [117]

2.4.3 Relationship to Pathophysiology

The relationship between ultrasound elastography and the pathophysiology of cardiovascular disease is grounded in the biomechanical properties of the arterial wall and the role of arterial stiffness in disease progression. Arterial stiffness, a key feature of atherosclerosis, reflects the loss of elastic properties in the arterial wall due to the accumulation of atherosclerotic plaques, smooth muscle cell proliferation, and increased collagen deposition. As arteries become stiffer, they are less able to expand and contract with the pulsatile flow of blood, leading to increased systolic blood pressure, reduced diastolic pressure, and impaired blood flow. This mechanical dysfunction

contributes to the development of further cardiovascular complications, such as hypertension, left ventricular hypertrophy, and increased risk of ischemic events.[123]

Ultrasound elastography directly correlates with these pathophysiological changes, by measuring arterial strain and stiffness. Reduced strain, as detected by ultrasound elastography, is an early indicator of increased arterial stiffness, which is a hallmark of atherosclerosis and other vascular diseases. Additionally, ultrasound elastography can assess endothelial function, which plays a critical role in regulating vascular tone and preventing the progression of atherosclerosis. Endothelial dysfunction, often seen in conditions such as hypertension, diabetes, and hyperlipidemia, is associated with impaired vasodilation and increased risk of plaque formation.[124] By quantifying changes in arterial diameter in response to stimuli, ultrasound elastography can detect endothelial dysfunction before it leads to overt clinical disease.

The ability to measure these biomechanical properties provides a window into the early stages of cardiovascular disease, allowing for more accurate risk stratification. For example, individuals with increased arterial stiffness or impaired endothelial function are at higher risk of developing atherosclerosis and experiencing adverse cardiovascular events. By identifying these changes early, ultrasound elastography can guide preventive interventions such as lifestyle modification, pharmacotherapy, and monitoring to slow disease progression and reduce the risk of major cardiovascular events.[125]

2.5 References

[1] M. Di Cesare, P. Perel, S. Taylor, C. Kabudula, H. Bixby, T. A. Gaziano, D. V. McGhie, J. Mwangi, B. Pervan, J. Narula, D. Pineiro, and F. J. Pinto, “The Heart of the World,” *Glob Heart,* vol. 19, no. 1, pp. 11, 2024.

[2] G. A. Mensah, V. Fuster, and G. A. Roth, “A Heart-Healthy and Stroke-Free World: Using Data to Inform Global Action,” *J Am Coll Cardiol,* vol. 82, no. 25, pp. 2343-2349, Dec 19, 2023.

[3] M. C. Tsai, C. C. Lee, S. C. Liu, P. J. Tseng, and K. L. Chien, "Combined healthy lifestyle factors are more beneficial in reducing cardiovascular disease in younger adults: a meta-analysis of prospective cohort studies," *Sci Rep,* vol. 10, no. 1, pp. 18165, Oct 23, 2020.

[4] C. J. Lavie, C. Ozemek, S. Carbone, P. T. Katzmarzyk, and S. N. Blair, "Sedentary Behavior, Exercise, and Cardiovascular Health," *Circ Res,* vol. 124, no. 5, pp. 799-815, Mar, 2019.

[5] H. R. Wurie, and F. P. Cappuccio, "Cardiovascular disease in low- and middle-income countries: an urgent priority," *Ethn Health,* vol. 17, no. 6, pp. 543-50, 2012.

[6] A. D. Bowry, J. Lewey, S. B. Dugani, and N. K. Choudhry, "The Burden of Cardiovascular Disease in Low- and Middle-Income Countries: Epidemiology and Management," *Can J Cardiol,* vol. 31, no. 9, pp. 1151-9, Sep, 2015.

[7] K. E. Joynt Maddox, M. S. V. Elkind, H. J. Aparicio, Y. Commodore-Mensah, S. D. de Ferranti, W. N. Dowd, A. F. Hernandez, O. Khavjou, E. D. Michos, L. Palaniappan, J. Penko, R. Poudel, V. L. Roger, D. S. Kazi, and A. H. Association, "Forecasting the Burden of Cardiovascular Disease and Stroke in the United States Through 2050-Prevalence of Risk Factors and Disease: A Presidential Advisory From the American Heart Association," *Circulation,* vol. 150, no. 4, pp. e65-e88, Jul 23, 2024.

[8] Y. Fu, G. Yu, N. Maulana, and K. Thomson, "Interventions to tackle health inequalities in cardiovascular risks for socioeconomically disadvantaged populations: a rapid review," *Br Med Bull,* vol. 148, no. 1, pp. 22-41, Dec 11, 2023.

[9] A. Raj, S. Chakole, S. Agrawal, A. Gupta, H. Khekade, R. Prasad, T. Lohakare, and M. Wanjari, "The Impact of Menopause on Cardiovascular Aging: A Comprehensive Review of Androgen Influences," *Cureus,* vol. 15, no. 8, pp. e43569, Aug, 2023.

[10] S. R. El Khoudary, B. Aggarwal, T. M. Beckie, H. N. Hodis, A. E. Johnson, R. D. Langer, M. C. Limacher, J. E. Manson, M. L. Stefanick, M. A. Allison, A. H. A. P. S. C. o. t. C. o. E. a. Prevention, and a. C. o. C. a. S. Nursing, "Menopause Transition and Cardiovascular Disease Risk: Implications for Timing of Early Prevention: A Scientific Statement From the American Heart Association," *Circulation,* vol. 142, no. 25, pp. e506-e532, Dec 22, 2020.

[11] N. I. Parikh, S. J. Hwang, M. G. Larson, L. A. Cupples, C. S. Fox, E. S. Manders, J. M. Murabito, J. M. Massaro, U. Hoffmann, and C. J. O'Donnell, "Parental occurrence of premature cardiovascular disease predicts increased coronary artery and abdominal aortic calcification in the Framingham Offspring and Third Generation cohorts," *Circulation,* vol. 116, no. 13, pp. 1473-81, Sep 25, 2007.

[12] C. N. Taylor, D. Wang, M. G. Larson, E. S. Lau, E. J. Benjamin, R. B. D'Agostino, R. S. Vasan, D. Levy, S. Cheng, and J. E. Ho, "Family History of Modifiable Risk Factors and Association With Future Cardiovascular Disease," *J Am Heart Assoc,* vol. 12, no. 6, pp. e027881, Mar 21, 2023.

[13] D. S. Arsyad, J. Westerink, M. J. Cramer, J. Ansar, Wahiduddin, F. L. J. Visseren, P. A. Doevendans, and Ansariadi, "Modifiable risk factors in adults with and without prior cardiovascular disease: findings from the Indonesian National Basic Health Research," *BMC Public Health,* vol. 22, no. 1, pp. 660, Apr 05, 2022.

[14] J. S. Alpert, "New Coronary Heart Disease Risk Factors," *Am J Med,* vol. 136, no. 4, pp. 331-332, Apr, 2023.

[15] T. R. Einarson, A. Acs, C. Ludwig, and U. H. Panton, "Prevalence of cardiovascular disease in type 2 diabetes: a systematic literature review of scientific evidence from across the world in 2007-2017," *Cardiovasc Diabetol,* vol. 17, no. 1, pp. 83, Jun 08, 2018.

[16] M. Kivimäki, and A. Steptoe, "Effects of stress on the development and progression of cardiovascular disease," *Nat Rev Cardiol,* vol. 15, no. 4, pp. 215-229, Apr, 2018.

[17] C. Krittanawong, N. S. Maitra, Y. K. Qadeer, Z. Wang, S. Fogg, E. A. Storch, C. M. Celano, J. C. Huffman, M. Jha, D. S. Charney, and C. J. Lavie, "Association of Depression and Cardiovascular Disease," *Am J Med,* vol. 136, no. 9, pp. 881-895, Sep, 2023.

[18] J. L. Sotelo, D. Musselman, and C. Nemeroff, "The biology of depression in cancer and the relationship between depression and cancer progression," *Int Rev Psychiatry,* vol. 26, no. 1, pp. 16-30, Feb, 2014.

[19] J. M. Rippe, "Lifestyle Strategies for Risk Factor Reduction, Prevention, and Treatment of Cardiovascular Disease," *Am J Lifestyle Med,* vol. 13, no. 2, pp. 204-212, 2019.

[20] R. Ndejjo, H. Y. Hassen, R. K. Wanyenze, D. Musoke, F. Nuwaha, S. Abrams, H. Bastiaens, and G. Musinguzi, "Community-Based Interventions for Cardiovascular Disease Prevention in Low-and Middle-Income Countries: A Systematic Review," *Public Health Rev,* vol. 42, pp. 1604018, 2021.

[21] R. B. D'Agostino, S. Grundy, L. M. Sullivan, P. Wilson, and C. R. P. Group, "Validation of the Framingham coronary heart disease prediction scores: results of a multiple ethnic groups investigation," *JAMA,* vol. 286, no. 2, pp. 180-7, Jul 11, 2001.

[22] R. B. D'Agostino, R. S. Vasan, M. J. Pencina, P. A. Wolf, M. Cobain, J. M. Massaro, and W. B. Kannel, "General cardiovascular risk profile for use in primary care: the Framingham Heart Study," *Circulation,* vol. 117, no. 6, pp. 743-53, Feb 12, 2008.

[23] D. K. Arnett, A. Khera, and R. S. Blumenthal, "2019 ACC/AHA Guideline on the Primary Prevention of Cardiovascular Disease: Part 1, Lifestyle and Behavioral Factors," *JAMA Cardiol,* vol. 4, no. 10, pp. 1043-1044, Oct 01, 2019.

[24] C. D. Rodríguez-Ariza, A. Cabrera-Villamizar, A. L. Rodríguez-Pulido, S. Callegari, N. A. Ossa Rodríguez, M. Pinilla-Roncancio, S. M. Moreno López, and C. A. Sánchez-Vallejo, "External validation of the ACC/AHA ASCVD risk score in a Colombian population cohort," *Sci Rep,* vol. 13, no. 1, pp. 6139, Apr 15, 2023.

[25] I. Talha, N. Elkhoudri, and A. Hilali, "Major Limitations of Cardiovascular Risk Scores," *Cardiovasc Ther,* vol. 2024, pp. 4133365, 2024.

[26] N. J. Samani, E. Beeston, C. Greengrass, F. Riveros-McKay, R. Debiec, D. Lawday, Q. Wang, C. A. Budgeon, P. S. Braund, R. Bramley, S. Kharodia, M. Newton, A. Marshall, A. Krzeminski, A. Zafar, A. Chahal, A. Heer, K. Khunti, N. Joshi, M. Lakhani, A. Farooqi, V. Plagnol, P. Donnelly, M. E. Weale, and C. P. Nelson, "Polygenic risk score adds to a clinical risk score in the prediction of cardiovascular disease in a clinical setting," *Eur Heart J,* vol. 45, no. 34, pp. 3152-3160, Sep 07, 2024.

[27] H. Yun, N. I. Noh, and E. Y. Lee, "Genetic risk scores used in cardiovascular disease prediction models: a systematic review," *Rev Cardiovasc Med,* vol. 23, no. 1, pp. 8, Jan 11, 2022.

[28] T. Liu, A. Krentz, L. Lu, and V. Curcin, "Machine learning based prediction models for cardiovascular disease risk using electronic health records data: systematic review and meta-analysis," *European Heart Journal - Digital Health*, 2024.

[29] M. Singh, A. Kumar, N. N. Khanna, J. R. Laird, A. Nicolaides, G. Faa, A. M. Johri, L. E. Mantella, J. F. E. Fernandes, J. S. Teji, N. Singh, M. M. Fouda, R. Singh, A. Sharma, G. Kitas, V. Rathore, I. M. Singh, K. Tadepalli, M. Al-Maini, E. R. Isenovic, S. Chaturvedi, D. Garg, K. I. Paraskevas, D. P. Mikhailidis, V. Viswanathan, M. K. Kalra, Z. Ruzsa, L. Saba, A. F. Laine, D. L. Bhatt, and J. S. Suri, "Artificial intelligence for cardiovascular disease risk assessment in personalised framework: a scoping review," *EClinicalMedicine,* vol. 73, pp. 102660, Jul, 2024.

[30] Y. Cai, Y. Q. Cai, L. Y. Tang, Y. H. Wang, M. Gong, T. C. Jing, H. J. Li, J. Li-Ling, W. Hu, Z. Yin, D. X. Gong, and G. W. Zhang, "Artificial intelligence in the risk prediction models of cardiovascular disease and development of an independent validation screening tool: a systematic review," *BMC Med,* vol. 22, no. 1, pp. 56, Feb 05, 2024.

[31] M. O. Gore, C. R. Ayers, A. Khera, C. R. deFilippi, T. J. Wang, S. L. Seliger, V. Nambi, E. Selvin, J. D. Berry, W. G. Hundley, M. Budoff, P. Greenland, M. H. Drazner, C. M. Ballantyne, B. D. Levine, and J. A. de Lemos, "Combining Biomarkers and Imaging for Short-Term Assessment of Cardiovascular Disease Risk in Apparently Healthy Adults," *J Am Heart Assoc,* vol. 9, no. 15, pp. e015410, Aug 04, 2020.

[32] Y. K. Wong, and H. F. Tse, "Circulating Biomarkers for Cardiovascular Disease Risk Prediction in Patients With Cardiovascular Disease," *Front Cardiovasc Med,* vol. 8, pp. 713191, 2021.

[33] A. R. Folsom, "Classical and novel biomarkers for cardiovascular risk prediction in the United States," *J Epidemiol,* vol. 23, no. 3, pp. 158-62, 2013.

[34] M. J. Blaha, J. Yeboah, M. Al Rifai, K. Liu, R. Kronmal, and P. Greenland, "Providing Evidence for Subclinical CVD in Risk Assessment," *Glob Heart,* vol. 11, no. 3, pp. 275-285, Sep, 2016.

[35] K. Kobiyama, and K. Ley, “Atherosclerosis,” *Circ Res,* vol. 123, no. 10, pp. 1118-1120, Oct 26, 2018.

[36] J. F. Bentzon, F. Otsuka, R. Virmani, and E. Falk, “Mechanisms of plaque formation and rupture,” *Circ Res,* vol. 114, no. 12, pp. 1852-66, Jun 06, 2014.

[37] M. A. Gimbrone, and G. García-Cardeña, “Endothelial Cell Dysfunction and the Pathobiology of Atherosclerosis,” *Circ Res,* vol. 118, no. 4, pp. 620-36, Feb 19, 2016.

[38] H. Jiang, Y. Zhou, S. M. Nabavi, A. Sahebkar, P. J. Little, S. Xu, J. Weng, and J. Ge, “Mechanisms of Oxidized LDL-Mediated Endothelial Dysfunction and Its Consequences for the Development of Atherosclerosis,” *Front Cardiovasc Med,* vol. 9, pp. 925923, 2022.

[39] C. Khatana, N. K. Saini, S. Chakrabarti, V. Saini, A. Sharma, R. V. Saini, and A. K. Saini, “Mechanistic Insights into the Oxidized Low-Density Lipoprotein-Induced Atherosclerosis,” *Oxidative Medicine and Cellular Longevity,* vol. 2020, no. 1, pp. 5245308, 2020.

[40] R. Fitridge, and M. Thompson, "Mechanisms of Vascular Disease: A Reference Book for Vascular Specialists," 2011.

[41] R. Hutter, C. Valdiviezo, B. V. Sauter, M. Savontaus, I. Chereshnev, F. E. Carrick, G. Bauriedel, B. Lüderitz, J. T. Fallon, V. Fuster, and J. J. Badimon, “Caspase-3 and tissue factor expression in lipid-rich plaque macrophages: evidence for apoptosis as link between inflammation and atherothrombosis,” *Circulation,* vol. 109, no. 16, pp. 2001-8, Apr 27, 2004.

[42] L. Alonso-Herranz, J. Albarrán-Juárez, and J. F. Bentzon, “Mechanisms of fibrous cap formation in atherosclerosis,” *Front Cardiovasc Med,* vol. 10, pp. 1254114, 2023.

[43] M. Clarke, and M. Bennett, “Defining the role of vascular smooth muscle cell apoptosis in atherosclerosis,” *Cell Cycle,* vol. 5, no. 20, pp. 2329-31, Oct, 2006.

[44] P. Libby, “Mechanisms of acute coronary syndromes and their implications for therapy,” *N Engl J Med,* vol. 368, no. 21, pp. 2004-13, May 23, 2013.

[45] G. Howard, L. E. Wagenknecht, G. L. Burke, A. Diez-Roux, G. W. Evans, P. McGovern, F. J. Nieto, and G. S. Tell, “Cigarette smoking and progression of atherosclerosis: The Atherosclerosis Risk in Communities (ARIC) Study,” *Jama,* vol. 279, no. 2, pp. 119-24, Jan 14, 1998.

[46] F. Cosentino, P. J. Grant, V. Aboyans, C. J. Bailey, A. Ceriello, V. Delgado, M. Federici, G. Filippatos, D. E. Grobbee, T. B. Hansen, H. V. Huikuri, I. Johansson, P. Jüni, M. Lettino, N. Marx, L. G. Mellbin, C. J. Östgren, B. Rocca, M. Roffi, N. Sattar, P. M. Seferović, M. Sousa-Uva, P. Valensi, D. C. Wheeler, and E. S. D. Group, “2019 ESC Guidelines on diabetes, pre-diabetes, and cardiovascular diseases developed in collaboration with the EASD: The Task Force for diabetes, pre-diabetes, and cardiovascular diseases of the European Society of Cardiology (ESC) and the European

Association for the Study of Diabetes (EASD)," *European Heart Journal,* vol. 41, no. 2, pp. 255-323, 2019.

[47] S. E. Berman, X. Wang, C. C. Mitchell, B. Kundu, D. C. Jackson, S. M. Wilbrand, T. Varghese, B. P. Hermann, H. A. Rowley, S. C. Johnson, and R. J. Dempsey, "The relationship between carotid artery plaque stability and white matter ischemic injury," *Neuroimage Clin,* vol. 9, pp. 216-22, 2015.

[48] R. Ditaranto, G. Vitale, M. Lorenzini, and C. Rapezzi, "The complex interplay between fitness, genetics, lifestyle, and inflammation in the pathogenesis of coronary atherosclerosis: lessons from the Amazon rainforest," *European Heart Journal Supplements,* vol. 21, no. Supplement_B, pp. B76-B79, 2019.

[49] S. Ogata, K. Nishimura, M. Guzman-Castillo, Y. Sumita, M. Nakai, Y. M. Nakao, N. Nishi, T. Noguchi, A. Sekikawa, Y. Saito, T. Watanabe, Y. Kobayashi, T. Okamura, H. Ogawa, S. Yasuda, Y. Miyamoto, S. Capewell, and M. O'Flaherty, "Explaining the decline in coronary heart disease mortality rates in Japan: Contributions of changes in risk factors and evidence-based treatments between 1980 and 2012," *Int J Cardiol,* vol. 291, pp. 183-188, Sep 15, 2019.

[50] E. M. Urbina, T. R. Kimball, C. E. McCoy, P. R. Khoury, S. R. Daniels, and L. M. Dolan, "Youth with obesity and obesity-related type 2 diabetes mellitus demonstrate abnormalities in carotid structure and function," *Circulation,* vol. 119, no. 22, pp. 2913-9, Jun 9, 2009.

[51] M. S. Kamińska, D. Schneider-Matyka, K. Rachubińska, M. Panczyk, E. Grochans, and A. M. Cybulska, "Menopause Predisposes Women to Increased Risk of Cardiovascular Disease," *J Clin Med,* vol. 12, no. 22, Nov 13, 2023.

[52] J. E. Roeters van Lennep, L. S. Tokgözoğlu, L. Badimon, S. M. Dumanski, M. Gulati, C. N. Hess, K. B. Holven, M. Kavousi, M. Kayıkçıoğlu, E. Lutgens, E. D. Michos, E. Prescott, J. K. Stock, A. Tybjaerg-Hansen, M. J. H. Wermer, and M. Benn, "Women, lipids, and atherosclerotic cardiovascular disease: a call to action from the European Atherosclerosis Society," *European Heart Journal,* vol. 44, no. 39, pp. 4157-4173, 2023.

[53] G. Velarde, K. Bravo-Jaimes, E. J. Brandt, D. Wang, P. Douglass, L. R. Castellanos, F. Rodriguez, L. Palaniappan, U. Ibebuogu, R. Bond, K. Ferdinand, G. Lundberg, R. Thamman, K. Vijayaraghavan, and K. Watson, "Locking the Revolving Door: Racial Disparities in Cardiovascular Disease," *J Am Heart Assoc,* vol. 12, no. 8, pp. e025271, Apr 18, 2023.

[54] A. M. Kanaya, "Diabetes in South Asians: Uncovering Novel Risk Factors With Longitudinal Epidemiologic Data: Kelly West Award Lecture 2023," *Diabetes Care,* vol. 47, no. 1, pp. 7-16, Jan 1, 2024.

[55] D. M. Lloyd-Jones, Y. Hong, D. Labarthe, D. Mozaffarian, L. J. Appel, L. Van Horn, K. Greenlund, S. Daniels, G. Nichol, G. F. Tomaselli, D. K. Arnett, G. C. Fonarow, P. M. Ho, M. S. Lauer, F. A. Masoudi, R. M. Robertson, V. Roger, L. H. Schwamm, P. Sorlie, C. W.

Yancy, and W. D. Rosamond, "Defining and Setting National Goals for Cardiovascular Health Promotion and Disease Reduction," *Circulation,* vol. 121, no. 4, pp. 586-613, 2010.

[56] W. Yang, Q. Nie, Y. Sun, D. Zou, J. Tang, and M. Wang, "Early prediction of atherosclerosis diagnosis with medical ambient intelligence," *Front Physiol,* vol. 14, pp. 1225636, 2023.

[57] S. Jebari-Benslaiman, U. Galicia-García, A. Larrea-Sebal, J. R. Olaetxea, I. Alloza, K. Vandenbroeck, A. Benito-Vicente, and C. Martín, "Pathophysiology of Atherosclerosis," *Int J Mol Sci,* vol. 23, no. 6, Mar 20, 2022.

[58] D. A. Chistiakov, A. A. Melnichenko, V. A. Myasoedova, A. V. Grechko, and A. N. Orekhov, "Mechanisms of foam cell formation in atherosclerosis," *J Mol Med (Berl),* vol. 95, no. 11, pp. 1153-1165, Nov, 2017.

[59] M. R. Bennett, S. Sinha, and G. K. Owens, "Vascular Smooth Muscle Cells in Atherosclerosis," *Circ Res,* vol. 118, no. 4, pp. 692-702, Feb 19, 2016.

[60] A. C. Newby, and A. B. Zaltsman, "Fibrous cap formation or destruction — the critical importance of vascular smooth muscle cell proliferation, migration and matrix formation," *Cardiovascular Research,* vol. 41, no. 2, pp. 345-360, 1999.

[61] V. Fuster, B. Stein, J. A. Ambrose, L. Badimon, J. J. Badimon, and J. H. Chesebro, "Atherosclerotic plaque rupture and thrombosis. Evolving concepts," *Circulation,* vol. 82, no. 3 Suppl, pp. Ii47-59, Sep, 1990.

[62] T. J. Guzik, and R. M. Touyz, "Oxidative Stress, Inflammation, and Vascular Aging in Hypertension," *Hypertension,* vol. 70, no. 4, pp. 660-667, Oct, 2017.

[63] Y. Higashi, "Roles of Oxidative Stress and Inflammation in Vascular Endothelial Dysfunction-Related Disease," *Antioxidants (Basel),* vol. 11, no. 10, Sep 30, 2022.

[64] J. J. Wentzel, Y. S. Chatzizisis, F. J. H. Gijsen, G. D. Giannoglou, C. L. Feldman, and P. H. Stone, "Endothelial shear stress in the evolution of coronary atherosclerotic plaque and vascular remodelling: current understanding and remaining questions," *Cardiovascular Research,* vol. 96, no. 2, pp. 234-243, 2012.

[65] P. H. Stone, A. U. Coskun, Y. Yeghiazarians, S. Kinlay, J. J. Popma, R. E. Kuntz, and C. L. Feldman, "Prediction of sites of coronary atherosclerosis progression: In vivo profiling of endothelial shear stress, lumen, and outer vessel wall characteristics to predict vascular behavior," *Curr Opin Cardiol,* vol. 18, no. 6, pp. 458-70, Nov, 2003.

[66] P. A. Cahill, and E. M. Redmond, "Vascular endothelium - Gatekeeper of vessel health," *Atherosclerosis,* vol. 248, pp. 97-109, May, 2016.

[67] K. Takata, S. Imaizumi, B. Zhang, S. Miura, and K. Saku, "Stabilization of high-risk plaques," *Cardiovasc Diagn Ther,* vol. 6, no. 4, pp. 304-21, Aug, 2016.

[68] T. J. van Trier, N. Mohammadnia, M. Snaterse, R. J. G. Peters, H. T. Jørstad, and W. A. Bax, “Lifestyle management to prevent atherosclerotic cardiovascular disease: evidence and challenges,” *Neth Heart J,* vol. 30, no. 1, pp. 3-14, Jan, 2022.

[69] A. Schmidt-Trucksäss, A. H. Lichtenstein, and R. von Känel, “Lifestyle factors as determinants of atherosclerotic cardiovascular health,” *Atherosclerosis,* vol. 395, 2024.

[70] J. K. Liao, and U. Laufs, “Pleiotropic effects of statins,” *Annu Rev Pharmacol Toxicol,* vol. 45, pp. 89-118, 2005.

[71] J. Y. Choi, and J. O. Na, “Pharmacological Strategies beyond Statins: Ezetimibe and PCSK9 Inhibitors,” *J Lipid Atheroscler,* vol. 8, no. 2, pp. 183-191, Sep, 2019.

[72] A. von Eckardstein, and C. J. Binder, "Prevention and Treatment of Atherosclerosis: Improving State-of-the-Art Management and Search for Novel Targets," 2022.

[73] J. Ye, L. Li, M. Wang, Q. Ma, Y. Tian, Q. Zhang, J. Liu, B. Li, B. Zhang, H. Liu, and G. Sun, “Diabetes Mellitus Promotes the Development of Atherosclerosis: The Role of NLRP3,” *Front Immunol,* vol. 13, pp. 900254, 2022.

[74] S. Degrauwe, T. Pilgrim, A. Aminian, S. Noble, P. Meier, and J. F. Iglesias, “Dual antiplatelet therapy for secondary prevention of coronary artery disease,” *Open Heart,* vol. 4, no. 2, pp. e000651, 2017.

[75] M. Valgimigli, H. Bueno, R. A. Byrne, J.-P. Collet, F. Costa, A. Jeppsson, P. Jüni, A. Kastrati, P. Kolh, L. Mauri, G. Montalescot, F.-J. Neumann, M. Petricevic, M. Roffi, P. G. Steg, S. Windecker, J. L. Zamorano, G. N. Levine, E. S. D. Group, E. C. f. P. Guidelines, and E. N. C. Societies, “2017 ESC focused update on dual antiplatelet therapy in coronary artery disease developed in collaboration with EACTS: The Task Force for dual antiplatelet therapy in coronary artery disease of the European Society of Cardiology (ESC) and of the European Association for Cardio-Thoracic Surgery (EACTS),” *European Heart Journal,* vol. 39, no. 3, pp. 213-260, 2017.

[76] Q. Xie, J. Huang, K. Zhu, and Q. Chen, “Percutaneous coronary intervention versus coronary artery bypass grafting in patients with coronary heart disease and type 2 diabetes mellitus: Cumulative meta-analysis,” *Clin Cardiol,* vol. 44, no. 7, pp. 899-906, Jul, 2021.

[77] C. Spadaccio, and U. Benedetto, "Coronary artery bypass grafting (CABG) vs. percutaneous coronary intervention (PCI) in the treatment of multivessel coronary disease: quo vadis? -a review of the evidences on coronary artery disease," *Ann Cardiothorac Surg*, 4, pp. 506-515, China, 2018.

[78] D. H. O'Leary, and M. L. Bots, “Imaging of atherosclerosis: carotid intima–media thickness,” *European Heart Journal,* vol. 31, no. 14, pp. 1682-1689, 2010.

[79] J. Andersson, J. Sundström, T. Gustavsson, J. Hulthe, A. Elmgren, K. Zilmer, M. Zilmer, and L. Lind, “Echogenecity of the carotid intima-media complex is related to cardiovascular risk factors, dyslipidemia, oxidative stress and inflammation: the

Prospective Investigation of the Vasculature in Uppsala Seniors (PIVUS) study," *Atherosclerosis,* vol. 204, no. 2, pp. 612-8, Jun, 2009.

[80] S. Ebrahim, O. Papacosta, P. Whincup, G. Wannamethee, M. Walker, A. N. Nicolaides, S. Dhanjil, M. Griffin, G. Belcaro, A. Rumley, and G. D. Lowe, "Carotid plaque, intima media thickness, cardiovascular risk factors, and prevalent cardiovascular disease in men and women: the British Regional Heart Study," *Stroke,* vol. 30, no. 4, pp. 841-50, Apr, 1999.

[81] M. W. Lorenz, J. F. Polak, M. Kavousi, E. B. Mathiesen, H. Völzke, T. P. Tuomainen, D. Sander, M. Plichart, A. L. Catapano, C. M. Robertson, S. Kiechl, T. Rundek, M. Desvarieux, L. Lind, C. Schmid, P. DasMahapatra, L. Gao, K. Ziegelbauer, M. L. Bots, and S. G. Thompson, "Carotid intima-media thickness progression to predict cardiovascular events in the general population (the PROG-IMT collaborative project): a meta-analysis of individual participant data," *Lancet,* vol. 379, no. 9831, pp. 2053-62, Jun 2, 2012.

[82] V. Nambi, L. Chambless, A. R. Folsom, M. He, Y. Hu, T. Mosley, K. Volcik, E. Boerwinkle, and C. M. Ballantyne, "Carotid intima-media thickness and presence or absence of plaque improves prediction of coronary heart disease risk: the ARIC (Atherosclerosis Risk In Communities) study," *J Am Coll Cardiol,* vol. 55, no. 15, pp. 1600-7, Apr 13, 2010.

[83] B. C. Zyriax, K. Dransfeld, and E. Windler, "Carotid intima-media thickness and cardiovascular risk factors in healthy volunteers," *Ultrasound J,* vol. 13, no. 1, pp. 17, Mar 11, 2021.

[84] Y. Ling, Y. Wan, E. Barinas-Mitchell, A. Fujiyoshi, H. Cui, A. Maimaiti, R. Xu, J. Li, C. Suo, and M. Zaid, "Varying Definitions of Carotid Intima-Media Thickness and Future Cardiovascular Disease: A Systematic Review and Meta-Analysis," *Journal of the American Heart Association,* vol. 12, no. 23, pp. e031217, 2023.

[85] S. A. Peters, and M. L. Bots, "Carotid intima-media thickness studies: study design and data analysis," *J Stroke,* vol. 15, no. 1, pp. 38-48, Jan, 2013.

[86] R. R. Kasliwal, M. Bansal, D. Desai, and M. Sharma, "Carotid intima-media thickness: Current evidence, practices, and Indian experience," *Indian J Endocrinol Metab,* vol. 18, no. 1, pp. 13-22, Jan, 2014.

[87] L. Seekircher, L. Tschiderer, L. Lind, M. S. Safarova, M. Kavousi, M. A. Ikram, E. Lonn, S. Yusuf, D. E. Grobbee, J. J. P. Kastelein, F. L. J. Visseren, M. Walters, J. Dawson, P. Higgins, S. Agewall, A. Catapano, E. de Groot, M. A. Espeland, G. Klingenschmid, D. Magliano, M. H. Olsen, D. Preiss, D. Sander, M. Skilton, D. A. Zozulińska-Ziółkiewicz, M. P. C. Grooteman, P. J. Blankestijn, K. Kitagawa, S. Okazaki, M. V. Manzi, C. Mancusi, R. Izzo, M. Desvarieux, T. Rundek, H. C. Gerstein, M. L. Bots, M. J. Sweeting, M. W. Lorenz, and P. Willeit, "Intima-media thickness at the near or far wall of the common carotid artery in cardiovascular risk assessment," *Eur Heart J Open,* vol. 3, no. 5, pp. oead089, Sep, 2023.

[88] C. Mitchell, "Grayscale Analysis of Carotid Plaque: An Overview," *Journal of the American Society of Echocardiography,* vol. 32, no. 8, pp. A21-A22, 2019.

[89] K. Ariyoshi, S. Okuya, I. Kunitsugu, K. Matsunaga, Y. Nagao, R. Nomiyama, K. Takeda, and Y. Tanizawa, "Ultrasound analysis of gray-scale median value of carotid plaques is a useful reference index for cerebro-cardiovascular events in patients with type 2 diabetes," *J Diabetes Investig,* vol. 6, no. 1, pp. 91-7, Jan, 2015.

[90] R. Sztajzel, S. Momjian, I. Momjian-Mayor, N. Murith, K. Djebaili, G. Boissard, M. Comelli, and G. Pizolatto, "Stratified Gray-Scale Median Analysis and Color Mapping of the Carotid Plaque," *Stroke,* vol. 36, no. 4, pp. 741-745, 2005.

[91] C. C. Mitchell, J. H. Stein, T. D. Cook, S. Salamat, X. Wang, T. Varghese, D. C. Jackson, C. Sandoval Garcia, S. M. Wilbrand, and R. J. Dempsey, "Histopathologic Validation of Grayscale Carotid Plaque Characteristics Related to Plaque Vulnerability," *Ultrasound Med Biol,* vol. 43, no. 1, pp. 129-137, Jan, 2017.

[92] N. Katakami, T. A. Matsuoka, and I. Shimomura, "Clinical utility of carotid ultrasonography: Application for the management of patients with diabetes," *J Diabetes Investig,* vol. 10, no. 4, pp. 883-898, Jul, 2019.

[93] M. Alexandratou, A. Papachristodoulou, X. Li, S. Partovi, A. Davidhi, V. Rafailidis, P. Prassopoulos, V. Kamperidis, I. Koutroulou, G. Tsivgoulis, N. Grigoriadis, C. Krogias, and T. Karapanayiotides, "Advances in Noninvasive Carotid Wall Imaging with Ultrasound: A Narrative Review," *J Clin Med,* vol. 11, no. 20, Oct 20, 2022.

[94] C. N. Steffel, R. Brown, C. E. Korcarz, T. Varghese, J. H. Stein, S. M. Wilbrand, R. J. Dempsey, and C. C. Mitchell, "Influence of Ultrasound System and Gain on Grayscale Median Values," *J Ultrasound Med,* vol. 38, no. 2, pp. 307-319, Feb, 2019.

[95] A. M. Johri, V. Nambi, T. Z. Naqvi, S. B. Feinstein, E. S. H. Kim, M. M. Park, H. Becher, and H. Sillesen, "Recommendations for the Assessment of Carotid Arterial Plaque by Ultrasound for the Characterization of Atherosclerosis and Evaluation of Cardiovascular Risk: From the American Society of Echocardiography," *Journal of the American Society of Echocardiography,* vol. 33, no. 8, pp. 917-933, 2020.

[96] L. Caballero, S. Kou, R. Dulgheru, N. Gonjilashvili, G. D. Athanassopoulos, D. Barone, M. Baroni, N. Cardim, J. J. Gomez de Diego, M. J. Oliva, A. Hagendorff, K. Hristova, T. Lopez, J. Magne, C. Martinez, G. de la Morena, B. A. Popescu, M. Penicka, T. Ozyigit, J. D. Rodrigo Carbonero, A. Salustri, N. Van De Veire, R. S. Von Bardeleben, D. Vinereanu, J.-U. Voigt, J. L. Zamorano, A. Bernard, E. Donal, R. M. Lang, L. P. Badano, and P. Lancellotti, "Echocardiographic reference ranges for normal cardiac Doppler data: results from the NORRE Study," *European Heart Journal - Cardiovascular Imaging,* vol. 16, no. 9, pp. 1031-1041, 2015.

[97] M. Kasner, D. Westermann, P. Steendijk, R. Gaub, U. Wilkenshoff, K. Weitmann, W. Hoffmann, W. Poller, H.-P. Schultheiss, M. Pauschinger, and C. Tschöpe, "Utility of Doppler Echocardiography and Tissue Doppler Imaging in the Estimation of Diastolic

Function in Heart Failure With Normal Ejection Fraction," *Circulation,* vol. 116, no. 6, pp. 637-647, 2007.

[98] A. A. Oglat, M. Z. Matjafri, N. Suardi, M. A. Oqlat, M. A. Abdelrahman, and A. A. Oqlat, "A Review of Medical Doppler Ultrasonography of Blood Flow in General and Especially in Common Carotid Artery," *J Med Ultrasound,* vol. 26, no. 1, pp. 3-13, Jan-Mar, 2018.

[99] A. Granata, F. Fiorini, S. Andrulli, F. Logias, M. Gallieni, G. Romano, E. Sicurezza, and C. E. Fiore, "Doppler ultrasound and renal artery stenosis: An overview," *J Ultrasound,* vol. 12, no. 4, pp. 133-43, Dec, 2009.

[100] K. Nasra, and M. Osher, "Sonography Vascular Peripheral Arterial Assessment, Protocols, and Interpretation," *StatPearls*, Treasure Island (FL): StatPearls Publishing

[101] E. Swanson, "Doppler Ultrasound Imaging for Detection of Deep Vein Thrombosis in Plastic Surgery Outpatients: A Prospective Controlled Study," *Aesthetic Surgery Journal,* vol. 35, no. 2, pp. 204-214, 2015.

[102] M. Suenaga, N. Mizunuma, E. Shinozaki, S. Matsusaka, M. Ozaka, M. Ogura, K. Chin, and T. Yamaguchi, "Anticoagulant therapy for venous thromboembolism detected by Doppler ultrasound in patients with metastatic colorectal cancer receiving bevacizumab," *Onco Targets Ther,* vol. 8, pp. 243-9, 2015.

[103] S. Sarkar, S. Ghosh, S. K. Ghosh, and A. Collier, "Role of transcranial Doppler ultrasonography in stroke," *Postgrad Med J,* vol. 83, no. 985, pp. 683-9, Nov, 2007.

[104] A. Dua, S. S. Desai, A. Nodel, and J. A. Heller, "The Impact of Body Mass Index on Lower Extremity Duplex Ultrasonography for Deep Vein Thrombosis Diagnosis," *Annals of Vascular Surgery,* vol. 29, no. 6, pp. 1136-1140, 2015.

[105] S. Heinitz, J. Müller, K.-V. Jenderka, H. Schlögl, M. Stumvoll, M. Blüher, V. Blank, and T. Karlas, "The application of high-performance ultrasound probes increases anatomic depiction in obese patients," *Scientific Reports,* vol. 13, no. 1, pp. 16297, 2023/09/28, 2023.

[106] R. M. S. Sigrist, J. Liau, A. E. Kaffas, M. C. Chammas, and J. K. Willmann, "Ultrasound Elastography: Review of Techniques and Clinical Applications," *Theranostics,* vol. 7, no. 5, pp. 1303-1329, 2017.

[107] A. Bulum, G. Ivanac, F. Mandurić, L. Pfeifer, M. Bulum, E. Divjak, S. Radoš, and B. Brkljačić, "Contribution of UltraFast™ Ultrasound and Shear Wave Elastography in the Imaging of Carotid Artery Disease," *Diagnostics (Basel),* vol. 12, no. 5, May 8, 2022.

[108] A. W. Gardner, and D. E. Parker, "Association between arterial compliance and age in participants 9 to 77 years old," *Angiology,* vol. 61, no. 1, pp. 37-41, 2010.

[109] Y. H. Zhang, Y. Gao, and B. L. Su, "Assessment of carotid arterial wall elasticity in type 2 diabetes mellitus patients with microalbuminuria by real-time ultrasound elastography," *Int J Endocrinol,* vol. 2012, pp. 340974, 2012.

[110] X. Xu, B. Wang, C. Ren, J. Hu, D. A. Greenberg, T. Chen, L. Xie, and K. Jin, "Age-related Impairment of Vascular Structure and Functions," *Aging Dis,* vol. 8, no. 5, pp. 590-610, Oct, 2017.

[111] R. J. Dempsey, T. Varghese, D. C. Jackson, X. Wang, N. H. Meshram, C. C. Mitchell, B. P. Hermann, S. C. Johnson, S. E. Berman, and S. M. Wilbrand, "Carotid atherosclerotic plaque instability and cognition determined by ultrasound-measured plaque strain in asymptomatic patients with significant stenosis," *J Neurosurg,* vol. 128, no. 1, pp. 111-119, Jan, 2018.

[112] N. H. Meshram, T. Varghese, C. C. Mitchell, D. C. Jackson, S. M. Wilbrand, B. P. Hermann, and R. J. Dempsey, "Quantification of carotid artery plaque stability with multiple region of interest based ultrasound strain indices and relationship with cognition," *Phys Med Biol,* vol. 62, no. 15, pp. 6341-6360, Jul 17, 2017.

[113] N. H. Meshram, and T. Varghese, "GPU Accelerated Multilevel Lagrangian Carotid Strain Imaging," *IEEE Trans Ultrason Ferroelectr Freq Control,* vol. 65, no. 8, pp. 1370-1379, Aug, 2018.

[114] N. H. Meshram, D. Jackson, T. Varghese, C. C. Mitchell, S. M. Wilbrand, R. J. Dempsey, and B. P. Hermann, "A Cross-Sectional Investigation of Cognition and Ultrasound-Based Vascular Strain Indices," *Arch Clin Neuropsychol,* vol. 35, no. 1, pp. 46-55, Jan 24, 2019.

[115] N. H. Meshram, C. C. Mitchell, S. M. Wilbrand, R. J. Dempsey, and T. Varghese, "In vivo carotid strain imaging using principal strains in longitudinal view," *Biomed Phys Eng Express,* vol. 5, no. 3, 2019.

[116] M. McCormick, N. Rubert, and T. Varghese, "Bayesian regularization applied to ultrasound strain imaging," *IEEE Trans Biomed Eng,* vol. 58, no. 6, pp. 1612-20, Jun, 2011.

[117] M. McCormick, T. Varghese, X. Wang, C. Mitchell, M. A. Kliewer, and R. J. Dempsey, "Methods for robust in vivo strain estimation in the carotid artery," *Phys Med Biol,* vol. 57, no. 22, pp. 7329-53, Nov 21, 2012.

[118] X. Wang, C. C. Mitchell, T. Varghese, D. C. Jackson, B. G. Rocque, B. P. Hermann, and R. J. Dempsey, "Improved Correlation of Strain Indices with Cognitive Dysfunction with Inclusion of Adventitial Layer with Carotid Plaque," *Ultrason Imaging,* vol. 38, no. 3, pp. 194-208, May, 2016.

[119] J. D. Cameron, C. Rajkumar, B. A. Kingwell, G. L. Jennings, and A. M. Dart, "Higher systemic arterial compliance is associated with greater exercise time and lower blood pressure in a young older population," *J Am Geriatr Soc,* vol. 47, no. 6, pp. 653-6, Jun, 1999.

[120] L. J. Chalmers, K. C. Copeland, C. N. Hester, D. A. Fields, and A. W. Gardner, "Paradoxical increase in arterial compliance in obese pubertal children," *Angiology,* vol. 62, no. 7, pp. 565-70, Oct, 2011.

[121] J. B. Tryggestad, and K. R. Short, "Arterial compliance in obese children: implications for cardiovascular health," *Exerc Sport Sci Rev,* vol. 42, no. 4, pp. 175-82, Oct, 2014.

[122] H. Shi, C. C. Mitchell, M. McCormick, M. A. Kliewer, R. J. Dempsey, and T. Varghese, "Preliminary in vivo atherosclerotic carotid plaque characterization using the accumulated axial strain and relative lateral shift strain indices," *Phys Med Biol,* vol. 53, no. 22, pp. 6377-94, Nov 21, 2008.

[123] C. Palombo, and M. Kozakova, "Arterial stiffness, atherosclerosis and cardiovascular risk: Pathophysiologic mechanisms and emerging clinical indications," *Vascul Pharmacol,* vol. 77, pp. 1-7, Feb, 2016.

[124] G. Cismaru, T. Serban, and A. Tirpe, "Ultrasound Methods in the Evaluation of Atherosclerosis: From Pathophysiology to Clinic," *Biomedicines,* vol. 9, no. 4, Apr 13, 2021.

[125] P. Boutouyrie, P. Chowienczyk, J. D. Humphrey, and G. F. Mitchell, "Arterial Stiffness and Cardiovascular Risk in Hypertension," *Circulation Research,* vol. 128, no. 7, pp. 864-886, 2021/04/02, 2021.

Chapter 3: Automatic Carotid Feature Segmentation

In this chapter* [1] we utilize a Mask Region-based Convolutional Neural Networks (R-CNN) network to estimate Carotid lumen plus wall [1, 2] and Carotid plaque segmentations for use in our ultrasound elastography workflow. The goal for this deep learning network (DLN) is to assist with the time-consuming process of carotid feature segmentation performed by a sonographer.

3.1. Background

Atherosclerosis is the most common systemic vascular disease[3] and is a contributing factor in a majority of cardiovascular and cerebrovascular diseases[4]. According to the Center for Disease Control (CDC), cardiovascular and cerebrovascular diseases are among the leading causes of death and the leading causes of disability in the United States in 2019[5] and account for about 30% of mortality worldwide[6]. The buildup of plaque in the arteries is a lifelong process. While it is unknown what causes this plaque buildup, high cholesterol, diabetes, high blood pressure, and smoking all contribute to increased levels of atherosclerosis [7]. With the median age in developed countries continuing to rise[8] and the prevalence of lifestyle-related risk factors in the younger generation, the effect of atherosclerosis on the population will only increase.

Among cerebrovascular diseases, ischemic strokes (due to plaque related complications) are the most common [7]. Carotid atherosclerosis (plaque deposition) is considered a risk factor for ischemic stroke because the plaque may be obstructive resulting in hypoperfusion to the brain or may be unstable. Unstable plaque can release emboli into the blood stream that can obstruct blood vessels in the brain resulting hypoxic damage to brain tissue. Presently, symptoms and the potential

*This chapter is adapted from Kiernan M et al. Lumen segmentation using a Mask R-CNN in carotid arteries with stenotic atherosclerotic. Ultrasonics. 2024;137:107193.

of ischemic stroke are only witnessed following a life-threatening event or concerns surrounding the effect of a known risk factor[9]. Additionally, for each recognized stroke, more than 5 ‘silent strokes’ may occur in these patients [10, 11]. Combined with the increased prevalence of atherosclerosis, the threat that is ischemic strokes will continue to be a major cause of death and disability in developed countries [10, 11].

Identifying unstable plaque is important in order to optimize lifestyle modifications and medical treatment for the individual to reduce future risk for cardiovascular disease [12]. Currently, the main identifiers for those requiring treatment are previously documented symptoms of transient ischemic attack (TIA), stroke or those known to be at high risk (individuals with high blood pressure, diabetes or previously reported heart/vessel conditions). Carotid ultrasound is also used as a tool to determine plaque presence, plaque characteristics (echogenicity, surface) and percent stenosis. Information from the carotid examination is often used to direct patient management (i.e., medical treatment, carotid stenting or carotid endarterectomy) [4, 13, 14].

One method that can be used to identify plaque stability is ultrasound elastography. Ultrasound elastography quantifies regions of increased strain or deformation to determine a plaque stability [12, 15-17]. Increased strain in plaque has been associated with echolucent or softer plaque which are more prone to rupture [10, 17-19]. Reports from intravascular ultrasound (IVUS) elastography of coronary arteries also indicate that plaque composition is critical to assess stable vs unstable plaques, with higher strain distribution seen in fatty versus fibrous or calcific plaque [20, 21]. Additionally, high-strain regions observed in thin-cap fibrous atheroma are associated with increased presence of macrophages indicating vulnerable plaque susceptible to rupture [20, 21]. In arterial segments without plaque, stiffer arterial walls (lower strain values) are often attributed to areas of potential inflammation and possible sites for future plaque deposition[22].

Our ultrasound elastography protocol utilizes Lagrangian strain estimation detailed by McCormick et al. (2012) [23] and adapted for Graphics Processing Unit (GPU) acceleration by Meshram et al. (2018) [24] to calculate the strain distribution and quantitative strain indices on manually segmented plaque. We have demonstrated significant correlation of softer plaque based on our strain indices with cognition [10, 17] and magnetic resonance imaging (MRI) based white matter hyperintensity changes in the brain [25]. In order to perform accurate strain measurements, an accurate segmentation performed on an ultrasound B-mode image and tracked over a cardiac cycle is required [26]. Current protocol utilizes segmentations performed by a trained sonographer. The sonographer segments end diastolic frames using radiofrequency (RF) data converted to B-mode along with clinical color Doppler images. This binary mask can then be accurately propagated over all the frames in the cardiac cycle using the Bayesian carotid strain imaging algorithm[27].This is a time intensive process that prevents extensive analysis of patients beyond those known to be at risk [28]. The method described in this manuscript is anticipated to replicate the segmentation of RF-derived B-mode images that is currently performed by a trained sonographer.

Ultrasound elastography can play a pivotal role in monitoring the progression of carotid atherosclerosis over time, as well as in assessing the risk of plaque rupture and subsequent vascular cognitive dysfunction.[10, 25] Serial ultrasound examinations allow healthcare providers to track changes in plaque size, morphology, composition, and stability, offering a dynamic noninvasive assessment of disease progression and risk over time. This longitudinal monitoring is essential for tailoring treatment plans, adjusting medication regimens, and implementing lifestyle interventions to effectively manage and mitigate the impact of atherosclerosis on cardiovascular health.

However, our current ultrasound elastography protocol's reliance on manual segmentation of plaques by a trained sonographer presents practical challenges. This segmentation process, performed on end-diastolic frames using ultrasound radiofrequency (RF) data converted to B-mode and clinical color Doppler images, is time-intensive and limits extensive patient analysis beyond those already identified to be at risk.

Various approaches to resolving this issue have been reported. Manual image processing techniques such as active contours [29-32] and edge detection [33, 34] have shown inconsistent results and require user interaction. In the search for an automated approach, convolutional neural networks (CNNs) have been utilized for segmentation.[35, 36] Current methods for plaque segmentation using CNNs can be classified into semi-automatic and automatic methods. Semi-automatic methods require manual input, such as an Region of Interest (ROI) or spline[37], and have produced favorable results due to their limited scope. However, they still require advanced knowledge to locate the proper region for segmentation.[26] Automated methods are less dependent on user inputs but have shown limitations in accuracy compared to ground truth models and require well-trained models.

In their 2021 study, Zhou et al.[35] employed a U-Net structure for segmenting carotid plaques in 3D ultrasound images, utilizing datasets from two different sources. Their study, however, excluded patients with >70% stenosis, specifically evaluated in our study, who form the more challenging group with complex plaque, attenuation, and other artifacts. Results from two independent U-Net structures demonstrated an increased level of agreement with manual segmentations, with Pearson's correlation coefficients of 0.989 ($p < 0.0001$) and 0.987 ($p < 0.0001$). Despite the apparent automation of the method, it is essential to note that the dataset employed in this study comprised pre-cropped images focusing solely on the desired plaque

region. More recently, Zhou et al. (2023) [36] presented an image reconstruction-based self-supervised learning algorithm (IR-SSL) with U-Net and U-Net++, demonstrating improved performance and achieving Dice-similarity-coefficients (DSC) of 80.14–88.84%. While methods of this nature are often considered fully automatic, they still necessitate additional manual input in the form of cropping the original B-mode image. In specific scenarios, particularly when working with B-mode images, employing an automated system to crop images and retain only the ultrasound ROI may be acceptable[35, 38]. These nuances in fully automatic approaches are highlighted in our labs' prior work conducted by Meshram et al. in 2020[26]. This work revealed that a semi-automatic approach, incorporating a user-defined bounding box to limit the search area, yielded more favorable segmentation results compared to an unrestricted fully automatic approach.

Yang et al. [39] demonstrated that segmentation of the carotid artery in the transverse plane can be accurately extracted using self-adaptive histogram equalization, non-linear filtering, canny edge detection and morphology methods. Carvalho et al. [40] utilized contrast enhanced ultrasound (CEUS) alongside standard B-mode ultrasound to accurately segment the carotid lumen. Their method consists of an algorithm-based approach to obtain edge and centerline contours of the lumen, which can be utilized to identify changes in arterial diameter caused by the presence of atherosclerotic plaque. The major downside to this approach is the use of injected contrast agents in CEUS that limit its use this method in large-scale screenings. Xie et al. [28] demonstrated that CNNs can also provide accurate segmentation of the carotid lumen. Using a U-Net architecture, a segmentation accuracy of 94.3% was obtained, in the presence of significant plaque, calcified wall, and acoustic shadowing.

Jain et al. [41] demonstrated a method of localization of the common carotid artery (CCA) in the transverse view using a fast region convolutional neural network (FRCNN)-based localization

method. They found that their model can determine a bounding box for cross-sectional CCAs with an accuracy of about 88%. Qian et al.[42] used random forests to initiate a learning-based strategy to segment carotid plaque in B-mode longitudinal ultrasound images. Yang et al.[43] utilized a dual path U-Net structure to segment arterial lumen walls of IVUS images using a similar dataset size as that used in this work. Deep learning has also been used for improved estimation of vessel-flow dynamics [44] and Doppler velocity estimation [45].

The literature reported here utilized clinical B-mode images which are the result of vendor-specific black box image enhancement methods for training the detection and segmentation model. However, in the case of strain indices estimation, segmentation is done on the spatial dimension of the ultrasound RF data thus requiring an automatic detection and segmentation method trained on unfiltered ultrasound B-mode images reconstructed directly from RF data. We have previously demonstrated Lagrangian strain estimation both in manually segmented plaque regions[17, 46] and vessel wall segmentations.[47] Prior work [26] has also demonstrated that a bounding box around the plaque significantly improves the segmentation accuracy compared to direct segmentation of plaque from the entire B-mode image. Therefore, accurate lumen segmentation will provide us with improved ROI initialization for both vessel wall and plaque segmentation models, which in turn will return an accurate binary mask encompassing the plaque at end diastole.

3.2. Materials and Methods

3.2.1. Human Subjects and Data

Our dataset consists of ultrasound RF data loops, acquired over 2-3 cardiac cycles, from 118 patients with severe carotid stenosis due to atherosclerotic plaque, and who were referred for clinically indicated carotid endarterectomy (CEA). This dataset has been previously [16, 48, 49]

documented and is identical to the dataset used in Meshram et al. [26]. Ultrasound RF and B-mode data loops were acquired by keeping the transducer relatively stationary for freehand acquisitions with respect to the skin surface. Acquisition was performed using a Siemens S2000 system (Siemens Ultrasound, Mountain View, CA, USA) with an 18L6 linear array transducer. Data was collected in the longitudinal imaging planes covering the carotid artery in three spatial locations, namely the common carotid artery, carotid bifurcation, and internal carotid artery at a depth of 4 cm on both left and right side for each patient. A total of 350 views with plaque were obtained. In each view, the sonographer manually segmented plaque at two to three end diastolic frames on the B-mode image frames that were converted from acquired RF data. Originally, images and segmentations for the carotid lumen and wall segmentation model were resampled from their original size of 455 × 691 pixels to a size of 512 × 512 pixels. After a follow up investigation of this model, images were left at their original size for the carotid plaque model.

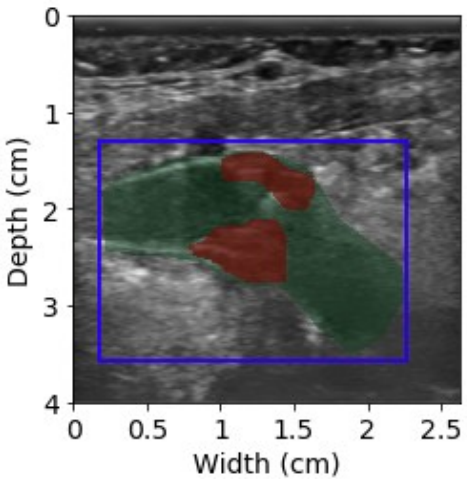

Figure 3.1. Example segmentations and lumen bounding box utilized in this study. Plaque segmentations are depicted in red, while lumen segmentation is depicted in green. The ground truth lumen bounding box is depicted in blue.

After segmentation, rectangular bounding boxes containing the segmented plaque and lumen were generated under the guidance of the sonographer. This process resulted in a dataset of 885

individual plaque segmentations and lumen detected frames for training and validation of the Mask R-CNN models. Figure 3.1 provides an example of the plaque and lumen.

3.2.2. Network Structure

There are several object detection methods reported in literature, such as You Only Look Once (YOLO) [50], Single Shot MultiBox Detector (SSD) [51], Detection Transformer (DETR) [52], and Faster R-CNN.[53] However, all of these methods only detect the bounding box, but do not return any segmentation within the bounding box. Therefore, we decided to utilize the Mask R-CNN network [54] which had the state-of-the-art performance in terms of instance segmentation (simultaneous detection and segmentation). Prediction of segmentation masks is performed in parallel to the prediction of the class and bounding box. The network seeks to optimize a joint loss function between each task, decoupling the mask and bounding box predictions. Instance segmentation is critical for our downstream task of plaque segmentation as an ultrasound B-mode image might contain multiple disconnected plaque ROIs in it. The model is pre-trained on the COCO (Common Objects in Context) dataset[55] to leverage transfer learning for carotid feature detection.

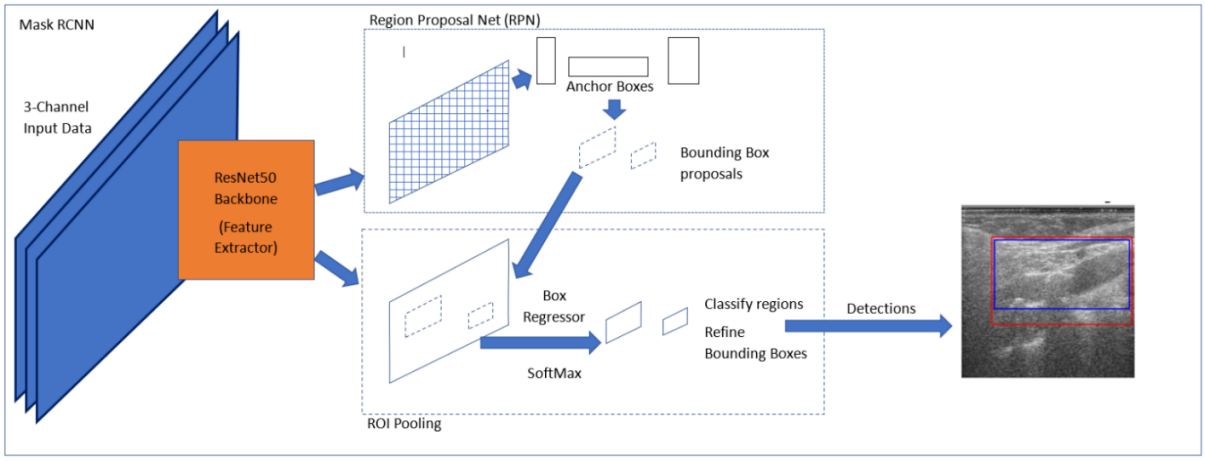

Figure 3.2. Mask R-CNN model utilizing a ResNet50 backbone. Three-channel data consisting of B-mode data from RF, Inphase/Quadrature (IQ), MimickNet B-mode and short time Spatiotemporal Clutter Filtered Power Images are used here.

The Dice similarity coefficient (DSC), intersection over Union (IoU), average precision (AP) and average recall (AR) in COCO evaluation format were used to evaluate the lumen ROI and lumen segmentation results. Below are the defined equations for the evaluation parameters used in the study.

Eq 3.1. $$DSC = \frac{2TP}{2TP + FP + FN}$$

Eq 3.2. $$AP = \frac{TP}{TP + FP}$$

Eq 3.3. $$Recall = \frac{TP}{TP + FN}$$

Eq 3.4. $$IoU = \frac{area\ of\ overlap}{area\ of\ union} = \frac{|A \cap B|}{|A \cup B|}$$

TP indicates a true positive result, where the predicted bounding box or segmentation region agrees with the ground truth. FP indicates a false positive result, where the model predicts a result that does not agree with the ground truth. FN indicates a false negative result, where the model does not predict a result, but a result is expected in the ground truth region. A and B in the IoU equation represent the predicted and ground truth regions, respectively.

3.2.3 Carotid Lumen and Wall Model

Three-Channel image data, i.e., B-mode data derived from raw RF data, MimickNet (MimNet) B-mode [56] and short time Spatiotemporal Clutter Filtered Power Images obtained using singular value decomposition (SVD) as well as single channel RF data, were generated as the input for Mask R-CNN. The structure of the Mask R-CNN model used is shown in Figure 3.2. MimickNet B-mode images are derived from a deep learning framework that transforms conventional delay-and-summed (DAS) images into approximated Dynamic Tissue Contrast Enhanced (DTCE) post-processed images similar to those on Siemens clinical scanners [56].

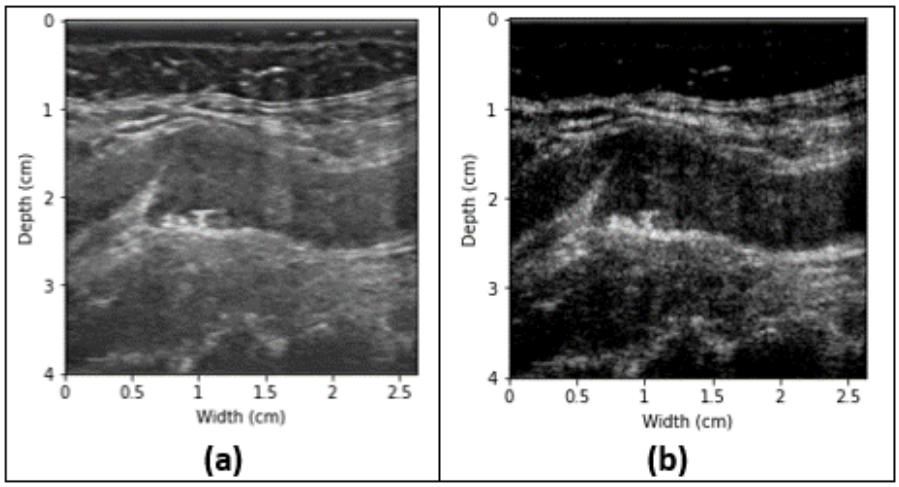

Figure 3.3. (a) MimickNet derived processed image. (b) Spatiotemporal Clutter Filtered Power Image.

Utilizing Eigen decomposition of the images, SVD decomposes the image matrix into a diagonal matrix containing singular values, a unitary matrix of singular vectors related to the axial variation of an image, and a unitary matrix of singular vectors related to the lateral variation [57]. SVD-based methods have been most commonly used in Doppler ultrasound to separate flow from slower moving tissue [58, 59], but have proven to reduce speckle noise in medical ultrasound images when utilized in an adaptive beamformer.[57] In this work, we have used two singular value thresholds for SVD filtering [60] - (a) low order singular value threshold for static tissue signal suppression (b) high order singular value threshold for random noise suppression. First, singular values were derived by applying spatiotemporal SVD on casorati matrix extracted from a sequence of complex carotid IQ data covering one cardiac cycle. Next, singular values were normalized, and a singular value ratio vector was derived by calculating the ratio between each adjacent singular value. Singular values with ratio greater than low order singular value threshold (0.85) were filtered out for suppressing static tissue signals. On the other hand, the gradient of singular value curve was calculated and singular values with a gradient less than the high order threshold (0.01) was filtered for suppressing random noise. Inverse SVD was applied with the filtered singular

value curve resulting in a sequence of filtered carotid ultrasound images over a cardiac cycle. Next, two power images were derived at the end diastole phase of the cardiac cycle (a) considering the first three frames and (b) considering the last three frames of the filtered cardiac cycle data and were used for training. These images are denoted as short-time Spatiotemporal Clutter Filtered Power images. Our hypothesis is that the inclusion of SVD filtered images as an additional input channel to the network would provide additional information to the model that in turn will aid in localization of the carotid lumen. Examples of the MimickNet B-mode and Spatiotemporal Clutter Filtered Power Images are shown in Figure 3.3.

Of the 885 acquired views, approximately 90% (766 images) were used for training and validation while the remaining 10% (119 images) were used in testing. Within the training and validation sets 90% were used for training (694 images) and 10% (77 images) were used for validation. The networks utilized a ResNet50 backbone feature extraction layer and was trained on a NVIDIA A40 GPU (NVIDIA Corporation, Santa Clara, CA, USA) with an AMD EPYC 7H12 CPU (Advanced Micro Devices, Inc., Santa Clara, CA, USA). The initial learning rate was 0.0025, which was reduced by 10% after 16 and 22 epochs respectively. Each layer of the networks are trained for 26 epochs, then the final layer of the models are trained for an additional 10 epochs for fine tuning. Random online data augmentation was provided by affine transformations, horizontal flips, motion blur and adjustment of brightness and contrast.

To identify how well the lumen and wall model predictions match the expected (ground truth) images, the weighted mean signed percent error (MPE) and the weighted mean absolute percent error (MAPE) were used. For a single predicted image y and corresponding ground truth image x with N pixels, the MPE and MAPE are defined as:

Eq 3.5. $$\mathrm{MPE} = \frac{100\%}{N}\sum_{i=1}^{N}\frac{y_i - x_i}{x_i}$$ **Eq 3.6.** $$\mathrm{wMPE} = \frac{100\%}{N}\frac{\sum_{i=1}^{n} y_i - x_i}{\sum_{i=1}^{n} x_i}$$

Eq 3.7. $$\mathrm{MAPE} = \frac{100\%}{N}\sum_{i=1}^{N}\frac{|y_i - x_i|}{x_i}$$ **Eq 3.8.** $$\mathrm{wMAPE} = \frac{100\%}{N}\frac{\sum_{i=1}^{n} |y_i - x_i|}{\sum_{i=1}^{n} x_i}$$

MPE indicates estimation bias, whether a prediction is overestimating (more area is predicted that the ground truth, giving a positive value) or underestimating (negative value) compared to the expected result represented as a percentage of the ground truth. The inclusion of the absolute value in the MAPE presents the total error, as MPE results in value cancellation. This is performed for the areas of the bounding box and lumen segmentations, as well as the height and width of the bounding box. Note that the area-based calculations utilize the weighted versions of these metrics to avoid divide by zero errors caused by the binary nature of the produced areas. Additionally, for the bounding box, we also present the mean distance (in pixels) between the center points of the predicted and ground truth boxes.

3.2.4 Carotid Plaque Model

Apart from minor changes, the same training protocol from the lumen detection model was utilized in the carotid plaque model. Of the 885 acquired views, approximately 90% (766 images) were used for training and validation while the remaining 10% (119 images) were used in testing. Within the training and validation sets 90% were used for training (694 images) and 10% (77 images) were used for validation.

This model investigates the effects of limiting the maximum number of allowed bounding box predictions on Mask R-CNN model accuracy. Different models were trained with bounding box limits ranging from 1 to 5, and each model was tested both with the same limit used during training and with a limit of 2 bounding boxes, resulting in a total of 9 distinct model configurations. The

inclusion of a 2-box testing condition for all models reflects the observation that most images contain at most two plaque segments. By varying the number of bounding boxes during training and testing, we also explore how mismatches between these settings affect performance. For instance, when the model is tested with more boxes than it was trained on ($y > x$), it may output additional regions that are less optimized, potentially introducing more false positives. Conversely, testing with fewer boxes than the model was trained for ($y < x$) may suppress relevant predictions and limit the model's effectiveness. To further assess agreement across models, we identify the most consistent bounding box predictions independent of the ground truth by selecting predicted regions that appear in at least 5 out of the 9 model outputs. This majority-vote strategy highlights which regions are robustly identified across different training and testing constraints.

3.3. Results

3.3.1 Lumen and Wall Model

Figure 3.4 shows results of the bounding box predictions for two cases using the three-channel trained model. For each case, both the B-mode and ground truth segmentation mask are shown. The bounding box predicted by our R-CNN network is depicted in red, and the ground truth bounding box derived from the maximum extents of the segmentation mask is shown in blue. The first case, shown in 5(a), depicts a case where the predicted bounding box region is within acceptable agreement of the ground truth bounding box. In the case shown in 5(b), the predicted bounding box is not in agreement with the ground truth bounding box.

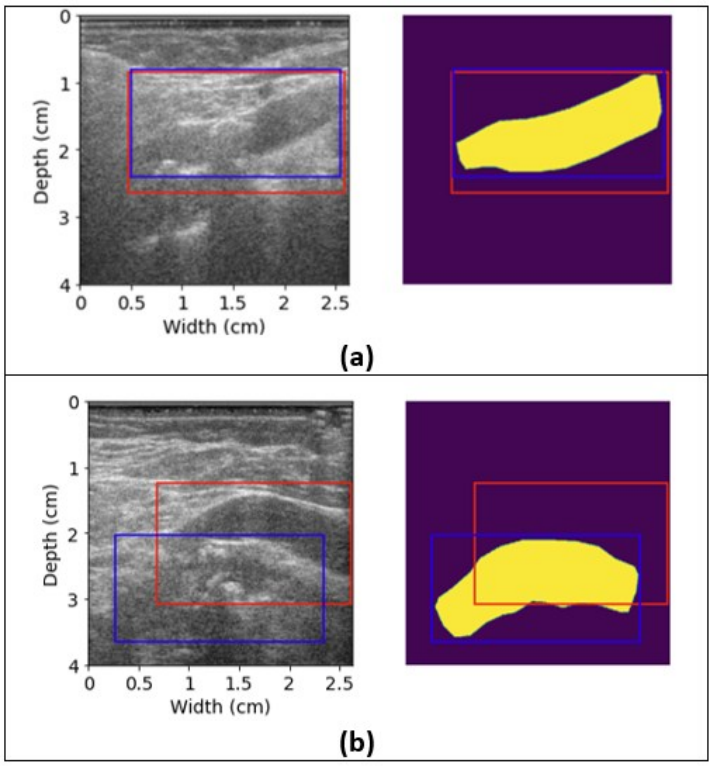

Figure 3.4. Predicted bounding boxes for carotid lumen detection using three-channel training input on B-mode and binary segmentation images. Red boxes represent the predicted bounding boxes and blue boxes represent the ground truth. (a) High agreement case, (b) Poor agreement (detection of jugular vein).

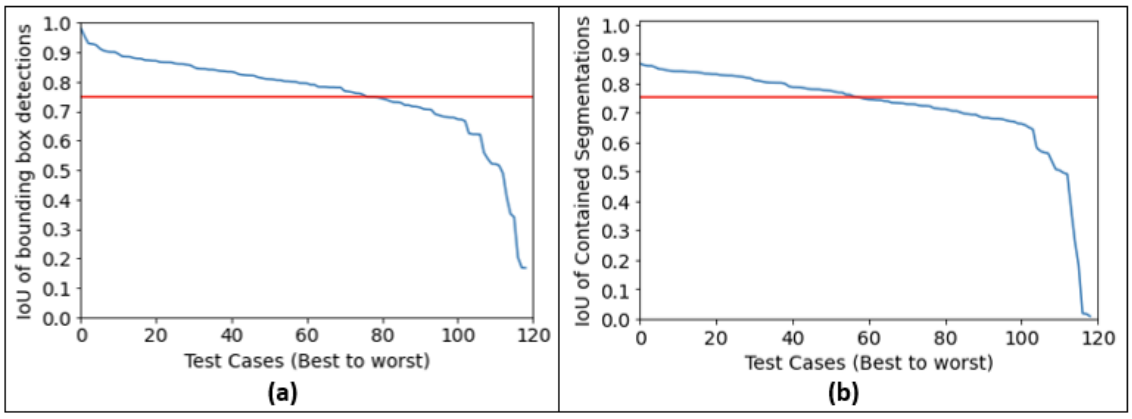

Figure 3.5. IoU metric comparisons for three-channel input model (a) IoUs for bounding box agreement for each test case, sorted from best to worst. (b) IoUs for predicted segmentation agreement, sorted from best to worst. Threshold of 0.75 is shown in red.

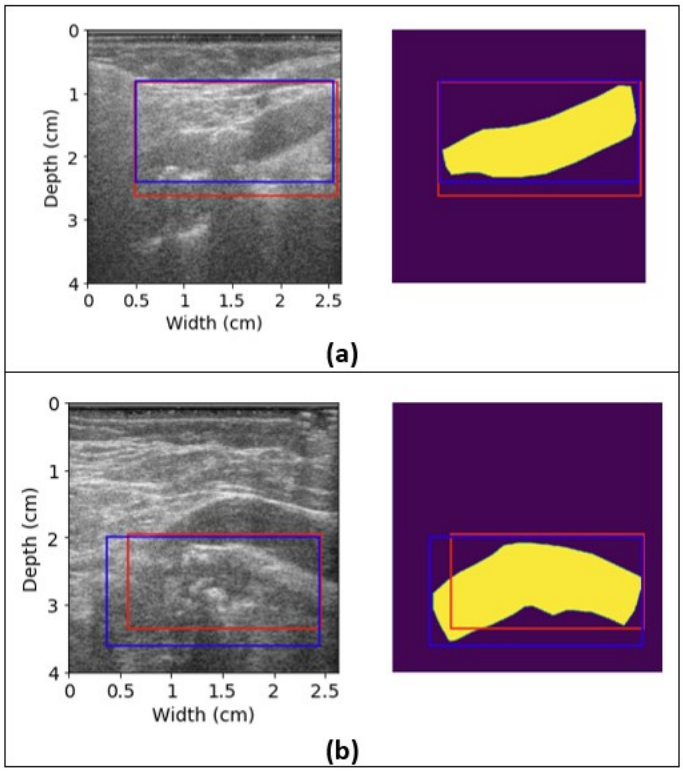

Figure 3.6. Bounding boxes for carotid lumen detection using single-channel training input on B-mode and binary segmentation images. Red boxes represent the predicted bounding boxes and blue boxes represent the ground truth. Same cases shown in Figure 3.4 are shown using the single channel input model. (a) High agreement case, (b) Poor agreement case.

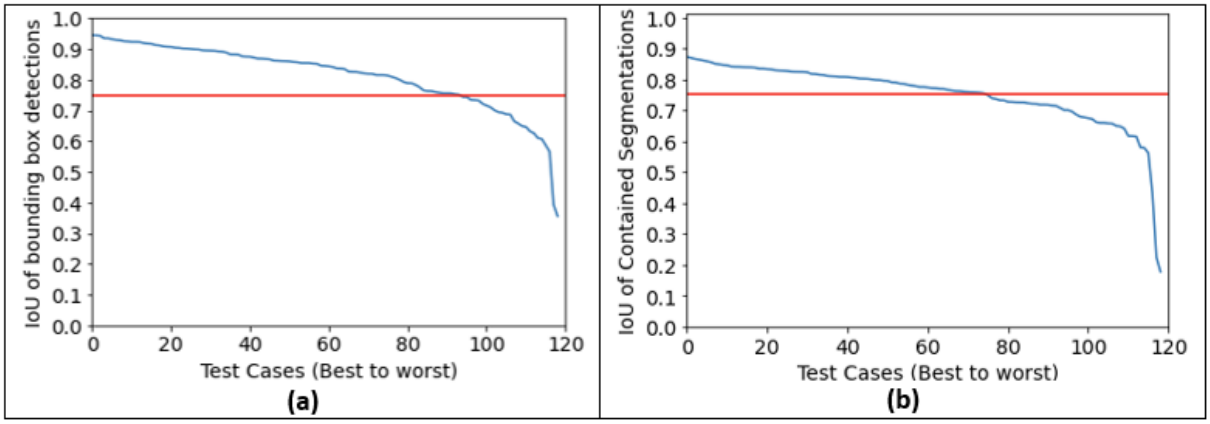

Figure 3.7. IoU metric comparisons for single-channel input model (a) IoUs for bounding box agreement for each test case, sorted from best to worst. (b) IoUs for predicted segmentation agreement, sorted from best to worst. Threshold of 0.75 is shown in red.

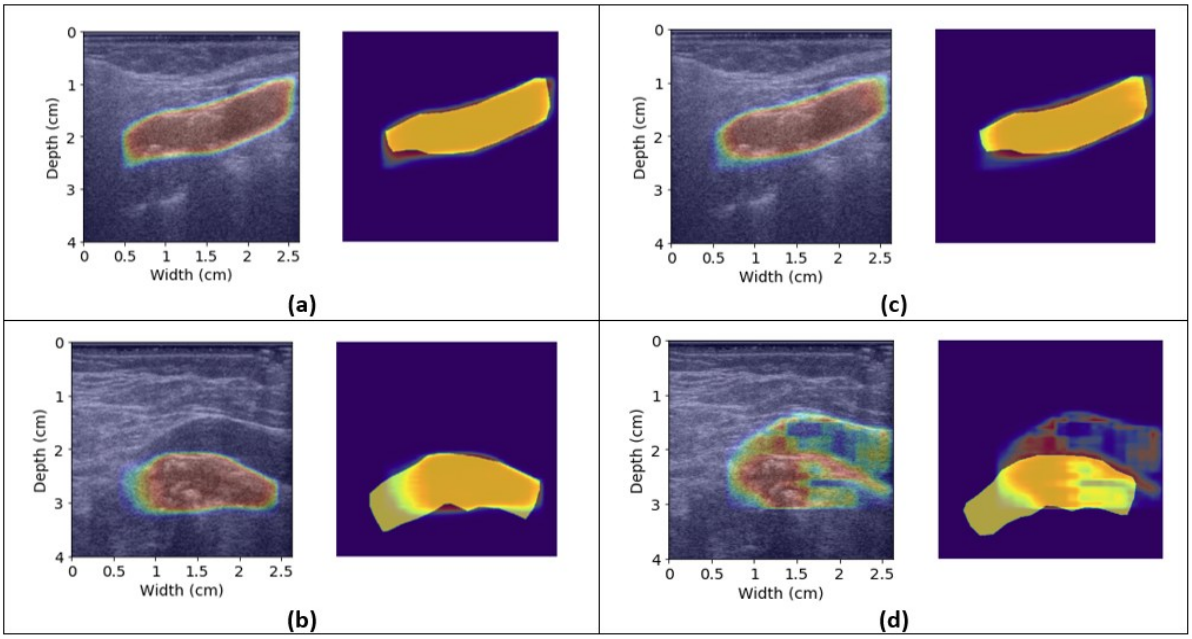

Figure 3.8. Segmentation predictions for carotid lumen detection using single-channel training input (Left) and three-channel training input (Right) on B-mode and binary segmentation images. Confidence levels of prediction regions are shown from red to blue (high to low). (a) high agreement; single-channel, (b) high agreement; three-channel, (c) low agreement; single-channel, (d) low agreement; three-channel.

Figure 3.5 presents plots of the individual IoU values for the test sets ranked from best to worst for both the bounding box ROI and subsequent semantic lumen segmentation comparisons to the ground-truth manual results from the sonographer. Figure 3.5(a) reports the individual IoU values for the bounding box agreement for each of the test cases and are plotted from highest to lowest IoU value. A line, marked in red in the plots, signifies an arbitrary cutoff point of 0.75 where results above the line are considered acceptable. Figure 3.5(b) also plots the IoU for each test case, but the IoU compares the predicted segmentations contained with the ground truth segmentation masks. Figure 3.6 shows the same cases seen in Figure 3.4 utilizing the single channel (B-mode) training model. In both cases, the single channel model produces better bounding box predictions than the three-channel model, with much better agreement in the second case. The single channel model also fails to predict the less defined region of the lumen in the image (seen in the bottom left of Figure 3.6(b). Figure 3.7 shows the same IoU plots for the single channel model as described

previously. Figure 3.8 shows the predicted segmentations for the cases seen in Figures 5 and 7. The segmentations shown with the areas of high confidence shown in red, and areas of low confidence are shown in blue.

Table 3.1 summarizes the network performance statistics reporting mean and standard deviation of IoU as well as the AP and AR for the resultant bounding boxes of each tested model combination. Also shown is the number of test cases that are considered 'acceptable' by having predictions having an IoU agreement of greater than 0.75. Network performance statistics for predicted lumen segmentations are shown in Table 3.2. Table 3.3 presents the weighted mean percent error (wMPE) and mean absolute error (wMAPE) with standard deviations for Bounding box and lumen segmentation results. Statistics on the midpoint, width, and height of the bounding box are presented in Table 3.4. Cases above an arbitrary center point distance threshold is also presented in Table 3.4. The threshold is set to exclude cases with a midpoint distance greater than 25 pixels and cases more than 10% smaller in any dimension than their respective ground truth case.

Training Images used	DCE	Mean IoU	AP IoU= 0.50:0.95	AP IoU= 0.50	AP IoU= 0.75	AR IoU= 0.50:0.95	Cases above threshold
B-mode	0.89±0.07	0.81±0.11	0.62	0.98	0.68	0.68	94/119 (78.99%)
3 Channel	0.85±0.11	0.76±0.12	0.54	0.93	0.57	0.58	76/119 (63.86%)
B-mode + MimNet	0.87±0.11	0.78±0.14	0.58	0.93	0.61	0.63	83/119 (69.75%)
B-mode + SVD	0.84±0.15	0.74±0.17	0.50	0.87	0.51	0.58	75/119 (63.02%)
MimNet + SVD	0.87±0.11	0.77±0.15	0.55	0.92	0.58	0.60	76/119 (63.86%)

Table 3.1. Network performance statistics for bounding box detection.

Training Images used	DCE	Mean IoU	AP IoU= 0.50:0.95	AP IoU= 0.50	AP IoU= 0.75	AR IoU= 0.50:0.95	Cases above threshold
B-mode	0.85±0.08	0.75±0.10	0.64	0.97	0.75	0.68	75/119 (63.02%)
3 Channel	0.82±0.15	0.71±0.16	0.59	0.93	0.71	0.58	58/119 (48.74%)
B-mode + MimNet	0.78±0.14	0.66±0.14	0.55	0.94	0.58	0.60	28/119 (23.53%)
B-mode + SVD	0.77±0.20	0.66±0.19	0.52	0.87	0.51	0.59	39/119 (32.77%)
MimNet + SVD	0.81±0.11	0.70±0.15	0.55	0.93	0.61	0.60	44/119 (36.97%)

Table 3.2. Network performance statistics for lumen segmentation prediction. AP : Average Precision; AR : Average Recall

	Bounding Box		Lumen Segmentation	
Training Images used	wMPE (%)	wMAPE (%)	wMPE (%)	wMAPE (%)
B-mode	10.22±19.81	16.89±14.55	-0.38±16.98	12.21±11.81
3 Channel	16.59±25.16	22.19±20.39	-1.91±19.43	13.32±14.28
B-mode + MimNet	3.77±21.88	15.86±15.53	-11.69±18.09	17.61±12.40
B-mode + SVD	11.52±28.28	19.45±23.55	-11.96±16.62	15.05±13.88
MimNet + SVD	5.71±21.07	17.73±17.25	-4.44±18.66	14.12±12.99

Table 3.3. Percent Errors for network outputs based on object areas.

	Midpoint	Width		Height		
Training Images used	Average Displacement (pixels)	MPE (%)	MAPE (%)	MPE (%)	MAPE (%)	Cases above threshold
B-mode	20.25±18.03	5.62±10.84	8.72±8.52	3.85±10.8	8.82±7.33	90/119 (75.63%)
3-Channel	27.92±30.36	4.24±13.71	10.16±10.10	11.08 ±12.31	12.98±10.28	74/119 (62.18%)
B-mode + MimNet	24.72±22.18	3.25±13.70	9.59±10.27	-0.10±11.29	8.65±7.21	69/119 (57.98%)
B-mode + SVD	33.90±29.94	4.67±12.73	9.67±9.48	5.53±15.92	11.17±12.60	47/119 (39.50%)
MimNet + SVD	26.09±24.56	7.31±15.27	11.38±12.45	-2.29±11.96	9.15±8.00	65/119 (54.62%)

Table 3.4. Midpoint displacement and Percent Errors for bounding box localization.

Figure 3.9 shows segmentation and bounding box predictions of the model in a follow up study for the lumen and wall model using the single channel RF-derived B-mode input and using original image sizes. Table 3.5 shows updated single channel B-Mode performance statistics

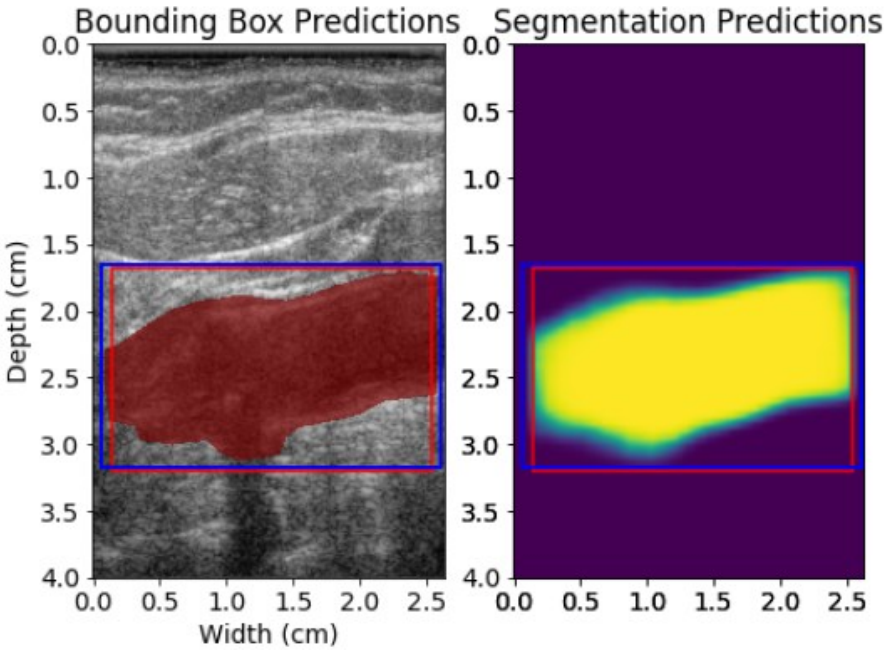

Figure 3.9: Predicted (Red) and Ground Truth (Blue) bounding boxes over B-mode + GT Segmentation Mask (Left) and Binary segmentation mask (Right)

Prediction Type	DCE	Mean IoU	AP IoU= 0.50:0.95	AP IoU=0.50	AP IoU=0.75	AR IoU= 0.50:0.95	Cases above threshold
Bounding Box	0.91±0.04	0.84±0.04	0.68	0.98	0.77	0.74	94/119 (78.99%)
Segmentations	0.88±0.04	0.79±0.06	0.68	0.98	0.76	0.72	76/119 (63.86%)

Table 3.5: Network Performance Statistics for single-channel B-mode lumen and wall segmentation model

3.3.2 Plaque Bounding-Box Testing Results

Figure 3.10 contains a few representative examples for 3 selected models; a model trained with a maximum of three bounding boxes and tested on a maximum of two bounding boxes (A-C) and models trained with a maximum of five bounding boxes and tested with a maximum of 2 (D-F)

and 5 bounding boxes (G-I) respectively. For each model there are three cases labeled as columns I, II, and III. Each instance contains a bounding box prediction and a segmentation prediction. The bounding box prediction contains the RF-derived B-mode image with the baseline segmentations for the carotid lumen and any carotid plaque present. The ground truth bounding boxes derived from the ground truth plaque segmentations are depicted with a blue rectangular outline, while the predicted bounding box is depicted as a red outline. The segmentation results are shown with the ground truth manual segmentations shown in dark yellow, and the predicted segmentation maps are overlaid within the predicted regions using a scale from green to yellow, where brighter yellow denotes more confidence in the result.

Figure 3.11, presents bounding box predictions for all models tested. For each image, corresponding to the respective columns *I, II,* and *III* in Figure 3.10, show the ground truth bounding box area, raw predicted bounding box area, and the filtered results. The first image is simply the ground truth bounding box area for reference. The second image is a raw composite of all nine segmentation models tested in this study. Brighter regions indicate areas of high agreement between models. The final image contains the final 'reconstructed' result by only incorporating regions where at least five of the models agree upon an area.

Table 3.6 presents bounding box results for the nine training and testing schemes. For each model, the mean DSC and mean IoU are shown with their standard deviations. The final two rows account for the raw and filtered combined bounding box results shown in Figure 3.11. The raw predictions compare the ground truth with the raw unfiltered results. Likewise, the filtered predictions compare the ground truth with the filtered results which only accounts for regions where at least five of the models agree upon an area. Though not the focus of this particular study, the same evaluation

metric used in Table 3.6 is utilized in Table 3.7 for evaluation of segmentation result for each of the models. For both tables, higher values of DSC, IoU, AP, and AR indicate better results.

Table 3.8 presents the comparison between three-channel and single-channel input data. The mean IoU and DSC results for the same models shown in Tables 3.1 and 3.2. Each listed model had a p-value of < .001, showing a statistically lower accuracy when compared to the results of the lumen segmentation model. Performance of the best plaque models are compared to the performance of the lumen model in Table 3.9.

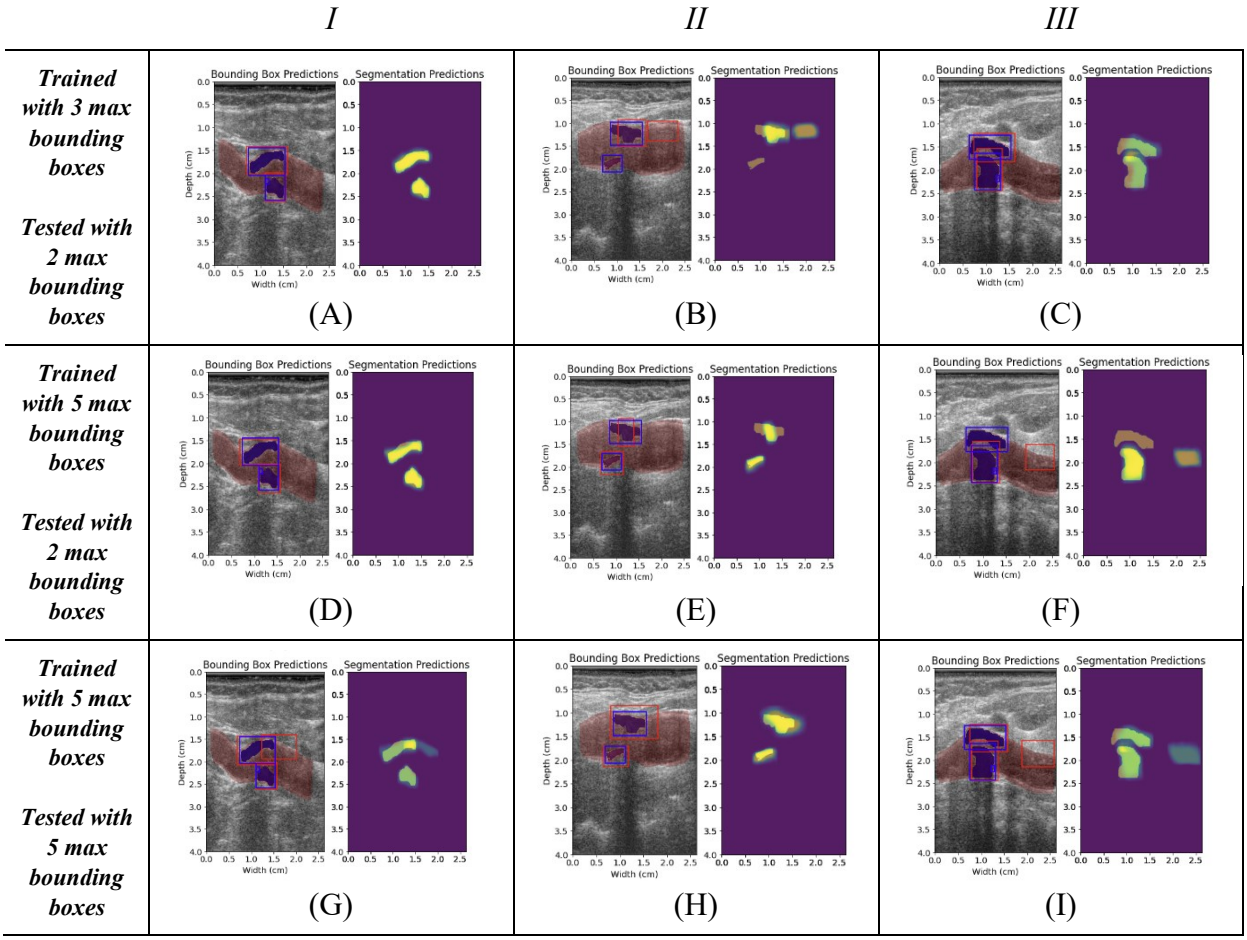

Figure 3.10: Example bounding box and segmentation results for three select cases for three models. A model trained on 3 boxes and tested on 2 boxes (A-C), 5 boxes and 2 boxes (D-F), and 5 boxes and 5 boxes (G-I). Images in columns *I, II,* and *III* correspond to the same test case.

I

II

III

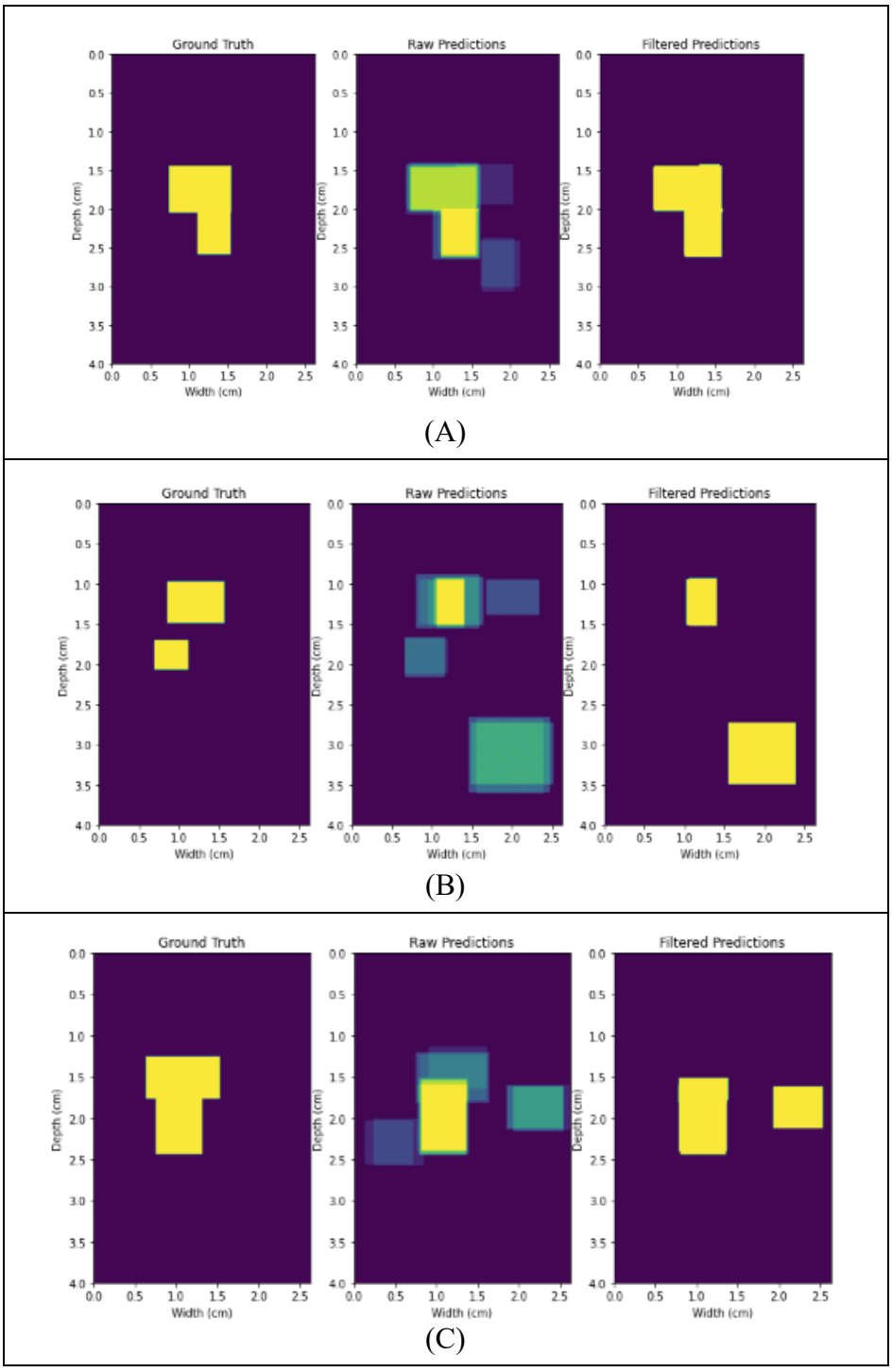

Figure 3.11. Bounding box analysis images. Ground truth, raw predictions, and filtered predictions for the corresponding cases in Figure 3.10. (A) image *I,* (B) image *II,* (C) image *III*

Max Training Boxes	Max Testing Boxes	DSC	IoU	AP IoU= 0.50:0.95	AP IoU=0.50	AP IoU=0.75	AR IoU= 0.50:0.95
1	*1*	0.62±0.22	0.48±0.22	0.107	0.215	0.074	0.128
2	*2*	0.72±0.20	0.59±0.22	0.165	0.331	0.156	0.202
3	*3*	0.69±0.18	0.56±0.20	0.171	0.338	0.170	0.216
4	*4*	0.65±0.17	0.51±0.20	0.165	0.335	0.146	0.212
5	*5*	0.67±0.19	0.53±0.19	0.165	0.345	0.144	0.217
1	*2*	0.72±0.20	0.60±0.22	0.163	0.349	0.115	0.201
3	*2*	0.72±0.19	0.60±0.22	0.165	0.324	0.171	0.207
4	*2*	0.71±0.20	0.59±0.22	0.160	0.318	0.143	0.203
5	*2*	0.74±0.17	0.61±0.20	0.159	0.334	0.140	0.205
Raw Combined		0.69±0.18	0.58±0.20				
Filtered Predictions		0.76±0.17	0.61±0.21				

Table 3.6. Network performance statistics for bounding box detection. Higher values indicate better results.

Max Training Boxes	Max Testing Boxes	DSC	IoU	AP IoU= 0.50:0.95	AP IoU=0.50	AP IoU=0.75	AR IoU= 0.50:0.95
1	*1*	0.54±0.20	0.40±0.18	0.082	0.209	0.046	0.102
2	*2*	0.62±0.18	0.47±0.18	0.116	0.297	0.056	0.148
3	*3*	0.60±0.17	0.45±0.17	0.120	0.302	0.061	0.156
4	*4*	0.57±0.17	0.41±0.16	0.120	0.309	0.054	0.160
5	*5*	0.58±0.19	0.43±0.17	0.120	0.318	0.060	0.158
1	*2*	0.62±0.18	0.48±0.17	0.117	0.301	0.059	0.152
3	*2*	0.62±0.18	0.47±0.18	0.116	0.290	0.062	0.151
4	*2*	0.62±0.18	0.47±0.18	0.117	0.305	0.050	0.153
5	*2*	0.64±0.16	0.49±0.16	0.119	0.313	0.061	0.153

Table 3.7. Network performance statistics for carotid plaque segmentation prediction.

Model	Dice	IoU
Three-Channel	0.69±0.21	0.56±0.22
Single Channel (B-Mode)	0.69±0.20	0.55±0.20

Table 3.8. Comparison of input data results using the best performing model (3 max training boxes and 2 max testing boxes).

Model	**DSC**	**IoU**	**AP IoU= 0.50:0.95**	**AP IoU=0.50**	**AP IoU=0.75**	**AR IoU= 0.50:0.95**
Lumen model	**0.89±0.07**	**0.81±0.11**	**0.62**	**0.98**	**0.68**	**0.68**
Best Plaque model	0.74±0.17	0.61±0.20	0.159	0.334	0.140	0.205
Filtered Plaque Predictions	0.76±0.17	0.61±0.21				

Table 3.9. Comparison of network performance results for Lumen and plaque models

3.4. Discussion

3.4.1 Lumen and Wall Model

The R-CNN model utilized for generating the lumen bounding box for each model combination produces relatively consistent results in cases where the carotid artery is the primary visualized vessel, and the B-mode image is free from significant acoustic shadowing.

The single-channel B-mode model produces the highest accuracy for both bounding box predictions and lumen segmentation predictions (Tables 3.1 and 3.2). Cases with less prominent carotid arteries or with significant acoustic shadowing have minimal impact on the accuracy of this model when compared to the other models tested. The multi-channel models consistently failed where the jugular vein is prominent, and the carotid artery is poorly visualized. The models

that incorporate SVD images produced the weakest agreement with the predicted bounding boxes overall and had the lowest accuracy in lumen segmentation. The B-mode plus SVD model was most susceptible to weakly visualized artery regions alongside either a prominent jugular vein or acoustic shadowing. When paired with MimickNet images, the SVD plus MimickNet model can handle acoustic shadowing better, but still struggles with a prominent jugular vein. The B-mode plus MimickNet model produces the second highest IoU and acceptable bounding boxes but produces segmentations with lower overall agreement with the ground truth segmentations. In general, segmentation predictions are less precise than the single channel B-mode case in regions of reduced vessel visualization. However, this is an acceptable finding as the detected bounding boxes would be utilized for ROI initialization for downstream task of plaque detection and segmentation.

The three-channel model, which incorporates all image types produces the second-best lumen segmentation results. The three-channel and two-channel models have similar limitations as described with the single channel model. Figures 3.5(a) and 3.6(a) depict the bounding box produced by the lumen R-CNNs that have reasonable agreement to the ground truth for the three-channel and single-channel models. The predicted segmentations for both the single channel (Fig. 3.9(a)) and three channel (Fig. 3.9(c)) are in reasonable agreement. Although the B-mode image does not exhibit significant contrast between the carotid lumen and the background, the R-CNN model still produces an acceptable bounding box and lumen segmentation result for both training methods. Figure 3.4(b) shows an instance where the three-channel R-CNN fails to accurately predict the carotid artery and instead generates the bounding box around the jugular vein, which is better visualized in this case. Figure 3.8(d) shows that the three-channel model attempts to segment both vessels in the region but misses the regions of the carotid lumen with poor

visualization. Figure 3.8(b) shows that the single-channel model can better predict the carotid lumen in this case but is still limited by the poorly visualized region of the artery on the left end of the segmentation.

On average, all models overestimated the dimensions of the bounding boxes in terms of area, width and height (Table 3.3 and Table 3.4). However, the best-performing model with the single channel B-mode stream as an input had only 10 % overestimation, which is an acceptable result, and these bounding boxes will be used to initialize a ROI for future plaque segmentation tasks. However, the cases where a model underestimates the size of a bounding box may reduce the usability in plaque localization. Therefore, the threshold used in the last column of Table 3.4 excludes cases where predicted bounding boxes are more than 10% smaller in any dimension than their respective ground truth as well as the threshold of 25 pixels between midpoints. The single-channel model had the most consistent performance in terms of the bounding box midpoint and MAPE results with 75.63% of the predictions satisfying the acceptable case criteria based on center point distance and bounding box dimension. Other models showed higher standard deviations and lower percentage of acceptable cases, especially in the case of the B-mode + SVD model (only 39.50% cases being acceptable, Table 3.4).

Our initial hypothesis was that the inclusion of SVD filtered images as an additional input channel to the network would provide additional information to the model that in turn will aid in localization of the carotid lumen. However, the results contradict this, with the best-performing model utilizing only the RF-derived B-mode images. We hypothesize the following reasons for such behavior. First, spatiotemporal SVD filtering was done using data collected at frame rate of 29 frames per second over a cardiac cycle which is significantly lower compared to the ultrafast ultrasound imaging applications where spatiotemporal SVD performs optimally. Second, low

order singular values were filtered in order to enhance arterial wall delineation while suppressing tissue signals. However, in several cases, the tissue signal suppression turned out to be quite strong resulting in lumen-like anechoic regions in the images. Furthermore, ultrasound texture information within plaque ROIs was in a few cases during the low-order SVD filtering which might have been valuable for the model to learn. We hypothesize that carotid ultrasound data collected at higher frame rate coupled with adaptive SVD filtering might provide better model performance in the future.

The dataset utilized in this study consists of very few cases with jugular vein visualization because the sonographer attempts to avoid visualization of the jugular vein when performing data collection. Further refinement of the training data with poorly visualized carotid artery regions and visualization of the jugular vein may help bounding box estimation in the low performance. Weighting of the different channels to favor the B-mode images more heavily in training may also improve network performance.

Meshram et al. [26] has previously reported on the use of user-defined bounding boxes for semantic carotid atherosclerotic plaque segmentations using both a U-net and dilated U-Net structure. Future work will aim to provide a means of automatically determining these plaque bounding boxes utilizing predicted lumen segmentation directly, such as in the calculation of Lumen diameter (LD), and carotid intima-media thickness (cIMT). The development of a modified Mask R-CNN model for carotid plaque segmentations is underway which incorporates training information from the lumen segmentation method described here.

Adjusting the network by utilizing non-resampled images produces an increase in accuracy compared to a previous iteration using a single-channel RF-derived B-mode Mask R-CNN for

prediction of the Carotid Lumen. Table 3.5 shows the network achieved a mean IoU of 0.84 for bounding-box detections and a mean IoU of 0.79 for lumen segmentation predictions. These results show an increase from our previous work, where the reported IoU for bounding box and segmentation predictions were 0.81 and 0.75 as seen in Tables 3.1 and 3.2 respectively. We also see less prediction variation in the improved model, with a greatly improved number of successful cases above an IoU threshold of 0.75. This is especially noticeable in the lumen segmentation prediction results.

3.4.2 Plaque Segmentation Model

Of the 9 carotid plaque test models trained and tested using different bounding box restrictions, the model trained with a maximum of five bounding boxes and tested on a maximum of two bounding boxes achieved the best performance based on DSC (0.74 for bounding box and 0.64 for segmentation) and IoU (0.61 for bounding box and 0.49 for segmentation). For each model of the Plaque Mask R-CNN presented here, the resulting mean bounding box DSC scores are consistent. The models, when limited to two bounding box predictions in testing, produce the best overall results for each model. However, the results of individual image scores vary amongst the different models as shown in Figure 3.10. Looking specifically at cases II and III, each of the three models produce differing results. Figure 3.10(c) shows good agreement for both plaque segments, while 3.2(f) include a false positive detection, as well as a false negative detection for the near wall plaque. For the models with 4 or 5 maximum bounding box predictions, many cases can end up with more False Positive detections than a model trained on 1, 2 or 3 bounding boxes as the maximum number of ground truth boxes in the dataset is 3. Because most dataset images have 1 or 2 plaque segments, when the models are limited to 2 boxes in testing, this limits the number of false positives seen and thus produces a better mean Dice score. In some instances, the 4 or 5

bounding box predictions can detect plaque segments left out by other models due to lower prediction confidence. This is seen in Figure 3.10(i) which recovers the near wall plaque lost in 3.10(f) but unfortunately still retains a false positive detection.

The variation seen between models is attributed to the limited variation within the training dataset. If the training is limited to too few bounding boxes, the network may predict a false positive region over a true positive due to less confidence. If the number of bounding boxes is increased, we may get the same false positive region, but it may also correctly detect the desired true positive region. Limiting the testing bounding boxes to 2 keeps the 2 most confident predictions from the trained model. For most cases such as Figure 3.10(I) this can reduce the prevalence of false positives but can also cause some false positives to replace true positive detections. As shown in Tables 3.6 and 3.7, this increases the mean DSC and IoU slightly compared to using a one-to-one ratio for maximum training and testing bounding boxes. A more comprehensive dataset would likely decrease the impact of this effect.

Table 3.8 shows a comparison between data input methods described in our previous work for the best of the 9 independent models (3 maximum training bounding boxes, 2 maximum test bounding boxes). Testing was performed for each of the 9 models, but no significant difference between models was observed as shown in Table 3.8. Thus, using our modified mask R-CNN for carotid plaque detection we do not see a significant accuracy difference between input methods previously observed for carotid lumen detection.

The incorporation of a method to combine the models seen in Figure 3.11 allows for an accumulation of the best results on an image-by-image basis. A mean Dice score of 0.76 allows for a consensus result for the Plaque Mask R-CNN model as these are the most agreed-upon results

for each model. However, as shown in Figure 3.11(b and c) there exists cases where too few models agree upon the correct region and/or too many models identify a false positive region. In both cases the model agreement is higher in false positive regions than in some 'true' regions. This does increase overall performance as shown in Table 3.6, but as a whole these models consistently provide erroneous results.

Although model results include inherent variability, the filtered combined bounding box results show that the models produce mostly similar results with only a small increase in DSC (0.76±0.17) compared to the best individual model (0.74±0.17) as shown in Table 3.9. This indicates that the plaque segmentation Mask R-CNN model cannot match the results of the lumen segmentation Mask R-CNN in its current state. This is most likely due to a higher variation of plaque presentation amongst patients compared to the carotid vessel lumen, which is typically more uniform. To achieve the same accuracy of the Lumen Mask R-CNN, we would need to incorporate more patients with varying plaque structures or perhaps restricting the search region to the vessel regions identified by the Lumen Mask R-CNN.

3.5 References

[1] M. J. Kiernan, R. Al Mukaddim, C. C. Mitchell, J. Maybock, S. M. Wilbrand, R. J. Dempsey, and T. Varghese, "Lumen segmentation using a Mask R-CNN in carotid arteries with stenotic atherosclerotic plaque," *Ultrasonics,* vol. 137, pp. 107193, Feb, 2024.

[2] M. Kiernan, R. A. Mukaddim, C. Mitchell, J. Maybock, S. Wilbrand, R. Dempsey, and T. Varghese, *Utilizing a mask R-CNN for segmentation of the carotid lumen in subjects with plaque deposition*, p.pp. MI: SPIE, 2024.

[3] C. Stefanadis, C. K. Antoniou, D. Tsiachris, and P. Pietri, "Coronary Atherosclerotic Vulnerable Plaque: Current Perspectives," *J Am Heart Assoc,* vol. 6, no. 3, 03 17, 2017.

[4] A. J. Lusis, "Atherosclerosis," *Nature,* vol. 407, no. 6801, pp. 233-41, Sep 14, 2000.

[5] F. B. Ahmad, J. A. Cisewski, A. Miniño, and R. N. Anderson, "Provisional Mortality Data - United States, 2020," *MMWR Morb Mortal Wkly Rep,* vol. 70, no. 14, pp. 519-522, 04 09, 2021.

[6] P. A. H. Organization, "Leading causes of mortality and health loss atregional, subregional, and country levels in the Region of the Americas,2000-2019," *ENLACE data portal*, 2021].

[7] C. W. Tsao, A. W. Aday, Z. I. Almarzooq, A. Alonso, A. Z. Beaton, M. S. Bittencourt, A. K. Boehme, A. E. Buxton, A. P. Carson, Y. Commodore-Mensah, M. S. V. Elkind, K. R. Evenson, C. Eze-Nliam, J. F. Ferguson, G. Generoso, J. E. Ho, R. Kalani, S. S. Khan, B. M. Kissela, K. L. Knutson, D. A. Levine, T. T. Lewis, J. Liu, M. S. Loop, J. Ma, M. E. Mussolino, S. D. Navaneethan, A. M. Perak, R. Poudel, M. Rezk-Hanna, G. A. Roth, E. B. Schroeder, S. H. Shah, E. L. Thacker, L. B. VanWagner, S. S. Virani, J. H. Voecks, N.-Y. Wang, K. Yaffe, and S. S. Martin, "Heart Disease and Stroke Statistics—2022 Update: A Report From the American Heart Association," *Circulation,* vol. 145, no. 8, pp. e153-e639, 2022.

[8] V. Canudas-Romo, "Three measures of longevity: time trends and record values," *Demography,* vol. 47, no. 2, pp. 299-312, May, 2010.

[9] D. Kuriakose, and Z. Xiao, "Pathophysiology and Treatment of Stroke: Present Status and Future Perspectives," *Int J Mol Sci,* vol. 21, no. 20, Oct 15, 2020.

[10] N. H. Meshram, D. Jackson, T. Varghese, C. C. Mitchell, S. M. Wilbrand, R. J. Dempsey, and B. P. Hermann, "A Cross-Sectional Investigation of Cognition and Ultrasound-Based Vascular Strain Indices," *Arch Clin Neuropsychol,* vol. 35, no. 1, pp. 46-55, Jan 24, 2019.

[11] R. J. Dempsey, R. Vemuganti, T. Varghese, and B. P. Hermann, "A review of carotid atherosclerosis and vascular cognitive decline: a new understanding of the keys to symptomology," *Neurosurgery,* vol. 67, no. 2, pp. 484-93; discussion 493-4, Aug, 2010.

[12] C. L. de Korte, S. Fekkes, A. J. Nederveen, R. Manniesing, and H. R. Hansen, "Review: Mechanical Characterization of Carotid Arteries and Atherosclerotic Plaques," *IEEE Trans Ultrason Ferroelectr Freq Control,* vol. 63, no. 10, pp. 1613-1623, 10, 2016.

[13] P. N. T. Wells, "Current status and future technical advances of ultrasonic imaging," *IEEE Engineering in Medicine and Biology Magazine,* vol. 19, no. 5, pp. 14-20, 2000.

[14] G. L. ten Kate, E. J. Sijbrands, D. Staub, B. Coll, F. J. ten Cate, S. B. Feinstein, and A. F. Schinkel, "Noninvasive imaging of the vulnerable atherosclerotic plaque," *Curr Probl Cardiol,* vol. 35, no. 11, pp. 556-91, Nov, 2010.

[15] G. Geroulakos, G. Ramaswami, A. Nicolaides, K. James, N. Labropoulos, G. Belcaro, and M. Holloway, "Characterization of symptomatic and asymptomatic carotid plaques using high-resolution real-time ultrasonography," *Br J Surg,* vol. 80, no. 10, pp. 1274-7, Oct, 1993.

[16] N. H. Meshram, T. Varghese, C. C. Mitchell, D. C. Jackson, S. M. Wilbrand, B. P. Hermann, and R. J. Dempsey, "Quantification of carotid artery plaque stability with multiple region of interest based ultrasound strain indices and relationship with cognition," *Phys Med Biol,* vol. 62, no. 15, pp. 6341-6360, Jul 17, 2017.

[17] X. Wang, D. C. Jackson, C. C. Mitchell, T. Varghese, S. M. Wilbrand, B. G. Rocque, B. P. Hermann, and R. J. Dempsey, "Classification of Symptomatic and Asymptomatic Patients with and without Cognitive Decline Using Non-invasive Carotid Plaque Strain Indices as Biomarkers," *Ultrasound Med Biol,* vol. 42, no. 4, pp. 909-18, Apr, 2016.

[18] M. H. Roy Cardinal, M. H. G. Heusinkveld, Z. Qin, R. G. P. Lopata, C. Naim, G. Soulez, and G. Cloutier, "Carotid Artery Plaque Vulnerability Assessment Using Noninvasive Ultrasound Elastography: Validation With MRI," *AJR Am J Roentgenol,* vol. 209, no. 1, pp. 142-151, Jul, 2017.

[19] A. A. Khan, S. Sikdar, T. Hatsukami, J. Cebral, M. Jones, J. Huston, G. Howard, and B. K. Lal, "Noninvasive characterization of carotid plaque strain," *J Vasc Surg,* vol. 65, no. 6, pp. 1653-1663, Jun, 2017.

[20] C. L. de Korte, J. A. Schaar, F. Mastik, P. W. Serruys, and A. F. van der Steen, "Intravascular elastography: from bench to bedside," *J Interv Cardiol,* vol. 16, no. 3, pp. 253-9, Jun, 2003.

[21] R. A. Baldewsing, J. A. Schaar, C. L. de Korte, F. Mastik, P. W. Serruys, and A. F. van der Steen, "Intravascular Ultrasound Elastography: A Clinician's Tool for Assessing Vulnerability and Material Composition of Plaques," *Stud Health Technol Inform,* vol. 113, pp. 75-96, 2005.

[22] J. C. Kohn, M. C. Lampi, and C. A. Reinhart-King, "Age-related vascular stiffening: causes and consequences," *Front Genet,* vol. 6, pp. 112, 2015.

[23] M. McCormick, T. Varghese, X. Wang, C. Mitchell, M. A. Kliewer, and R. J. Dempsey, "Methods for robust in vivo strain estimation in the carotid artery," *Phys Med Biol,* vol. 57, no. 22, pp. 7329-53, Nov 21, 2012.

[24] N. H. Meshram, and T. Varghese, "GPU Accelerated Multilevel Lagrangian Carotid Strain Imaging," *IEEE Trans Ultrason Ferroelectr Freq Control,* vol. 65, no. 8, pp. 1370-1379, Aug, 2018.

[25] S. E. Berman, X. Wang, C. C. Mitchell, B. Kundu, D. C. Jackson, S. M. Wilbrand, T. Varghese, B. P. Hermann, H. A. Rowley, S. C. Johnson, and R. J. Dempsey, "The relationship between carotid artery plaque stability and white matter ischemic injury," *Neuroimage Clin,* vol. 9, pp. 216-22, 2015.

[26] N. H. Meshram, C. C. Mitchell, S. Wilbrand, R. J. Dempsey, and T. Varghese, "Deep Learning for Carotid Plaque Segmentation using a Dilated U-Net Architecture," *Ultrason Imaging,* vol. 42, no. 4-5, pp. 221-230, 2020 Jul-Sep, 2020.

[27] M. McCormick, N. Rubert, and T. Varghese, "Bayesian regularization applied to ultrasound strain imaging," *IEEE Trans Biomed Eng,* vol. 58, no. 6, pp. 1612-20, Jun, 2011.

[28] M. Xie, Y. Li, Y. Xue, L. Huntress, W. Beckerman, S. Rahimi, J. Ady, and U. Roshan, "Vessel lumen segmentation in carotid artery ultrasounds with the U-Net convolutional neural network." pp. 2680-2684.

[29] F. MOLINARI, W. LIBONI, P. GIUSTETTO, S. BADALAMENTI, and J. S. SURI, "AUTOMATIC COMPUTER-BASED TRACINGS (ACT) IN LONGITUDINAL 2-D ULTRASOUND IMAGES USING DIFFERENT SCANNERS," *Journal of Mechanics in Medicine and Biology,* vol. 09, no. 04, pp. 481-505, 2009.

[30] M. C. Bastida-Jumilla, R. M. Menchón-Lara, J. Morales-Sánchez, R. Verdú-Monedero, J. Larrey-Ruiz, and J. L. Sancho-Gómez, "Segmentation of the common carotid artery walls based on a frequency implementation of active contours: segmentation of the common carotid artery walls," *J Digit Imaging,* vol. 26, no. 1, pp. 129-39, Feb, 2013.

[31] C. P. Loizou, C. S. Pattichis, A. N. Nicolaides, and M. Pantziaris, “Manual and automated media and intima thickness measurements of the common carotid artery,” *IEEE Trans Ultrason Ferroelectr Freq Control,* vol. 56, no. 5, pp. 983-94, May, 2009.

[32] C. P. Loizou, T. Kasparis, C. Spyrou, and M. Pantziaris, "Integrated System for the Complete Segmentation of the Common Carotid Artery Bifurcation in Ultrasound Images," *Artificial Intelligence Applications and Innovations.* pp. 292-301.

[33] J. H. Stein, C. E. Korcarz, M. E. Mays, P. S. Douglas, M. Palta, H. Zhang, T. Lecaire, D. Paine, D. Gustafson, and L. Fan, “A semiautomated ultrasound border detection program that facilitates clinical measurement of ultrasound carotid intima-media thickness,” *J Am Soc Echocardiogr,* vol. 18, no. 3, pp. 244-51, Mar, 2005.

[34] F. Faita, V. Gemignani, E. Bianchini, C. Giannarelli, L. Ghiadoni, and M. Demi, “Real-time measurement system for evaluation of the carotid intima-media thickness with a robust edge operator,” *J Ultrasound Med,* vol. 27, no. 9, pp. 1353-61, Sep, 2008.

[35] R. Zhou, M. R. Azarpazhooh, J. D. Spence, S. Hashemi, W. Ma, X. Cheng, H. Gan, M. Ding, and A. Fenster, “Deep Learning-Based Carotid Plaque Segmentation from B-Mode Ultrasound Images,” *Ultrasound Med Biol,* vol. 47, no. 9, pp. 2723-2733, 09, 2021.

[36] R. Zhou, Y. Ou, X. Fang, M. R. Azarpazhooh, H. Gan, Z. Ye, J. D. Spence, X. Xu, and A. Fenster, “Ultrasound carotid plaque segmentation via image reconstruction-based self-supervised learning with limited training labels,” *Math Biosci Eng,* vol. 20, no. 2, pp. 1617-1636, Jan, 2023.

[37] E. Ukwatta, J. Awad, A. D. Ward, D. Buchanan, J. Samarabandu, G. Parraga, and A. Fenster, “Three-dimensional ultrasound of carotid atherosclerosis: Semiautomated segmentation using a level set-based method,” *Medical Physics,* vol. 38, no. 5, pp. 2479-2493, 2011.

[38] F. Molinari, K. M. Meiburger, L. Saba, U. R. Acharya, G. Ledda, G. Zeng, S. Y. Ho, A. T. Ahuja, S. C. Ho, A. Nicolaides, and J. S. Suri, “Ultrasound IMT measurement on a multi-ethnic and multi-institutional database: our review and experience using four fully automated and one semi-automated methods,” *Comput Methods Programs Biomed,* vol. 108, no. 3, pp. 946-60, Dec, 2012.

[39] X. Yang, J. Jin, M. Xu, H. Wu, W. He, M. Yuchi, and M. Ding, “Ultrasound common carotid artery segmentation based on active shape model,” *Comput Math Methods Med,* vol. 2013, pp. 345968, 2013.

[40] D. D. Carvalho, Z. Akkus, S. C. van den Oord, A. F. Schinkel, A. F. van der Steen, W. J. Niessen, J. G. Bosch, and S. Klein, “Lumen segmentation and motion estimation in B-mode and contrast-enhanced ultrasound images of the carotid artery in patients with atherosclerotic plaque,” *IEEE Trans Med Imaging,* vol. 34, no. 4, pp. 983-93, Apr, 2015.

[41] P. K. Jain, S. Gupta, A. Bhavsar, A. Nigam, and N. Sharma, “Localization of common carotid artery transverse section in B-mode ultrasound images using faster RCNN: a deep learning approach,” *Med Biol Eng Comput,* vol. 58, no. 3, pp. 471-482, Mar, 2020.

[42] C. Qian, E. Su, and X. Ni, “Learning-based initialization for correntropy-based level sets to segment atherosclerotic plaque in ultrasound images,” *Ultrasonics,* vol. 127, pp. 106826, Jan, 2023.

[43] J. Yang, M. Faraji, and A. Basu, “Robust segmentation of arterial walls in intravascular ultrasound images using Dual Path U-Net,” *Ultrasonics,* vol. 96, pp. 24-33, Jul, 2019.

[44] J. H. Park, E. Seo, W. Choi, and S. J. Lee, “Ultrasound deep learning for monitoring of flow-vessel dynamics in murine carotid artery,” *Ultrasonics,* vol. 120, pp. 106636, Mar, 2022.

[45] H. Nahas, B. Y. S. Yiu, A. J. Y. Chee, J. S. Au, and A. C. H. Yu, “Deep-learning-assisted and GPU-accelerated vector Doppler imaging with aliasing-resistant velocity estimation,” *Ultrasonics,* vol. 134, pp. 107050, Sep, 2023.

[46] N. H. Meshram, C. C. Mitchell, S. M. Wilbrand, R. J. Dempsey, and T. Varghese, “In vivo carotid strain imaging using principal strains in longitudinal view,” *Biomed Phys Eng Express,* vol. 5, no. 3, 2019.

[47] W. Ge, C. G. Krueger, A. Weichmann, D. Shanmuganayagam, and T. Varghese, “Displacement and strain estimation for evaluation of arterial wall stiffness using a familial hypercholesterolemia swine model of atherosclerosis,” *Med Phys,* vol. 39, no. 7, pp. 4483-92, Jul, 2012.

[48] N. H. Meshram, C. C. Mitchell, S. M. Wilbrand, R. J. Dempsey, and T. Varghese, “carotid strain imaging using principal strains in longitudinal view,” *Biomed Phys Eng Express,* vol. 5, no. 3, 2019.

[49] R. J. Dempsey, T. Varghese, D. C. Jackson, X. Wang, N. H. Meshram, C. C. Mitchell, B. P. Hermann, S. C. Johnson, S. E. Berman, and S. M. Wilbrand, “Carotid atherosclerotic plaque instability and cognition determined by ultrasound-measured plaque strain in asymptomatic patients with significant stenosis,” *J Neurosurg,* vol. 128, no. 1, pp. 111-119, Jan, 2018.

[50] J. Redmon, S. Divvala, R. Girshick, and A. Farhadi, “You Only Look Once: Unified, Real-Time Object Detection,” in 2016 IEEE Conference on Computer Vision and Pattern Recognition (CVPR), 2016, pp. 779-788.

[51] W. Liu, D. Anguelov, D. Erhan, C. Szegedy, S. Reed, C.-Y. Fu, and A. C. Berg, "SSD: Single Shot MultiBox Detector." pp. 21-37.

[52] N. Carion, F. Massa, G. Synnaeve, N. Usunier, A. Kirillov, and S. Zagoruyko, "End-to-End Object Detection with Transformers." pp. 213-229.

[53] R. Girshick, "Fast R-CNN." pp. 1440-1448.

[54] K. He, G. Gkioxari, P. Dollár, and R. Girshick, "Mask R-CNN." pp. 2980-2988.

[55] T.-Y. Lin, M. Maire, S. Belongie, J. Hays, P. Perona, D. Ramanan, P. Dollár, and C. L. Zitnick, "Microsoft COCO: Common Objects in Context." pp. 740-755.

[56] O. Huang, W. Long, N. Bottenus, M. Lerendegui, G. E. Trahey, S. Farsiu, and M. L. Palmeri, “MimickNet, Mimicking Clinical Image Post- Processing Under Black-Box Constraints,” *IEEE Trans Med Imaging,* vol. 39, no. 6, pp. 2277-2286, Jun, 2020.

[57] H. Hasegawa, and R. Nagaoka, “Singular value decomposition filter for speckle reduction in adaptive ultrasound imaging,” *Japanese Journal of Applied Physics,* vol. 58, pp. SGGE06, 07/01, 2019.

[58] J. Tierney, J. Baker, D. Brown, D. Wilkes, and B. Byram, "Independent Component-Based Spatiotemporal Clutter Filtering for Slow Flow Ultrasound," *IEEE Trans Med Imaging,* vol. 39, no. 5, pp. 1472-1482, May, 2020.

[59] P. Song, J. D. Trzasko, A. Manduca, B. Qiang, R. Kadirvel, D. F. Kallmes, and S. Chen, "Accelerated Singular Value-Based Ultrasound Blood Flow Clutter Filtering With Randomized Singular Value Decomposition and Randomized Spatial Downsampling," *IEEE Transactions on Ultrasonics, Ferroelectrics, and Frequency Control,* vol. 64, no. 4, pp. 706-716, 2017.

[60] R. Al Mukaddim, A. M. Weichmann, C. C. Mitchell, and T. Varghese, "Enhancement of in vivo cardiac photoacoustic signal specificity using spatiotemporal singular value decomposition," *J Biomed Opt,* vol. 26, no. 4, Apr, 2021.

Chapter 4: Comparison of Carotid Intima-Media Thickness Measurements with Lagrangian Strain Estimation

4.1 Background

4.1.1 Carotid Intima-Media Thickness Measurement Background

Carotid Intima-Media Thickness (IMT) measurement is a widely recognized non-invasive technique used to evaluate cardiovascular disease (CVD) risk. Cardiovascular diseases remain the leading cause of death worldwide,[1] making early detection and prevention essential for reducing the associated health burden. IMT serves as an early marker of subclinical atherosclerosis by measuring the thickness of the two innermost layers of the arterial wall: the intima and the media. Changes in these layers often precede the development of visible atherosclerotic plaques, making IMT a valuable tool for assessing arterial wall health before significant structural damage occurs.

IMT is commonly measured in the common carotid artery (CCA) due to its accessibility and reproducibility. Using high-resolution B-mode ultrasonography, clinicians and researchers capture detailed images of the arterial wall, focusing on the far wall of the CCA for accurate and consistent measurements. The technique typically involves measuring the distal one centimeter of the CCA's far wall at multiple angles, with the mean and maximum IMT values calculated to represent overall thickness. This standardization has facilitated widespread use in clinical and research settings, making IMT a cornerstone metric in vascular health studies.

4.1.2 Lagrangian Strain Estimation Background

Strain estimation is an advanced imaging technique that provides valuable insights into the mechanical properties of arterial walls,[2, 3] complementing traditional methods like Carotid IMT measurement. Unlike IMT, which focuses on structural changes, strain estimation evaluates how arterial walls deform in response to forces such as blood pressure during the cardiac cycle. This assessment of arterial compliance—the ability of vessels to expand and contract—offers a dynamic perspective on vascular health, making it a promising tool for early detection of cardiovascular disease (CVD).

The concept of strain estimation is rooted in the measurement of deformation, typically expressed as a percentage change in length relative to its original state. Strain can be categorized into axial strain (deformation along the vessel's length), lateral strain (deformation perpendicular to the blood flow), and shear strain (distortions caused by opposing forces within the vessel wall). These parameters provide a comprehensive view of the mechanical behavior of arteries under varying physiological conditions. Strain maps and indices offer a nuanced understanding of vascular health, highlighting areas of reduced arterial compliance that may indicate early pathological changes.

4.2 Motivation for Use of Lagrangian Strain Estimation in Risk Assessment

The motivation for this project lies in the critical need to enhance our understanding of early indicators of arterial health to prevent or mitigate cardiovascular disease. By investigating the relationships between arterial wall structure, as assessed by carotid IMT, and mechanical properties, measured through Lagrangian arterial strain, in a cohort of healthy young adults, this

study aims to bridge the gap between structural and mechanical markers of vascular health. The focus on how these measures correlate with traditional cardiovascular risk factors highlights the potential of novel strain indices as a research tool to detect early arterial changes, ultimately contributing to the development of more effective strategies for early intervention and prevention of arterial injury.

4.3 Materials and Methods

4.3.1 Lagrangian Strain Estimation Model Architecture

In this study, we will employ Lagrangian strain estimation initially proposed by Shi et al. (2008)[4] and further developed in McCormick et al. (2012), [5] and later adapted for GPU acceleration by Meshram et al. (2018)[6]. The strain estimation algorithm utilizes radiofrequency (RF) data collected using an Acuson S2000 system (Siemens Ultrasound, Mountain View, CA, USA) to calculate strain distribution and quantitative strain indices within defined segmented regions. This process relies on binary segmentations of plaque regions performed on RF-derived B-mode images and employs a three-level pyramidal hierarchy for displacement tracking, ultimately resulting in the calculation of the Lagrangian strain tensor from the accumulated displacement vectors. The GPU implementation is executed using an NVIDIA K40 GPU with CUDA programming, as described by Meshram et al. (2018)[6].

The hierarchical approach involves three levels, each with a different degree of decimation corresponding to a Gaussian filter with a variance of $(f/2)^2$ where (f) is the decimation factor. Higher levels of decimation are possible in the axial or beam direction due to denser image content, with broader structures being retained at higher levels, while finer structures are preserved at the lowest level, which consists of RF data. Envelope data is used at higher levels to maintain the

overall structure and adhere to the Nyquist criterion. The matching blocks within each level decrease in size linearly from coarse to fine, without overlapping with neighboring blocks. This approach reduces the computational burden, mitigates correlated artifacts and aids in regularization.

Displacement matching involves interpolating displacements at coarser levels to initialize searches at lower levels. To prevent peak-hopping errors, which occur when the correlation coefficient peaks select speckle decorrelation peaks instead of the true peak, a strain image is generated. Pixels with strain magnitudes exceeding a 7.5% threshold are marked for replacement, with these pixels being linearly interpolated across errant regions or extrapolated from valid data near the edges.
Block scaling addresses decorrelation across frames within a block, partially due to strain. Strain at higher levels can be used to stretch or compress the matching block before cross-correlation, reducing decorrelation by resampling the matching blocks with a scaling factor and windowed-sinc interpolation. The scaling factor is adjusted based on the normal strain in the relevant direction, particularly when strain is low, resulting in an improved strain signal-to-noise ratio (SNR).

The algorithm utilizes Dynamic frame skipping, where the amount of deformation between images in a sequence influences the overall SNR[7]. Due to varying loads on the region of interest (ROI) throughout the cardiac cycle, the frame skip length must adjust according to the cardiac phase—shorter during high strain rates and longer when strain rates are low. At the lowest level, strain is estimated using a least squares gradient over a 3x3 pixel region. The strain sequence is calculated over the cardiac cycle, using the end-diastolic state as a reference.

Indices	Description	Physical significance
Axial Strain	Identifies how well vessel walls respond to forces in the axial direction (perpendicular to blood flow)	
Lateral Strain	Identifies how well vessel walls respond to forces in the lateral (longitudinal) direction (parallel to blood flow)	
Shear strain	Identifies how well vessel walls respond to opposing axial and lateral forces parallel to the surface that can cause angular deformation or distortions.	
Peak Strain Index	Highest strain index for a given image. If we have N ROI and P frames, $$PSI = \underset{i=1}{\overset{N}{Max}} \; \underset{k=1}{\overset{P}{Max}} |R_{ki}|$$ where R_{ki} is the average strain value of the i^{th} ROI in k^{th} frame.	Indicates maximum strain peak over a given cardiac cycle.
Global peak to peak (GPTP)	Difference between the maximum or minimum accumulated average value across ROIs If we have N ROI and P frames. $$GPTP = \underset{i=1}{\overset{N}{Max}} \; \underset{k=1}{\overset{P}{Max}} R_{ki} - \underset{j=1}{\overset{N}{Max}} \; \underset{k=1}{\overset{P}{Max}} R_{kj}$$ Where R_{ki} is the average strain value of the i^{th} ROI in k^{th} frame.	Net temporal strain fluctuation among the unstable ROI
Average L-1 Norm (AL1N)	Average L-1 norm of the difference in the average strain values in all ROI's with average strain value in entire region. This is done per frame over a cardiac cycle. Then the average of all the L-1 norm estimates is computed. If we have N ROIs and P frames, $$AL1N = \frac{1}{NP}\sum_{j=1}^{N}\sum_{i=1}^{P}\left|R_{ij} - P_i\right|$$ where, R_{ij} is the average strain value of j^{th} ROI in the i^{th} frame and P_i is the average strain value of the entire plaque region in the i^{th} frame	Average additional strain in the unstable regions compared to overall strain

Table 4.1. Relevant strain descriptors

Accumulated displacement and Lagrangian strain are calculated according to a mesh created from the binary segmentation mask provided by an expert sonographer, with strain and displacement for each point interpolated and added to the accumulated values for every frame.

The visualization of strain within the vessel walls is crucial for identifying vulnerable sections that may rupture, with the plaque's composition, size, and location influencing its susceptibility. Scalar

strain indices are obtained from the Lagrangian strain tensor via Eigen analysis. Table 4.1 describes the principal strains and the indices used in this study. For each strain type, the mean peak strain index, mean global peak to peak index and average L1 norm were calculated for each participant for a total 9 strain parameters.

4.3.2 Volunteer Subject Requirements and Data Selection

The cohort for this study consisted of 80 healthy individuals (40 men and 40 women) aged 25-50 (mean 35) who volunteered to participate in a research study performed at the University of Wisconsin-Madison from December 2021 to August 2023. The only requirement for the study was that volunteers could not be actively undergoing treatment for CVD (hypertension or dyslipidemia) or history of a major cardiovascular event (stroke, TIA, or cardiac symptoms). Collected data included age (years), sex, body-mass index (kg/m^2) smoking status, blood pressure (mmHg), lipid panel (total cholesterol ,high-density lipoprotein cholesterol [HDL-C], low-density lipoprotein cholesterol [LDL-C] , and triglycerides measured in mg/dL), high-sensitivity C-Reactive Protein (mg/L), and hemoglobin A1c (mg/dL). Blood work and health history were collected to assess cardiovascular risk factors.

4.3.3 Carotid Intima-Media Thickness Protocol

The clinical imaging component of the study was conducted using an Acuson S2000 ultrasound system (Siemens Medical Solutions USA, Inc., Malvern, PA, USA) equipped with a 9L4 transducer (Siemens Medical Solutions, Malvern, PA, USA). The ultrasound protocol included both transverse and longitudinal imaging of the common carotid artery (CCA), carotid bulb, and internal and external carotid arteries. Pulsed wave Doppler velocities were obtained from the proximal, mid-, and distal segments of the CCA, the carotid bulb, and the internal and external carotid arteries. If plaque was present, the location was noted and documented. Color Doppler

imaging was performed in both transverse and longitudinal planes across the same vascular structures. All images were stored digitally in Digital Imaging and Communications in Medicine (DICOM) format.[8] These images were subsequently imported into the Syngo Ultrasound Workplace reading stations at the University of Wisconsin Atherosclerosis Imaging Research Program, MESA Carotid Ultrasound Reading Center. Carotid intima-media thickness (IMT) was measured using Arterial Health Package software (Siemens Medical, Malvern, PA, USA). The distal one centimeter of the right and left common carotid artery far wall was measured in triplicate from two different angles. The mean of the mean and mean of the max IMT was then calculated from both the right and left sides.[4, 9, 10]

4.3.4 Statistical Analysis

Spearman's ρ (rho) correlations were used to examine the relationships between CCA IMT and axial, lateral and shear strain indices. Multiple regression analysis was used to examine relationships between axial, lateral and shear strain indices or CIMT measurements with cardiovascular risk factors. The model included the cardiovascular risk factors of age, sex, body-mass index, smoking status, systolic blood pressure, diastolic blood pressure, total cholesterol, high-density lipoprotein cholesterol, low-density lipoprotein cholesterol, triglycerides, high-sensitivity C-reactive protein, and hemoglobin A1c compared individually with CCA intima-media thickness measurements (mean of the mean and mean of the max) and axial, lateral and shear strain indices. Mann-Whitney U tests were used to examine differences by sex in CVD risk factors (age, BMI, systolic blood pressure, diastolic blood pressure, total cholesterol, HDL-C, LDL-C, triglycerides, high-sensitivity C-reactive protein, and hemoglobin A1c). One volunteer did not have a reported BMI. In cases where BMI is included in the model, an N of 79 is used.

4.4 Results

4.4.1 Participants Characteristics

Participants were median (IQR) age 35 (13.25) years, 50% female, 1 (1%) were American Indian, 4(5%) were Hispanic, 9(11%) were Asian/Asian American, 1(1%) were mixed race and 64 (80%) were white. All baseline participant characteristics are presented in Table 4.2.

	N	Median (inter-quartile range)	Range
Age, y	80	35 (13.25)	23-50
Sex (n, %)	80		
Male		40 (50.0%)	
Female		40 (50.0%)	
Body-mass Index (kg/m^2)	79	25.7 (7.75)	17.5-51
Smoking Status	80		
Never (n, %)		68 (85%)	
Former (n, %)		7 (8.75%)	
Current (n, %)		5 (6.25%)	
Systolic Blood Pressure (mmHg)	80	128.5 (23)	103-153
Diastolic Blood Pressure (mmHg)	80	79.5 (18)	61-100
Total Cholesterol (mg/dL)	80	182.5 (48.5)	114-298
High-density lipoprotein cholesterol (mg/dL)	80	49 (17)	25-88
Low-density lipoprotein cholesterol (mg/dL)	80	113.5 (44)	59-219
Triglycerides (mg/dL)	80	81 (57.5)	32-324
High-sensitivity C-Reactive Protein (mg/L)	80	1 (2.525)	0.299-17.9
Hemoglobin A1c (mg/dL)	80	5.2 (0.4)	4.8-6
CCA IMT Mean of the mean (mm)	80	0.512 (0.081)	0.387-0.742
CCA IMT Mean of the Max (mm)	80	0.633 (0.091)	0.485-0.911
Axial Strain: Mean Peak Strain	80	27.53 (26.74)	9.563-101.7
Axial Strain: Mean Peak-to-Peak Strain	80	8.123(7.994)	1.933-35.37
Axial Strain: Average L1-Norm	80	33.75 (29.74)	11.154-109.07
Lateral Strain: Mean Peak Strain	80	9.581 (7.076)	3.73-36.2
Lateral Strain: Mean Peak-to-Peak Strain	80	13.72(11.75)	4.443-48.61
Lateral Strain: Average L1-Norm	80	3.659 (2.964)	1.057-18.61
Shear Strain: Mean Peak Strain	80	28.88 (23.62)	9.744-92.71
Shear Strain: Mean Peak-to-Peak Strain	80	39.89 (31.25)	11.457-122.56
Shear Strain: Average L1-Norm	80	8.545(10.19)	3.361-42.05

Table 4.2. Participant Characteristics. Participant characteristics of volunteer dataset.

4.4.2 Correlations between Carotid Intima-Media Thickness and Lagrangian Strain Indices

No statistically significant associations were found between carotid IMT and strain of the CCA as shown in Table 4.3. All reported strain metrics had a p value greater than 0.05.

	CCA IMT Mean of the Mean		CCA IMT Mean of the Max	
	ρ	*P* value	ρ	*P* value
Axial Strain: Mean Peak Strain	-0.071	0.530	-0.066	0.561
Axial Strain: Mean Peak-to-Peak Strain	-0.008	0.943	-0.018	0.873
Axial Strain: Average L1-Norm	0.033	0.769	0.028	0.807
Lateral Strain: Mean Peak Strain	0.011	0.920	0.031	0.783
Lateral Strain: Mean Peak-to-Peak Strain	0.053	0.643	0.058	0.608
Lateral Strain: Average L1-Norm	0.021	0.854	0.047	0.679
Shear Strain: Mean Peak Strain	-0.012	0.91	-0.002	0.984
Shear Strain: Mean Peak-to-Peak Strain	-0.041	0.717	-0.031	0.782
Shear Strain: Average L1-Norm	-0.023	0.839	-0.001	0.996

Table 4.3. Spearman's rho correlations between carotid intima-media thickness measurements and Strain indices of the Common Carotid Artery.

4.4.3 Carotid Intima-Media Thickness and Cardiovascular Risk Factor Associations

Variable	β (95% CI)	*P* Value
CCA IMT Mean of the Max		
Age, y	0.005 (0.003,0.007)	**<0.001***
Sex	0.012 (-0.023,0.048)	0.5005
Body-mass Index (kg/m^2)	0.004 (0.001,0.007)	**0.004***
Smoking Status	0.021 (-0.045,0.087)	0.5234
Systolic Blood Pressure (mmHg)	0.001 (-0.000,0.003)	0.1014
Diastolic Blood Pressure (mmHg)	0.0001 (-0.002,0.002)	0.8901
Total Cholesterol (mg/dL)	-0.008 (-0.015,-0.002)	**0.008***
High-density lipoprotein cholesterol (mg/dL)	0.008 (0.002,0.014)	**0.009***
Low-density lipoprotein cholesterol (mg/dL)	0.008 (0.002,0.015)	**0.009***
Triglycerides (mg/dL)	0.001 (-0.000,0.002)	0.053
High-sensitivity C-Reactive Protein (mg/L)	-0.0006 (-0.006,0.004)	0.817
Hemoglobin A1c (mg/dL)	0.081 (0.019,0.142)	**0.011***
CCA IMT Mean of the Mean		
Age, y	0.005 (0.003,0.006)	**<0.001***
Sex	0.015 (-0.014,0.045)	0.310
Body-mass Index (kg/m^2)	0.004 (0.001,0.006)	**0.002***
Smoking Status	0.010 (-0.044,0.065)	0.705
Systolic Blood Pressure (mmHg)	0.001 (-0.000,0.003)	0.062
Diastolic Blood Pressure (mmHg)	-0.0001 (-0.002,0.002)	0.888
Total Cholesterol (mg/dL)	-0.008 (-0.013,-0.003)	**0.004***
High-density lipoprotein cholesterol (mg/dL)	0.007 (0.002,0.012)	**0.005***
Low-density lipoprotein cholesterol (mg/dL)	0.008 (0.002,0.013)	**0.005***
Triglycerides (mg/dL)	0.001 (0.000,0.002)	**0.027***
High-sensitivity C-Reactive Protein (mg/L)	0.0003 (-0.004,0.004)	0.898
Hemoglobin A1c (mg/dL)	0.060 (0.008,0.111)	**0.023***

Table 4.4. Associations of intima-media thickness measurements of the common carotid artery walls with Cardiovascular Disease Risk Factors.
* *P* values less than 0.05.

Statistically significant relationships between carotid IMT measurements and several CVD risk factors were identified (all p values <0.05). Carotid IMT measurements, mean of the mean and max of the mean, were statistically significantly associated with age, body-mass index, LDL-C, and hemoglobin A1c. Carotid IMT measurements were significantly inversely associated with total cholesterol. The mean of the mean carotid IMT also demonstrated an inverse association with triglycerides (Table 4.4).

4.4.4 Lagrangian Strain Indices and Cardiovascular Risk Factor Associations

Variable	β (95% CI)	*P* Value
Axial Strain: Mean Peak Strain		
Age, y	-0.697(-1.182,-0.212)	**0.006***
Sex	-5.905 (-13.765,1.954)	0.138
Body-mass Index (kg/m^2)	1.522 (0.897,2.146)	**<.001***
Smoking Status	4.823 (-9.710,19.356)	0.510
Systolic Blood Pressure (mmHg)	0.721 (0.372,1.070)	**<0.001***
Diastolic Blood Pressure (mmHg)	-0.571 (-1.047,-0.095)	**0.020***
Total Cholesterol (mg/dL)	1.089 (-0.302,2.482)	0.123
High-density lipoprotein cholesterol (mg/dL)	-0.996 (-2.333,0.341)	0.142
Low-density lipoprotein cholesterol (mg/dL)	-1.017 (-2.405,0.371)	0.148
Triglycerides (mg/dL)	-0.308 (-0.577,-0.038)	**0.026***
High-sensitivity C-Reactive Protein (mg/L)	0.155 (-0.940,1.250)	0.778
Hemoglobin A1c (mg/dL)	-14.660 (-28.318,-1.001)	**0.036***
Axial Strain: Mean Peak-to-Peak Strain		
Age, y	-0.927 (-1.475,-0.380)	**0.001***
Sex	-5.175 (-14.050,3.699)	0.249
Body-mass Index (kg/m^2)	1.859 (1.154,2.564)	**<.001***
Smoking Status	14.590 (-1.813,31.009)	0.080
Systolic Blood Pressure (mmHg)	0.683 (0.289,1.077)	**<0.001***
Diastolic Blood Pressure (mmHg)	-0.559 (-1.097,-0.022)	**0.042***
Total Cholesterol (mg/dL)	0.874 (-0.698,2.446)	0.271
High-density lipoprotein cholesterol (mg/dL)	-0.768 (-2.278,0.742)	0.313
Low-density lipoprotein cholesterol (mg/dL)	-0.772 (-2.339,0.795)	0.329
Triglycerides (mg/dL)	-0.271 (-0.576,0.033)	0.080
High-sensitivity C-Reactive Protein (mg/L)	0.057 (-1.180,1.293)	0.927
Hemoglobin A1c (mg/dL)	-10.320 (-25.744,5.103)	0.186
Axial Strain: Average L1-Norm		
Age, y	-0.225 (-0.433,-0.017)	**0.035***
Sex	-1.101 (-4.477,2.274)	0.517
Body-mass Index (kg/m^2)	0.358 (0.090,0.627)	**0.010***
Smoking Status	-1.188 (-7.431,5.054)	0.705
Systolic Blood Pressure (mmHg)	0.299 (0.149,0.449)	**<0.001***
Diastolic Blood Pressure (mmHg)	-0.287 (-0.492,-0.083)	**0.007***
Total Cholesterol (mg/dL)	0.632 (0.034,1.229)	**0.039***
High-density lipoprotein cholesterol (mg/dL)	-0.687 (-1.261,-0.113)	**0.020***
Low-density lipoprotein cholesterol (mg/dL)	-0.593 (-1.190,0.003)	0.051
Triglycerides (mg/dL)	-0.154 (-0.270,-0.038)	**0.010***
High-sensitivity C-Reactive Protein (mg/L)	-0.065 (-0.536,0.405)	0.783
Hemoglobin A1c (mg/dL)	-3.223 (-9.090,2.644)	0.277

Table 4.5. Associations of axial strain indices of the common carotid artery walls with Cardiovascular Disease Risk Factors.
* *P* values less than 0.05.

Variable	β (95% CI)	*P* Value
Lateral Strain: Mean Peak Strain		
Age, y	-0.295 (-0.468,-0.122)	**0.001***
Sex	-1.646 (-4.454,1.161)	0.246
Body-mass Index (kg/m^2)	0.559 (0.336,0.782)	**<0.001***
Smoking Status	2.818 (-2.374,8.010)	0.283
Systolic Blood Pressure (mmHg)	0.021 (-0.103,0.146)	0.732
Diastolic Blood Pressure (mmHg)	0.073 (-0.097,0.243)	0.392
Total Cholesterol (mg/dL)	-0.071 (-0.568,0.426)	0.777
High-density lipoprotein cholesterol (mg/dL)	0.224 (-0.253,0.702)	0.352
Low-density lipoprotein cholesterol (mg/dL)	0.110 (-0.381,0.611)	0.644
Triglycerides (mg/dL)	-0.010 (-0.106,0.086)	0.837
High-sensitivity C-Reactive Protein (mg/L)	0.283 (-0.108,0.674)	0.154
Hemoglobin A1c (mg/dL)	-1.986 (-6.866,2.893)	0.419
Lateral Strain: Mean Peak-to-Peak Strain		
Age, y	-0.410 (-0.651,-0.168)	**0.001***
Sex	-1.804 (-5.721,2.112)	0.361
Body-mass Index (kg/m^2)	0.729 (0.418,1.040)	**<.001***
Smoking Status	3.845 (-3.396,11.086)	0.293
Systolic Blood Pressure (mmHg)	0.068 (-0.106,0.242)	0.438
Diastolic Blood Pressure (mmHg)	0.091 (-0.146,0.328)	0.447
Total Cholesterol (mg/dL)	-0.144 (-0.837,0.550)	0.681
High-density lipoprotein cholesterol (mg/dL)	0.282 (-0.385,0.948)	0.402
Low-density lipoprotein cholesterol (mg/dL)	0.218 (-0.474,0.910)	0.532
Triglycerides (mg/dL)	-0.006 (-0.141,0.128)	0.926
High-sensitivity C-Reactive Protein (mg/L)	0.418 (-0.127,0.964)	0.131
Hemoglobin A1c (mg/dL)	-3.005 (-9.811,3.801)	0.381
Lateral Strain: Average L1-Norm		
Age, y	-0.160 (-0.251,-0.069)	**<0.001***
Sex	0.074 (-1.406,1.554)	0.921
Body-mass Index (kg/m^2)	0.195 (0.077,0.313)	**0.002***
Smoking Status	-0.029 (-2.766,2.708)	0.983
Systolic Blood Pressure (mmHg)	0.021 (-0.045,0.086)	0.534
Diastolic Blood Pressure (mmHg)	-0.004 (-0.094,0.085)	0.926
Total Cholesterol (mg/dL)	0.010 (-0.252,0.272)	0.764
High-density lipoprotein cholesterol (mg/dL)	0.025 (-0.227,0.277)	0.844
Low-density lipoprotein cholesterol (mg/dL)	0.014 (-0.248,0.275)	0.918
Triglycerides (mg/dL)	-0.008 (-0.058,0.043)	0.764
High-sensitivity C-Reactive Protein (mg/L)	-0.010 (-0.217,0.196)	0.920
Hemoglobin A1c (mg/dL)	-0.064 (-2.637,2.508)	0.960

Table 4.6. Associations of lateral strain indices of the common carotid artery walls with Cardiovascular Disease Risk Factors.

* *P* values less than 0.05.

Variable	β (95% CI)	*P* Value
Shear Strain: Mean Peak Strain		
Age, y	-0.540 (-1.029,-0.050)	**0.031***
Sex	-5.815 (-13.753,2.123)	0.148
Body-mass Index (kg/m^2)	1.364 (0.733,1.995)	**<.001***
Smoking Status	5.817 (-8.861,20.497)	0.432
Systolic Blood Pressure (mmHg)	0.468 (0.116,0.821)	**0.010***
Diastolic Blood Pressure (mmHg)	-0.193 (-0.674,0.288)	0.426
Total Cholesterol (mg/dL)	0.974 (-0.432,2.380)	0.171
High-density lipoprotein cholesterol (mg/dL)	-0.634 (-1.984,0.716)	0.352
Low-density lipoprotein cholesterol (mg/dL)	-0.919 (-2.321,0.483)	0.195
Triglycerides (mg/dL)	-0.263 (-0.536,0.009)	0.058
High-sensitivity C-Reactive Protein (mg/L)	0.154 (-0.952,1.261)	0.782
Hemoglobin A1c (mg/dL)	-13.860 (-27.654,-0.063)	**0.049***
Shear Strain: Mean Peak-to-Peak Strain		
Age, y	-0.636 (-1.219,-0.053)	**0.033***
Sex	-5.437 (-14.884,4.009)	0.255
Body-mass Index (kg/m^2)	1.612 (0.862,2.363)	**<.001***
Smoking Status	6.139 (-11.329,23.607)	0.485
Systolic Blood Pressure (mmHg)	0.572 (0.152,0.991)	**0.008***
Diastolic Blood Pressure (mmHg)	-0.130 (-0.702,0.442)	0.651
Total Cholesterol (mg/dL)	1.181 (-0.492,2.854)	0.163
High-density lipoprotein cholesterol (mg/dL)	-0.638 (-2.245,0.969)	0.431
Low-density lipoprotein cholesterol (mg/dL)	-1.059 (-2.727,0.609)	0.210
Triglycerides (mg/dL)	-0.295 (-0.619,0.029)	0.073
High-sensitivity C-Reactive Protein (mg/L)	0.676 (-0.641,1.992)	0.309
Hemoglobin A1c (mg/dL)	-22.520 (-38.943,-6.109)	**0.008***
Shear Strain: Average L1-Norm		
Age, y	-0.377 (-0.649,-0.106)	**0.007***
Sex	-0.805 (-5.207,3.598)	0.716
Body-mass Index (kg/m^2)	0.449 (0.099,0.799)	**0.013***
Smoking Status	0.305 (-7.835,8.445)	0.941
Systolic Blood Pressure (mmHg)	0.277 (0.081,0.472)	**0.006***
Diastolic Blood Pressure (mmHg)	-0.213 (-0.479,0.054)	0.116
Total Cholesterol (mg/dL)	0.522 (-0.257,1.302)	0.186
High-density lipoprotein cholesterol (mg/dL)	-0.498 (-1.247,0.251)	0.189
Low-density lipoprotein cholesterol (mg/dL)	-0.472 (-1.250,0.305)	0.229
Triglycerides (mg/dL)	-0.122 (-0.273,0.029)	0.110
High-sensitivity C-Reactive Protein (mg/L)	-0.454 (-1.068,0.159)	0.144
Hemoglobin A1c (mg/dL)	-2.707 (-10.358,4.943)	0.482

Table 4.7. Associations of shear strain indices of the common carotid artery walls with Cardiovascular Disease Risk Factors.

* *P* values less than 0.05.

Significant relationships were also noted between strain indices of the CCA and CVD risk factors. All strain measures were significantly associated with age and BMI. Increasing age was inversely related to all strain measures and BMI was positively associated with all strain measures (all p values <0.05). In addition to age and body-mass index, all axial strain parameters were statistically significant with a positive association with systolic blood pressure and an inverse association with diastolic blood pressure. Mean peak axial strain demonstrated an inverse statistically significant association with triglycerides and hemoglobin A1c. The average L1-Norm of axial strain demonstrated an additional positive relationship with total cholesterol, and inverse relationships with HDL-C and triglycerides (all p values <0.05). Lateral strain was only statistically significantly associated with age and BMI. No other CVD risk factors had statistically significant associations (all p values >0.05). Beyond the associations with age and body-mass index, shear strain metrics were positively statistically significant with systolic blood pressure. We also identified a statistically significant inverse association with hemoglobin A1c for mean peak shear strain and mean peak-to-peak strain (all p values >0.05) but this association was not observed in the average L1-Norm for shear strain.

4.4.5 Differences in Cardiovascular Disease Risk factors by sex

There were no statistically significant differences in CVD risk factors by sex for age, BMI, systolic blood pressure, diastolic blood pressure, total cholesterol, LDL-C cholesterol, triglycerides, high-sensitivity c-reactive protein, and hemoglobin A1c (all P values >0.05). HDL-C cholesterol was significantly higher in females (55.0 [19] mg/dL) compared to males (42.5 [15] mg/dL) (Z=-4.66, P=<0.001).

4.5 Discussion of Lagrangian Strain Results

Our study did not find strong statistically significant associations between carotid IMT and carotid strain indices in a small sample. This may suggest that these different assessments of arterial wall are independent metrics, despite both being correlated with many of the same CVD risk factors. This independence indicates that strain indices can serve as a complement to intima-media thickness in the carotid artery, offering an additional independent method for assessing arterial health and cardiovascular risk.

We observed positive correlations between carotid IMT and several CVD risk factors, including age, BMI, HDL-C, LDL-C, triglycerides, and hemoglobin A1c. These findings are consistent with existing literature, which suggests that arterial walls thicken with age and that higher cholesterol and hemoglobin A1c levels are associated with increased wall thickness.[11, 12] However, we encountered a conflicting correlation with total cholesterol and IMT. While we expected a positive correlation, where higher cholesterol levels would correspond with increased IMT, we instead found an inverse relationship. In our cohort wall thickness measurements increased, as total cholesterol levels decreased.

For strain, higher strain in the arterial wall is considered healthier as it is thought to represent greater arterial compliance. Our findings support this, as the correlation between age and each strain factor was negative, showing that increasing age is associated with lower strain indices. Axial and shear strain indices were positively associated with systolic blood pressure and inversely related to hemoglobin A1c. We also noted that axial strain was inversely related with diastolic blood pressure and triglycerides. However, akin to our IMT findings, the relationship between total cholesterol and axial strain was the opposite of what we expected; higher total cholesterol levels

were associated with increased strain indices. Additionally, we found conflicting relationships between BMI and all measured strain parameters.

Our study utilized a cohort of volunteer subjects with no known prior history of cardiovascular disease, who were not currently being treated for hypertension or dyslipidemia and had median age of 35 years. The unexpected relationships between total cholesterol with both IMT and strain, as well as BMI and systolic blood pressure with strain, may be related to the overall healthiness of the cohort regarding these risk factors. For instance, the total cholesterol levels in our subjects showed minimal variability, with only 2.5% of participants having high total cholesterol (>239mg/dL). Additionally, 24% of the cohort was classified as overweight and 5% as obese, a contrast to the 73.6% of U.S. adults who are overweight or obese[13]. This indicates that our cohort was generally healthier. Furthermore, while systolic blood pressure was typically elevated (mean value of 127 mmHg), 42% of participants were classified as having high blood pressure (>130mmHg Systolic).

We hypothesize that these findings may be due to early remodeling of the arterial walls, with some studies reporting initial increased compliance followed by decreased compliance. In studies observing obese pubertal children, it was hypothesized that higher level of insulin or leptin may lead to chronic vasodilatation.[14-16] This can lead to increased arterial compliance, and may continue to increase until age, genetic, and environmental factors result in the development of atherosclerotic disease and a decline in arterial compliance. [17] Given that our cohort consisted of younger adults, it is possible that we are observing this effect due to more gradual arterial remodeling. Many participants were considered to be at a healthy BMI range, with the percentage of overweight individuals in our cohort being much less than the national average. Conversely, nearly half of the individuals in our study had blood pressures > 130mmHg. We may be seeing

that the age of individuals in the study is young enough to observe an increase in compliance as BMI and systolic blood pressure increase, similar to was seen in young obese children, albeit at a much more gradual rate. The unexpected result seen in total cholesterol is more difficult to attribute to arterial remodeling and is more likely due to the similarity in values among participants. Only 2 individuals demonstrated total cholesterol levels >239 mg/dL and 25 individuals had total cholesterol levels > 200 mg/dL. Additionally, we demonstrated that the female participants in this sample had significantly higher HLD-C, which may contribute to this finding.

4.6 Conclusion

Strain and carotid IMT demonstrated different patterns of association with CVD risk factors. Strain appeared to be more strongly related to age and systolic blood pressure. This finding suggests that strain is more sensitive to early mechanical changes associated with these risk factors and has promise as a research tool to characterize arterial health.

4.7 References

[1] M. Lindstrom, N. DeCleene, H. Dorsey, V. Fuster, C. O. Johnson, K. E. LeGrand, G. A. Mensah, C. Razo, B. Stark, J. Varieur Turco, and G. A. Roth, "Global Burden of Cardiovascular Diseases and Risks Collaboration, 1990-2021," *J Am Coll Cardiol,* vol. 80, no. 25, pp. 2372-2425, Dec 20, 2022.

[2] W. Ge, C. G. Krueger, A. Weichmann, D. Shanmuganayagam, and T. Varghese, "Displacement and strain estimation for evaluation of arterial wall stiffness using a familial hypercholesterolemia swine model of atherosclerosis," *Med Phys,* vol. 39, no. 7, pp. 4483-92, Jul, 2012.

[3] R. A. Mukaddim, Y. Liu, M. Graham, J. C. Eickhoff, A. M. Weichmann, M. C. Tattersall, C. E. Korcarz, J. H. Stein, T. Varghese, K. W. Eliceiri, and C. Mitchell, "In Vivo Adaptive Bayesian Regularized Lagrangian Carotid Strain Imaging for Murine Carotid Arteries and Its Associations With Histological Findings," *Ultrasound Med Biol,* vol. 49, no. 9, pp. 2103-2112, Sep, 2023.

[4] H. Shi, C. C. Mitchell, M. McCormick, M. A. Kliewer, R. J. Dempsey, and T. Varghese, "Preliminary in vivo atherosclerotic carotid plaque characterization using the accumulated axial strain and relative lateral shift strain indices," *Phys Med Biol,* vol. 53, no. 22, pp. 6377-94, Nov 21, 2008.

[5] M. McCormick, T. Varghese, X. Wang, C. Mitchell, M. A. Kliewer, and R. J. Dempsey, "Methods for robust in vivo strain estimation in the carotid artery," *Phys Med Biol,* vol. 57, no. 22, pp. 7329-53, Nov 21, 2012.

[6] N. H. Meshram, and T. Varghese, "GPU Accelerated Multilevel Lagrangian Carotid Strain Imaging," *IEEE Trans Ultrason Ferroelectr Freq Control,* vol. 65, no. 8, pp. 1370-1379, Aug, 2018.

[7] M. J. Daniels, and T. Varghese, "Dynamic frame selection for in vivo ultrasound temperature estimation during radiofrequency ablation," *Phys Med Biol,* vol. 55, no. 16, pp. 4735-53, Aug 21, 2010.

[8] C. C. Mitchell, J. H. Stein, T. D. Cook, S. Salamat, X. Wang, T. Varghese, D. C. Jackson, C. Sandoval Garcia, S. M. Wilbrand, and R. J. Dempsey, "Histopathologic Validation of Grayscale Carotid Plaque Characteristics Related to Plaque Vulnerability," *Ultrasound Med Biol,* vol. 43, no. 1, pp. 129-137, Jan, 2017.

[9] M. C. Tattersall, A. Gassett, C. E. Korcarz, A. D. Gepner, J. D. Kaufman, K. J. Liu, B. C. Astor, L. Sheppard, R. A. Kronmal, and J. H. Stein, "Predictors of carotid thickness and plaque progression during a decade: the Multi-Ethnic Study of Atherosclerosis," *Stroke,* vol. 45, no. 11, pp. 3257-62, Nov, 2014.

[10] C. C. Mitchell, C. E. Korcarz, A. D. Gepner, R. Nye, R. L. Young, M. Matsuzaki, W. S. Post, J. D. Kaufman, R. L. McClelland, and J. H. Stein, "Carotid Artery Echolucency, Texture Features, and Incident Cardiovascular Disease Events: The MESA Study," *J Am Heart Assoc,* vol. 8, no. 3, pp. e010875, Feb 5, 2019.

[11] X. Xu, B. Wang, C. Ren, J. Hu, D. A. Greenberg, T. Chen, L. Xie, and K. Jin, "Age-related Impairment of Vascular Structure and Functions," *Aging Dis,* vol. 8, no. 5, pp. 590-610, Oct, 2017.

[12] M. Zhou, J. Zhang, J. Jia, Y. Liu, M. Guo, X. Lv, X. Zhao, and S. Chen, "Association between hemoglobin A," *Nutr Metab Cardiovasc Dis,* vol. 32, no. 6, pp. 1463-1469, Jun, 2022.

[13] F. CD, C. MD, and A. J, "Prevalence of overweight, obesity, and severe obesity among adults

aged 20 and over: United States, 1960–1962 through 2017–2018," 2020.

[14] L. J. Chalmers, K. C. Copeland, C. N. Hester, D. A. Fields, and A. W. Gardner, "Paradoxical increase in arterial compliance in obese pubertal children," *Angiology,* vol. 62, no. 7, pp. 565-70, Oct, 2011.

[15] J. B. Tryggestad, and K. R. Short, "Arterial compliance in obese children: implications for cardiovascular health," *Exerc Sport Sci Rev,* vol. 42, no. 4, pp. 175-82, Oct, 2014.

[16] F. Dangardt, W. Osika, R. Volkmann, L. M. Gan, and P. Friberg, “Obese children show increased intimal wall thickness and decreased pulse wave velocity,” *Clin Physiol Funct Imaging,* vol. 28, no. 5, pp. 287-93, Sep, 2008.

[17] A. W. Gardner, and D. E. Parker, “Association between arterial compliance and age in participants 9 to 77 years old,” *Angiology,* vol. 61, no. 1, pp. 37-41, 2010.

Chapter 5: Using Lagrangian Strain Estimation for Assessing Arterial Stiffness in Carotid Atherosclerosis

5.1 Background

Cardiovascular disease (CVD) is the leading cause of death worldwide [1] and is associated with many risk factors that may be modified through lifestyle changes. Thus, there is a need to identify early biological changes to the arterial wall which may indicate an individual is at increased risk for CVD. Early arterial injury is thought to manifest with a change in arterial wall structure and mechanical properties that may be seen prior to the appearance of atherosclerotic plaque. Carotid intima media thickness (IMT) has been used to evaluate risk for CVD[2, 3] and is hypothesized to represent a change in arterial wall structure due to fibromuscular hyperplasia and smooth muscle hypertrophy associated with aging and hypertension.[4] However, carotid IMT does not directly measure mechanical properties of the arterial wall which also may be occurring in response to hemodynamic stress or arterial injury.

5.1.1 Lagrangian Strain as Surrogate for Vessel Compliance

Ultrasound elastography is a valuable tool for evaluating tissue deformation and has been widely used to assess carotid plaque stability [5-8] and vessel wall mechanics [9-11]. Plaques exhibiting greater strain tend to be softer and more echolucent, making them more susceptible to rupture [8, 12-14]. Studies using intravascular ultrasound (IVUS) elastography in coronary arteries highlight the role of plaque composition in determining stability, with fatty plaques showing increased strain compared to fibrous or calcified ones [15, 16]. Arterial regions without plaques but with lower strain values often indicate stiffer vessel walls, which may be associated with inflammation and a predisposition to future plaque formation [17]. Our group has been developing a Lagrangian strain

technique to evaluate the mechanical properties of the arterial wall.[18, 19] This technique quantifies the deformation of the arterial wall during the cardiac cycle and provides insight into arterial compliance, a measure of how easily the artery can expand and contract in response to blood pressure changes. We have previously demonstrated the ability of Lagrangian strain imaging to quantify carotid plaque vulnerability.[7, 12, 20-26]

This study aims to explore the relationships between mechanical properties of the arterial wall as measured using Lagrangian arterial strain in a larger cohort of healthy adults, with a particular focus on understanding how these measures are associated with traditional cardiovascular risk factors. By examining both structural (IMT) and mechanical (strain indices) markers of vascular health, this project will provide insight into how novel measures of strain can be used as a research tool to identify early changes associated with arterial injury.

5.2 Materials and Methods

5.2.1 Volunteer Cohort

The study cohort consisted of 181 healthy individuals (75 males and 106 females) aged between 18 and 88 years, recruited from the University of Wisconsin-Madison between December 2021 and January 2025. The only requirement for the study was that volunteers were not actively treated for hypertension or hyperlipidemia. Volunteers participated in the study after providing informed consent using a protocol approved by the University of Wisconsin-Madison institutional review board. Collected data included age (years), sex, body-mass index (kg/m^2), blood pressure (mmHg), fasting (10-12hrs) lipid panel (total cholesterol ,high-density lipoprotein cholesterol [HDL-C], low-density lipoprotein cholesterol [LDL-C] , and triglycerides measured in mg/dL), high-sensitivity C-Reactive Protein (mg/L), and hemoglobin A1c (mg/dL). Blood work and health

history were collected to assess cardiovascular risk factors. The 80 individuals selected for CIMT measurement seen in the previous chapter were include in this dataset.

5.2.2 Lagrangian Strain Estimation

In this study, we will employ Lagrangian strain estimation initially proposed by Shi et al. (2008) [27] and outlined in McCormick et al. (2012), [24] and later adapted for GPU acceleration by Meshram et al. (2018)[21]. The strain estimation algorithm utilizes radiofrequency (RF) data collected using an Acuson S2000 system with an 18L6 transducer (Siemens Medical Solutions, Malvern, PA, USA) to calculate strain distribution and quantitative strain indices within defined regions. This process relies on binary segmentations of the arterial wall performed on RF-derived B-mode images and employs a three-level pyramidal hierarchy for displacement tracking, resulting in the calculation of the Lagrangian strain tensor from the accumulated displacements. The GPU implementation is executed using an NVIDIA K40 GPU with CUDA programming, as described by Meshram et al. (2018)[21]. In this study, all binary segmentations of the carotid walls were performed by a trained sonographer. Scalar strain indices are obtained from the Lagrangian strain tensor via Eigen analysis. For each strain type, the mean peak strain index is used to represent the strain for each participant.

5.2.3 Statistical Analysis

Multiple regression analysis was used to examine relationships between axial, lateral and shear strain indices and cardiovascular risk factors. The model included the cardiovascular risk factors of age, sex, body mass index, systolic blood pressure, diastolic blood pressure, total cholesterol, high-density lipoprotein cholesterol, low-density lipoprotein cholesterol, triglycerides, high-sensitivity C-reactive protein, and hemoglobin A1c compared individually with axial, lateral and shear strain indices. Mann-Whitney U tests were used to examine differences by sex in CVD risk

factors (age, BMI, systolic blood pressure, diastolic blood pressure, total cholesterol, HDL-C, LDL-C, triglycerides, high-sensitivity C-reactive protein, and hemoglobin A1c).

5.3 Results

5.3.1 Baseline Participant Characteristics

Participants were median (IQR) age 42 (29) years, 58.6% female, 1 (1%) were American Indian, 4(5%) were Hispanic, 9(11%) were Asian/Asian American, 1(1%) were mixed race and 64 (80%) were white. All baseline participant characteristics are presented in (Table 5.1).

	N	Median (inter-quartile range)	Range
Age, y	181	42 (29)	18-88
Sex (n, %)	181		
Male		75 (41.4%)	
Female		106 (58.6%)	
Body-mass Index (kg/m^2)	181	24.9 (5.6)	17.5-51
Systolic Blood Pressure (mmHg)	181	128 (22)	98-188
Diastolic Blood Pressure (mmHg)	181	79 (18)	61-102
Total Cholesterol (mg/dL)	181	193 (46)	114-316
High-density lipoprotein cholesterol (mg/dL)	181	53 (22)	25-109
Low-density lipoprotein cholesterol (mg/dL)	181	115 (40)	59-223
Triglycerides (mg/dL)	181	82 (44)	26-527
High-sensitivity C-Reactive Protein (mg/L)	181	1.2 (2.5)	0.299-17.9
Hemoglobin A1c (mg/dL)	181	5.4 (0.4)	4.6-6.2
Lateral Strain peak strain value	181	8.9 (6.9)	2.9-36.2
Shear Strain peak strain value	181	24.0 (19.1)	7.5-92.7
Axial Strain peak strain value	181	24.9 (23.3)	5.0-101.7

Table 5.1. Participant Characteristics. Participant characteristics of volunteer dataset.

5.3.2 Relationships between Carotid Strain indices and CVD Risk Factors

Significant relationships were also noted between strain indices of the CCA and CVD risk factors (Table 5.2). All strain measures were significantly associated with age and BMI. Increasing age was inversely related to all strain measures and BMI was positively associated with all strain measures (all p values <0.05). In addition to age and body-mass index, mean peak axial strain was found to be statistically significant with a positive association with systolic blood pressure and an

inverse association with diastolic blood pressure. Mean peak axial strain demonstrated an inverse statistically significant association with triglycerides and hemoglobin A1c. The mean peak axial strain relationships seen are the same as what is seen in the CVD relationships with Mean peak absolute principal strain. Mean peak lateral strain was only statistically significantly associated with age and BMI. No other CVD risk factors had statistically significant associations (all p values >0.05). Beyond the associations with age and body-mass index, mean peak shear strain was positively statistically significant with systolic blood pressure. We also identified a statistically significant inverse association with hemoglobin A1c for mean peak shear strain (p value <0.05).

5.3.4 Differences in Cardiovascular Disease Risk factors by sex

There were no statistically significant differences in CVD risk factors by sex for age, BMI, systolic blood pressure, diastolic blood pressure, total cholesterol, LDL-C cholesterol, triglycerides, high-sensitivity c-reactive protein, and hemoglobin A1c (all P values >0.05). HDL-C cholesterol was significantly higher in females (62.5 [20] mg/dL) compared to males (45.4 [14] mg/dL) (Z=-7.4, P=<0.001).

Variable	β (95% CI)	*P* Value
Axial Strain: Mean Peak Strain		
Age, y	-0.467(-0.630,-0.304)	**<0.001***
Sex	0.371 (-5.348,6.090)	0.898
Body-mass Index (kg/m^2)	1.068 (0.581,1.554)	**<0.001***
Systolic Blood Pressure (mmHg)	0.264 (0.071,0.457)	**0.007***
Diastolic Blood Pressure (mmHg)	0.032 (-0.119,0.181)	0.471
Total Cholesterol (mg/dL)	-0.096 (-0.243,0.055)	0.198
High-density lipoprotein cholesterol (mg/dL)	-0.056 (-0.205,0.095)	0.452
Low-density lipoprotein cholesterol (mg/dL)	-0.056 (-0.205,0.096)	0.455
Triglycerides (mg/dL)	-0.051 (-0.199,0.100)	0.498
High-sensitivity C-Reactive Protein (mg/L)	0.111 (-0.154,0.376)	0.408
Hemoglobin A1c (mg/dL)	-18.020(-26.433,-9.606)	**<0.001***
Lateral Strain: Mean Peak Strain		
Age, y	-0.336 (-0.463,-0.196)	**<0.001***
Sex	-0.981 (-0.899,2.862)	0.305
Body-mass Index (kg/m^2)	0.260 (0.115,0.395)	**<0.001***
Systolic Blood Pressure (mmHg)	0.199 (0.115,0.339)	**0.007***
Diastolic Blood Pressure (mmHg)	0.063 (-0.088,0.211)	0.399
Total Cholesterol (mg/dL)	-0.050 (-0.198,0.101)	0.507
High-density lipoprotein cholesterol (mg/dL)	0.013 (-0.137,0.163)	0.862
Low-density lipoprotein cholesterol (mg/dL)	-0.064 (-0.213,0.088)	0.395
Triglycerides (mg/dL)	0.023 (-0.127,0.173)	0.754
High-sensitivity C-Reactive Protein (mg/L)	0.019 (-0.068,0.107)	0.663
Hemoglobin A1c (mg/dL)	-4.749(-7.573,-1.925)	**<0.001***
Shear Strain: Mean Peak Strain		
Age, y	-0.398 (-0.517,-0.263)	**<0.001***
Sex	-0.636 (-5.345,4.072)	0.790
Body-mass Index (kg/m^2)	0.274 (0.129,0.407)	**<0.001***
Systolic Blood Pressure (mmHg)	0.228 (0.081,0.366)	**0.002***
Diastolic Blood Pressure (mmHg)	0.108 (-0.042,0.254)	0.146
Total Cholesterol (mg/dL)	-0.089 (-0.235,0.062)	0.236
High-density lipoprotein cholesterol (mg/dL)	-0.037 (-0.186,0.113)	0.617
Low-density lipoprotein cholesterol (mg/dL)	-0.067 (-0.216,0.085)	0.374
Triglycerides (mg/dL)	-0.042 (-0.191,0.108)	0.571
High-sensitivity C-Reactive Protein (mg/L)	0.032 (-0.187,0.251)	0.773
Hemoglobin A1c (mg/dL)	-15.434 (-22.334,-8.535)	**<0.001***

Table 5.2. Associations of strain indices of the common carotid artery walls with Cardiovascular Disease Risk Factors. * *P* values less than 0.05.

5.4 Discussion

For strain, higher strain in the arterial wall is considered healthier as it is thought to represent greater arterial compliance. Arterial walls strain is known to decrease with age as well as history of increased CVD risk factors such as obesity[28], hypercholesterolemia[29], and hyperglycemia[30, 31]. Overall our findings support this, as the correlation between age and each strain factor was negative, showing that increasing age is associated with lower strain indices. All peak strain values were also positively associated with systolic blood pressure and inversely related to hemoglobin A1c.

In a previous study (Chapter 4), we found that the relationship between total cholesterol and our carotid intima-media thickness (CIMT) measurements as well as our strain values was the opposite of what we expected; higher total cholesterol levels were associated with increased strain indices. In the expanded dataset used in this study, we observed that the association with cholesterol was no longer significant, though its correlation direction is now what we expect. However, the conflicting relationships between BMI and all measured strain parameters is also present in this dataset.

Our expanded study utilized a cohort of 181 volunteer subjects with no known prior history of cardiovascular disease and who were not currently being treated for hypertension or dyslipidemia had a median age of 42. This includes the 80 subjects with median age of 35 years used in the prior study. In the previous cohort, the unexpected relationships between total cholesterol and BMI with both IMT and strain, were attributed to the overall healthiness of the cohort regarding these risk factors.

For this cohort, the total cholesterol levels in our subjects were low, with only 9% (up from 2.5%) of participants having high total cholesterol (>239mg/dL). Similarly, 25% of the cohort was

classified as overweight and 24% as obese. When compared to the previous dataset of 80 participants, this is a sizeable increase as the number of overweight or obese individuals is up from 29% to 49%. However, this dataset has a lower percentage of individuals considered to be overweight or obese compared to the reported U.S. average of 73.6% of adults being considered overweight or obese. [32]

We previously hypothesized that our findings could be due to early remodeling of the arterial walls, with some studies reporting initial increased compliance followed by decreased compliance. In studies observing obese pubertal children, it was hypothesized that higher level of insulin or leptin may lead to chronic vasodilatation [33-35].

A large portion of participants in our cohort fell within a healthy BMI range, with the prevalence of overweight individuals notably lower than the national average. In contrast, nearly half of the cohort had systolic blood pressures exceeding 130 mmHg. This pattern may reflect the relatively young age of the study population, where increasing BMI and systolic blood pressure are still associated with greater vascular compliance—similar to trends observed in obese children, though likely occurring at a slower, more gradual rate.

A potential explanation for the unexpected findings related to cholesterol and BMI could lie in the complex interplay between metabolic health and vascular compliance. It is possible that the increase in BMI within a relatively healthy cohort reflects a phase of vascular adaptation where compliance is still maintained or even enhanced.[34] The lack of significant cholesterol associations in the expanded cohort may also indicate that the impact of cholesterol on vascular properties is moderated by other factors such as fitness levels or inflammation markers [36], which were not directly measured in this study. Further research is needed to assess how other potential confounders might influence the relationship between strain and cardiovascular risk factors.

One possible reason for the unexpected positive association between BMI and vascular strain could be related to the composition and distribution of body fat. Emerging evidence suggests that visceral adiposity, as opposed to subcutaneous fat, may be more closely linked with vascular stiffness and adverse cardiovascular outcomes. If a significant proportion of our cohort had higher BMI driven primarily by increased subcutaneous fat rather than visceral fat, this may explain why increased BMI appeared to correlate with greater strain. [37, 38] Additionally, the relatively young and healthy nature of our cohort may mean that the detrimental vascular effects of increased BMI have not yet manifested, leading to preserved or even enhanced vascular compliance in this population.

Moreover, our findings suggest that vascular remodeling in the context of metabolic alterations may follow a non-linear trajectory. While some literature supports the idea of early adaptive compliance[34], others indicate that prolonged metabolic stress ultimately results in stiffening and reduced strain.[28] Longitudinal studies would be beneficial to capture this transition and better understand the temporal dynamics of vascular adaptation in response to metabolic risk factors.

5.5 References

[1] M. Lindstrom, N. DeCleene, H. Dorsey, V. Fuster, C. O. Johnson, K. E. LeGrand, G. A. Mensah, C. Razo, B. Stark, J. Varieur Turco, and G. A. Roth, "Global Burden of Cardiovascular Diseases and Risks Collaboration, 1990-2021," *J Am Coll Cardiol,* vol. 80, no. 25, pp. 2372-2425, Dec 20, 2022.

[2] M. C. Tattersall, A. Gassett, C. E. Korcarz, A. D. Gepner, J. D. Kaufman, K. J. Liu, B. C. Astor, L. Sheppard, R. A. Kronmal, and J. H. Stein, "Predictors of carotid thickness and plaque progression during a decade: the Multi-Ethnic Study of Atherosclerosis," *Stroke,* vol. 45, no. 11, pp. 3257-62, Nov, 2014.

[3] J. Andersson, J. Sundström, T. Gustavsson, J. Hulthe, A. Elmgren, K. Zilmer, M. Zilmer, and L. Lind, "Echogenecity of the carotid intima-media complex is related to cardiovascular risk factors, dyslipidemia, oxidative stress and inflammation: the Prospective Investigation of the Vasculature in Uppsala Seniors (PIVUS) study," *Atherosclerosis,* vol. 204, no. 2, pp. 612-8, Jun, 2009.

[4] P. Greenland, J. Abrams, G. P. Aurigemma, M. G. Bond, L. T. Clark, M. H. Criqui, J. R. Crouse, L. Friedman, V. Fuster, D. M. Herrington, L. H. Kuller, P. M. Ridker, W. C.

Roberts, W. Stanford, N. Stone, H. J. Swan, K. A. Taubert, and L. Wexler, "Prevention Conference V: Beyond secondary prevention: identifying the high-risk patient for primary prevention: noninvasive tests of atherosclerotic burden: Writing Group III," *Circulation,* vol. 101, no. 1, pp. E16-22, Jan 04, 2000.

[5] C. L. de Korte, S. Fekkes, A. J. Nederveen, R. Manniesing, and H. R. Hansen, "Review: Mechanical Characterization of Carotid Arteries and Atherosclerotic Plaques," *IEEE Trans Ultrason Ferroelectr Freq Control,* vol. 63, no. 10, pp. 1613-1623, 10, 2016.

[6] G. Geroulakos, G. Ramaswami, A. Nicolaides, K. James, N. Labropoulos, G. Belcaro, and M. Holloway, "Characterization of symptomatic and asymptomatic carotid plaques using high-resolution real-time ultrasonography," *Br J Surg,* vol. 80, no. 10, pp. 1274-7, Oct, 1993.

[7] N. H. Meshram, T. Varghese, C. C. Mitchell, D. C. Jackson, S. M. Wilbrand, B. P. Hermann, and R. J. Dempsey, "Quantification of carotid artery plaque stability with multiple region of interest based ultrasound strain indices and relationship with cognition," *Phys Med Biol,* vol. 62, no. 15, pp. 6341-6360, Jul 17, 2017.

[8] X. Wang, D. C. Jackson, C. C. Mitchell, T. Varghese, S. M. Wilbrand, B. G. Rocque, B. P. Hermann, and R. J. Dempsey, "Classification of Symptomatic and Asymptomatic Patients with and without Cognitive Decline Using Non-invasive Carotid Plaque Strain Indices as Biomarkers," *Ultrasound Med Biol,* vol. 42, no. 4, pp. 909-18, Apr, 2016.

[9] C. L. de Korte, A. F. van der Steen, E. I. Céspedes, and G. Pasterkamp, "Intravascular ultrasound elastography in human arteries: initial experience in vitro," *Ultrasound Med Biol,* vol. 24, no. 3, pp. 401-8, Mar, 1998.

[10] G. Zahnd, L. Boussel, A. Marion, M. Durand, P. Moulin, A. Sérusclat, and D. Vray, "Measurement of two-dimensional movement parameters of the carotid artery wall for early detection of arteriosclerosis: a preliminary clinical study," *Ultrasound Med Biol,* vol. 37, no. 9, pp. 1421-9, Sep, 2011.

[11] S. Golemati, A. Sassano, M. J. Lever, A. A. Bharath, S. Dhanjil, and A. N. Nicolaides, "Carotid artery wall motion estimated from B-mode ultrasound using region tracking and block matching," *Ultrasound Med Biol,* vol. 29, no. 3, pp. 387-99, Mar, 2003.

[12] N. H. Meshram, D. Jackson, T. Varghese, C. C. Mitchell, S. M. Wilbrand, R. J. Dempsey, and B. P. Hermann, "A Cross-Sectional Investigation of Cognition and Ultrasound-Based Vascular Strain Indices," *Arch Clin Neuropsychol,* vol. 35, no. 1, pp. 46-55, Jan 24, 2019.

[13] M. H. Roy Cardinal, M. H. G. Heusinkveld, Z. Qin, R. G. P. Lopata, C. Naim, G. Soulez, and G. Cloutier, "Carotid Artery Plaque Vulnerability Assessment Using Noninvasive Ultrasound Elastography: Validation With MRI," *AJR Am J Roentgenol,* vol. 209, no. 1, pp. 142-151, Jul, 2017.

[14] A. A. Khan, S. Sikdar, T. Hatsukami, J. Cebral, M. Jones, J. Huston, G. Howard, and B. K. Lal, "Noninvasive characterization of carotid plaque strain," *J Vasc Surg,* vol. 65, no. 6, pp. 1653-1663, Jun, 2017.

[15] C. L. de Korte, J. A. Schaar, F. Mastik, P. W. Serruys, and A. F. van der Steen, "Intravascular elastography: from bench to bedside," *J Interv Cardiol,* vol. 16, no. 3, pp. 253-9, Jun, 2003.

[16] R. A. Baldewsing, J. A. Schaar, C. L. de Korte, F. Mastik, P. W. Serruys, and A. F. van der Steen, "Intravascular Ultrasound Elastography: A Clinician's Tool for Assessing Vulnerability and Material Composition of Plaques," *Stud Health Technol Inform,* vol. 113, pp. 75-96, 2005.

[17] J. C. Kohn, M. C. Lampi, and C. A. Reinhart-King, "Age-related vascular stiffening: causes and consequences," *Front Genet,* vol. 6, pp. 112, 2015.

[18] W. Ge, C. G. Krueger, A. Weichmann, D. Shanmuganayagam, and T. Varghese, "Displacement and strain estimation for evaluation of arterial wall stiffness using a familial hypercholesterolemia swine model of atherosclerosis," *Med Phys,* vol. 39, no. 7, pp. 4483-92, Jul, 2012.

[19] R. A. Mukaddim, Y. Liu, M. Graham, J. C. Eickhoff, A. M. Weichmann, M. C. Tattersall, C. E. Korcarz, J. H. Stein, T. Varghese, K. W. Eliceiri, and C. Mitchell, "In Vivo Adaptive Bayesian Regularized Lagrangian Carotid Strain Imaging for Murine Carotid Arteries and Its Associations With Histological Findings," *Ultrasound Med Biol,* vol. 49, no. 9, pp. 2103-2112, Sep, 2023.

[20] R. J. Dempsey, T. Varghese, D. C. Jackson, X. Wang, N. H. Meshram, C. C. Mitchell, B. P. Hermann, S. C. Johnson, S. E. Berman, and S. M. Wilbrand, "Carotid atherosclerotic plaque instability and cognition determined by ultrasound-measured plaque strain in asymptomatic patients with significant stenosis," *J Neurosurg,* vol. 128, no. 1, pp. 111-119, Jan, 2018.

[21] N. H. Meshram, and T. Varghese, "GPU Accelerated Multilevel Lagrangian Carotid Strain Imaging," *IEEE Trans Ultrason Ferroelectr Freq Control,* vol. 65, no. 8, pp. 1370-1379, Aug, 2018.

[22] N. H. Meshram, C. C. Mitchell, S. M. Wilbrand, R. J. Dempsey, and T. Varghese, "In vivo carotid strain imaging using principal strains in longitudinal view," *Biomed Phys Eng Express,* vol. 5, no. 3, 2019.

[23] M. McCormick, N. Rubert, and T. Varghese, "Bayesian regularization applied to ultrasound strain imaging," *IEEE Trans Biomed Eng,* vol. 58, no. 6, pp. 1612-20, Jun, 2011.

[24] M. McCormick, T. Varghese, X. Wang, C. Mitchell, M. A. Kliewer, and R. J. Dempsey, "Methods for robust in vivo strain estimation in the carotid artery," *Phys Med Biol,* vol. 57, no. 22, pp. 7329-53, Nov 21, 2012.

[25] X. Wang, C. C. Mitchell, T. Varghese, D. C. Jackson, B. G. Rocque, B. P. Hermann, and R. J. Dempsey, "Improved Correlation of Strain Indices with Cognitive Dysfunction with Inclusion of Adventitial Layer with Carotid Plaque," *Ultrason Imaging,* vol. 38, no. 3, pp. 194-208, May, 2016.

[26] S. E. Berman, X. Wang, C. C. Mitchell, B. Kundu, D. C. Jackson, S. M. Wilbrand, T. Varghese, B. P. Hermann, H. A. Rowley, S. C. Johnson, and R. J. Dempsey, "The relationship between carotid artery plaque stability and white matter ischemic injury," *Neuroimage Clin,* vol. 9, pp. 216-22, 2015.

[27] H. Shi, C. C. Mitchell, M. McCormick, M. A. Kliewer, R. J. Dempsey, and T. Varghese, "Preliminary in vivo atherosclerotic carotid plaque characterization using the accumulated axial strain and relative lateral shift strain indices," *Phys Med Biol,* vol. 53, no. 22, pp. 6377-94, Nov 21, 2008.

[28] P. Tounian, Y. Aggoun, B. Dubern, V. Varille, B. Guy-Grand, D. Sidi, J. P. Girardet, and D. Bonnet, "Presence of increased stiffness of the common carotid artery and endothelial dysfunction in severely obese children: a prospective study," *Lancet,* vol. 358, no. 9291, pp. 1400-4, Oct 27, 2001.

[29] Y. Aggoun, D. Bonnet, D. Sidi, J. P. Girardet, E. Brucker, M. Polak, M. E. Safar, and B. I. Levy, "Arterial mechanical changes in children with familial hypercholesterolemia," *Arterioscler Thromb Vasc Biol,* vol. 20, no. 9, pp. 2070-5, Sep, 2000.

[30] Y. Li, Y. Liu, S. Liu, M. Gao, W. Wang, K. Chen, and L. Huang, "Diabetic vascular diseases: molecular mechanisms and therapeutic strategies," *Signal Transduct Target Ther,* vol. 8, no. 1, pp. 152, Apr 10, 2023.

[31] Z. Z. Zhang, P. Wang, X. L. Kong, W. L. Mao, and M. Y. Cui, "Association of hemoglobin with arterial stiffness evaluated by carotid-femoral pulse wave velocity among Chinese adults," *Chronic Dis Transl Med,* vol. 5, no. 2, pp. 122-128, Jun, 2019.

[32] C. D. Fryar, M. D. Carroll, and J. Afful, "Prevalence of overweight, obesity, and severe obesity among adults aged 20 and over: United States, 1960-1962 through 2017–2018," 2020.

[33] L. J. Chalmers, K. C. Copeland, C. N. Hester, D. A. Fields, and A. W. Gardner, "Paradoxical increase in arterial compliance in obese pubertal children," *Angiology,* vol. 62, no. 7, pp. 565-70, Oct, 2011.

[34] J. B. Tryggestad, and K. R. Short, "Arterial compliance in obese children: implications for cardiovascular health," *Exerc Sport Sci Rev,* vol. 42, no. 4, pp. 175-82, Oct, 2014.

[35] F. Dangardt, W. Osika, R. Volkmann, L. M. Gan, and P. Friberg, "Obese children show increased intimal wall thickness and decreased pulse wave velocity," *Clin Physiol Funct Imaging,* vol. 28, no. 5, pp. 287-93, Sep, 2008.

[36] P. M. Ridker, M. V. Moorthy, N. R. Cook, N. Rifai, I. M. Lee, and J. E. Buring, "Inflammation, Cholesterol, Lipoprotein(a), and 30-Year Cardiovascular Outcomes in Women," *N Engl J Med,* vol. 391, no. 22, pp. 2087-2097, Dec 05, 2024.

[37] J. Mao, S. Gan, S. Gong, Q. Zhou, F. Yu, H. Zhou, H. Lu, Q. Li, and Z. Deng, "Visceral fat area is more strongly associated with arterial stiffness than abdominal subcutaneous fat area in Chinese patients with type 2 diabetes," *Diabetol Metab Syndr,* vol. 16, no. 1, pp. 123, Jun 05, 2024.

[38] K. Sutton-Tyrrell, A. Newman, E. M. Simonsick, R. Havlik, M. Pahor, E. Lakatta, H. Spurgeon, and P. Vaitkevicius, "Aortic stiffness is associated with visceral adiposity in older adults enrolled in the study of health, aging, and body composition," *Hypertension,* vol. 38, no. 3, pp. 429-33, Sep, 2001.

Chapter 6: Relationship between Atherosclerosis and Lagrangian Strain Indices

6.1 Background

Atherosclerosis is a major risk factor for cardiovascular diseases (CVD), contributing significantly to arterial remodeling and increased arterial stiffness. Chronic atherosclerosis leads to structural and functional changes in the vascular system, including endothelial dysfunction, increased vascular resistance, and arterial wall thickening.[1] These alterations can be quantified using Lagrangian strain imaging, a noninvasive technique that evaluates changes in arterial wall mechanics. This chapter explores the relationship between atherosclerosis and Lagrangian strain indices, particularly in the context of carotid artery stiffness and its implications for disease progression.

6.1.1 Atherosclerosis Vessel Pathophysiology

Atherosclerosis develops through a complex interplay of lipid accumulation, inflammation, endothelial dysfunction, and smooth muscle cell proliferation.[2] Endothelial injury, often caused by high blood pressure, smoking, or elevated cholesterol, increases permeability to low-density lipoproteins (LDL), which infiltrate the arterial walls. Oxidized LDL particles trigger an inflammatory response, attracting immune cells such as monocytes and T lymphocytes. Monocytes differentiate into macrophages, which engulf oxidized LDL but eventually become foam cells, forming fatty streaks within the artery walls.[3]

As the lesion progresses, smooth muscle cells migrate from the medial layer to the intima, where they proliferate and secrete extracellular matrix components such as collagen and elastin, leading to fibrous cap formation.[4, 5] Over time, inflammation weakens the fibrous cap, increasing the

risk of rupture. If the cap ruptures, plaque contents—including lipids, collagen, and tissue factor—are exposed to the bloodstream, triggering the coagulation cascade and thrombus formation.[6, 7] This process can lead to ischemic events such as heart attacks or strokes.

Chronic inflammation and oxidative stress further drive atherosclerosis progression. [8, 9] Inflammatory mediators, including cytokines and chemokines, promote immune cell recruitment and foam cell formation, while oxidative stress exacerbates endothelial dysfunction.[8, 9] Mechanical forces such as turbulent blood flow also influence plaque development.[10, 11] Regions exposed to disturbed flow are more prone to endothelial injury and plaque formation, whereas laminar flow in healthy arteries preserves endothelial integrity and prevents lipid accumulation.[12]

The development of atherosclerosis not only alters the structural integrity of the arterial wall but also significantly impacts its mechanical properties, including arterial strain.[13] As plaque builds up and the arterial wall undergoes remodeling due to smooth muscle cell proliferation and extracellular matrix deposition, the vessel becomes stiffer and less compliant. This reduction in elasticity translates into lower axial and shear strain values, as the artery's ability to stretch and deform during the cardiac cycle diminishes. Studies have shown that atherosclerotic arteries bear more stress and exhibit less strain compared to healthy ones, highlighting the mechanical implications of plaque development.[14] Furthermore, chronic inflammation and oxidative stress associated with atherosclerosis promote vascular remodeling and fibrosis, exacerbating arterial stiffness. Consequently, individuals with advanced atherosclerosis often exhibit reduced carotid arterial strain, a marker of vascular dysfunction that may contribute to the heightened cardiovascular risk observed in this population.[15]

Hemoglobin A1c (HbA1c) is a well-established marker for long-term glycemic control, reflecting average blood glucose levels over a period of approximately three months. Elevated HbA1c levels have been associated with increased cardiovascular risk, even among individuals without diagnosed diabetes. Research indicates that higher HbA1c levels correlate with greater arterial stiffness, a key factor in the development of atherosclerosis. For instance, a study found that each 1% increase in HbA1c was associated with a 1.43-fold increase in the odds of elevated arterial stiffness, independent of other risk factors. [16]

The mechanisms linking elevated HbA1c to arterial stiffness involve several pathophysiological processes. Chronic hyperglycemia leads to the formation of advanced glycation end products (AGEs), which can cross-link with collagen and elastin in the arterial wall, reducing elasticity and promoting stiffness.[17] Additionally, elevated HbA1c levels are associated with endothelial dysfunction, inflammation, and oxidative stress, all of which contribute to vascular remodeling and decreased arterial compliance.[18]

Moreover, elevated HbA1c levels have been linked to the presence and severity of atherosclerotic plaques. A study demonstrated that higher HbA1c levels were independently associated with the presence of significant coronary artery plaques, even in non-diabetic individuals.[19]

Lagrangian strain imaging provides a quantitative approach to assess these biomechanical changes. Atherosclerosis-induced arterial stiffening results from increased collagen deposition, reduced elastin content, and vascular smooth muscle hypertrophy. By measuring axial, lateral, and shear strain indices, this imaging technique helps detect early arterial stiffening before significant clinical symptoms emerge.

6.2 Materials and Methods

6.2.1 Lagrangian Strain Estimation

Lagrangian strain estimation has been extensively used in prior literature for assessing carotid plaque instability and cognition in both asymptomatic and symptomatic carotid endarterectomy (CEA) patients [20, 21]. Lagrangian strain estimation was initially developed by Shi et al. (2008)[22] followed by further elaboration by McCormick et al. (2012).[23] Later advancements by Meshram et al. (2018)[24] incorporated GPU acceleration, significantly improving computational performance.

The algorithm calculates strain distributions and quantitative indices using radiofrequency (RF) data acquired with either an Acuson S2000 or S3000 system equipped with an 18L6 transducer (Siemens Medical Solutions, Malvern, PA, USA). The process utilizes binary segmentation of the arterial wall from RF-derived B-mode images, and uses displacement tracking with a three-level pyramidal hierarchy. The accumulated displacements result in the Lagrangian strain tensor, from which scalar strain indices are obtained through Eigen analysis.

For computational purposes, the GPU-based algorithm employs an NVIDIA K40 GPU using CUDA programming, following the methodology described by Meshram et al. (2018).[24] To ensure precision, manual binary segmentation of carotid walls was performed by a trained sonographer.

6.2.2 Definition of Atherosclerosis Data Groups

The study cohort consisted of 181 healthy individuals (75 males and 106 females) aged between 18 and 88 years, recruited from the University of Wisconsin-Madison between December 2021

and January 2025. Participants were included if they were not receiving active treatment for hypertension or hyperlipidemia. Data collection involved demographic details, clinical history, and laboratory measurements, including age, sex, body mass index (BMI), smoking status, blood pressure, fasting lipid profiles (total cholesterol, LDL-C, HDL-C, triglycerides), high-sensitivity C-reactive protein (hs-CRP), and hemoglobin A1c levels. Additionally, a trained physician assessed the presence of carotid plaque. All participants provided informed consent under a protocol approved by the University of Wisconsin-Madison Institutional Review Board.

This first part of the study analyzed radiofrequency (RF) ultrasound data from the right and left common carotid arteries (CCAs) for 169 of the participants. These individuals were categorized into two groups: Group 1 (those diagnosed with atherosclerosis) and Group 2 (those without atherosclerosis. Groups were defined based on physician identification of arterial wall focal thickening and/or plaque presence on carotid ultrasound images. Demographic and metabolic panel data, including lipid profiles and hemoglobin A1c levels, were collected for all participants.

To further investigate the relationship between carotid wall strain and cardiovascular risk factors, an additional set of 12 participants (N=181) was included. All other CVD risk factors were tested but this analysis will focus on the hemoglobin A1c and ASCVD 10-year risk score group comparisons. Groups for hemoglobin A1c were determined with a threshold of 5.7%, where Group1 consisted of individuals with an HbA1c less than 5.7% and Group 2 which consisted of those with a HbA1c greater than 5.7%. The use of the 5.7% threshold was determined to follow the American Heart Association's cutoff for prediabetes. The 10-year ASCVD risk scores were calculated according to AHA guidelines [25] and a threshold of 5% 10-year risk (Group 1 <5% risk, Group 2 > 5% risk) was used to distinguish the groups.

6.2.3 Statistical Analysis

Comparisons between groups were performed using the Mann-Whitney U-test, given the non-parametric nature of the data. Strain indices, including maximum axial strain and shear strain, were analyzed alongside CVD risk parameters including age, sex, body-mass index, smoking status, systolic blood pressure, diastolic blood pressure, total cholesterol, high-density lipoprotein cholesterol, low-density lipoprotein cholesterol, triglycerides, high-sensitivity C-reactive protein, and hemoglobin A1c. Results were reported as median and interquartile range (IQR), with significance set at $p<0.05$.

For all members of the volunteer cohort, the 10-year risk of a first hard ASCVD event was calculated using the Pooled Cohort Equations as:

$$\textbf{Eq 6.1.} \quad \text{Risk} = 1 - S^0(10)^{e^{(\Sigma\beta_i X_i - \text{Mean}(\Sigma\beta_i X_i))}}$$

where $\boldsymbol{S_0}(10)$ represents the baseline survival rate at 10 years, and $\Sigma\beta_i X_i$ is the sum of each risk factor multiplied by its corresponding coefficient . The survival rates and coefficients are stratified by sex and race, and account for major risk factors including age, total cholesterol, HDL cholesterol, systolic blood pressure, treatment status, diabetes, and smoking history [25].

It is important to note that the 10-year ASCVD risk score is only validated for adults aged 40 to 79 years. For individuals under 40, the score has not been verified by the AHA, primarily because risk levels in this group are typically very low due to the strong age dependence of the equation. Furthermore, while lifetime ASCVD risk scores are available for some younger individuals, they are only validated for ages 20 to 59 [25], and no universal risk metric exists that spans the entire adult age range.

Despite these limitations, the 10-year ASCVD risk score has been applied to younger cohorts in previous studies [26-28]. Therefore, in this analysis, the 10-year ASCVD risk was calculated for all individuals in the dataset, including those under 40. However, results for this younger group should be interpreted with caution, as they fall outside the validated age range and are expected to have very low absolute risk. Future work may explore whether ultrasound-based strain indices can augment or extend traditional models to enable a more universal cardiovascular risk metric.

6.3 Results

Among the 169 participants in the carotid plaque group (60% female, aged 18–88 years, mean age 45), 25% (n=42) had carotid atherosclerosis. The carotid atherosclerosis group exhibited significantly lower maximum axial strain (25.56[16.92] vs 32.43[26.08]; $p<0.001$) and maximum shear strain (20.74[11.49] vs 27.50[21.72]; $p=0.013$), indicating increased arterial stiffness. Participants with atherosclerosis were significantly older (60.5[12] vs 38[21] years; $p<0.001$) and exhibited increased values of total cholesterol (211.5[44] vs 184[45] mg/dL; $p<0.001$), HDL-C (57.5[21] vs 52[20] mg/dL; $p=0.040$), LDL-C (134[39] vs 111[42] mg/dL; $p<0.001$), and hemoglobin A1c (5.6%[0.4%] vs 5.4%[0.4%]; $p<0.001$).

	With Atherosclerosis (n=42)	Without Atherosclerosis (n=127)	Mann-Whitney U Significance (p-value)
Maximum Axial Strain	25.56 [16.92]	32.43 [25.63]	**<0.001***
Maximum Lateral Strain	8.88 [5.45]	8.82 [6.96]	0.267
Maximum Shear Strain	20.74 [11.49]	27.50 [21.24]	**0.013***
Age (years)	60.5 [12]	38 [22]	**<0.001***
BMI (kg/m^2)	24.35 [6.45]	24.85 [5.07]	0.520
Systolic Blood Pressure (SBP) (mmHg)	128.5 [23]	128 [22]	0.116
Diastolic Blood Pressure (DBP) (mmHg)	79.5 [13]	78 [17]	0.448
Total Cholesterol(mg/dL)	211.5 [44]	184 [45]	**<0.001***
High-density lipoprotein cholesterol (HDL-C) (mg/dL)	57.5 [21]	52 [20]	**0.040***
Low-density lipoprotein cholesterol (LDL-C) (mg/dL)	134 [39]	111 [42]	**<0.001***
Triglycerides(mg/dL)	81.5 [38]	81.5 [51]	0.822
High-sensitivity C-Reactive Protein (hs-CRP) (mg/L)	0.85 [1.65]	1.2 [2.6]	0.302
Hemoglobin A1c (mg/dL)	5.6 [0.4]	5.4 [0.4]	**<0.001***

Table 6.1. Group Statistics for Atherosclerotic plaque groups. Reported as Median [IQR].
*p-value < 0.05

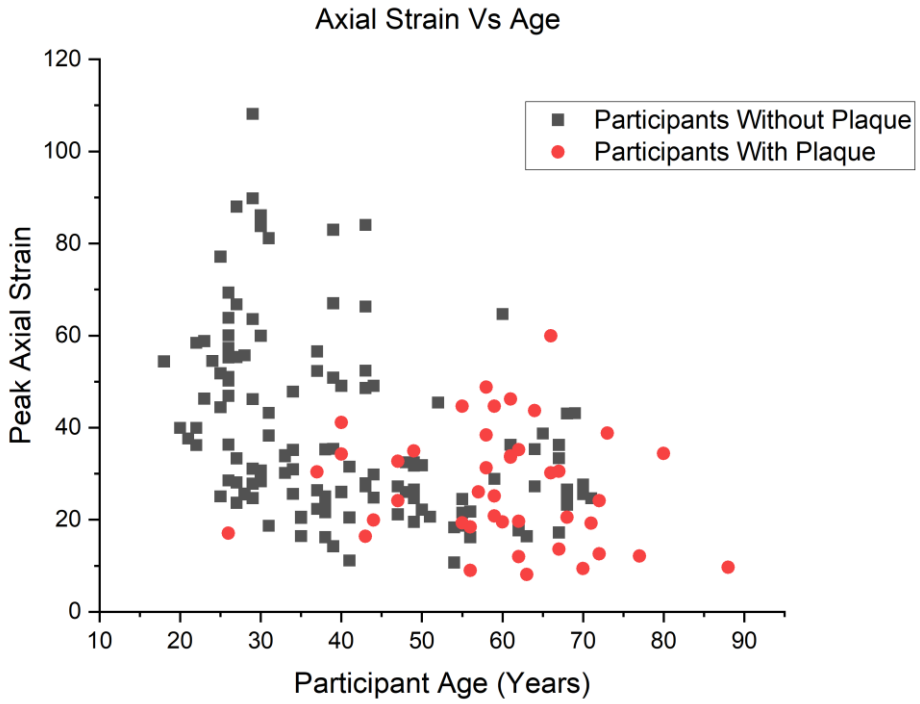

Figure 6.1. Plot of Axial Strain vs Participant Age. Separated by group

Among the 181 participants in the HbA1c test, 17% (n=30) had elevated HbA1c levels. The elevated HbA1c group (Group 2) had a mean HbA1c level of 5.9% ± 0.2%, compared to

5.4% ± 0.4% in the normal group (Group1; $p < 0.001$). Group 2 also exhibited significantly lower maximum axial strain (23.43 [15.05] vs 25.60 [26.81]; p=0.017), maximum lateral strain (7.65 [5.64] vs 9.01 [6.88]; p=0.034), and maximum shear strain (22.53 [15.82] vs 26.82 [19.91]; p=0.019), indicating increased arterial stiffness. Participants with elevated HbA1c were significantly older (61 [17.5] vs 39 [26] years; p<0.001) but had similar BMI (24.4 [3.9] vs 25.1 [5.8]; p=0.767) and blood pressure measurements (SBP: 129.5 [24.3] vs 128 [22] mmHg, p=0.545; DBP: 82 [17] vs 79 [15] mmHg, p=0.148).

No significant differences were observed in total cholesterol (203.5 [53] vs 190 [47] mg/dL; p=0.329), HDL-C (51.5 [16.3] vs 54 [22] mg/dL; p=0.426), LDL-C (125.5 [47.5] vs 114 [40] mg/dL; p=0.401), triglycerides (88.5 [35.5] vs 81 [48] mg/dL; p=0.081), or high-sensitivity C-reactive protein (hs-CRP) (0.9 [2.4] vs 1.2 [2.5] mg/L; p=0.976).

	Normal HbA1c (n=151)	Elevated HbA1c (n=30)	Mann-Whitney U Significance (p-value)
Maximum Axial Strain	25.60 [26.81]	23.43 [15.05]	**0.017***
Maximum Lateral Strain	9.01 [6.88]	7.65 [5.64]	**0.034***
Maximum Shear Strain	26.82 [19.91]	22.53 [15.82]	**0.019***
Age (years)	39 [26]	61 [17.5]	**<0.001***
BMI (kg/m^2)	25.1 [5.8]	24.4 [3.9]	0.767
Systolic Blood Pressure (SBP) (mmHg)	128 [22]	129.5 [24.3]	0.545
Diastolic Blood Pressure (DBP) (mmHg)	79 [15]	82 [17]	0.148
Total Cholesterol(mg/dL)	190 [47]	203.5 [53]	0.329
High-density lipoprotein cholesterol (HDL-C) (mg/dL)	54 [22]	51.5 [16.3]	0.426*
Low-density lipoprotein cholesterol (LDL-C) (mg/dL)	114 [40]	125.5 [47.5]	0.401*
Triglycerides(mg/dL)	81 [48]	88.5 [35.5]	0.081
High-sensitivity C-Reactive Protein (hs-CRP) (mg/L)	1.2 [2.5]	0.9 [2.4]	0.976
Hemoglobin A1c (mg/dL)	5.4 [0.4]	5.9 [0.2]	**<0.001***

Table 6.2. Group Statistics for Hemoglobin A1c groups. Reported as Median [IQR].
*p-value < 0.05

Among the 181 participants, 27% (n=49) had an estimated cardiovascular risk greater than 5%. The high-risk group (Group 2) exhibited significantly lower maximum axial strain (18.20 [17.50] vs 26.14 [25.96]; p<0.001), maximum lateral strain (7.91 [7.11] vs 9.01 [7.18]; p=0.009), and maximum shear strain (22.03 [21.00] vs 27.79 [14.43]; p<0.001), indicating increased arterial stiffness. Participants in Group 2 were significantly older (66 [11] vs 37 [18.3] years; p<0.001) but had comparable BMI (24.4 [5.0] vs 25.1 [7.2]; p=0.666) and blood pressure measurements (SBP: 131 [23] vs 126.5 [20] mmHg, p=0.218; DBP: 81 [15] vs 77.5 [15] mmHg, p=0.133).

Participants with higher cardiovascular risk demonstrated increased levels of total cholesterol (208 [39] vs 185.5 [44] mg/dL; p<0.001), LDL-C (128 [30] vs 112 [41.8] mg/dL; p<0.001), triglycerides (87 [47] vs 79.5 [49.3] mg/dL; p=0.018), and hemoglobin A1c (5.6 [0.4] vs 5.3 [0.4]; p<0.001). No significant differences were observed in HDL-C (54 [19] vs 53 [23] mg/dL; p=0.957) or high-sensitivity C-reactive protein (hs-CRP) (0.9 [2.6] vs 1.1 [2.6] mg/L; p=0.613).

	<5% Risk (n=132)	>5% Risk (n=49)	Mann-Whitney U Significance (p-value)
Maximum Axial Strain	26.14 [25.96]	18.20 [17.50]	**<0.001***
Maximum Lateral Strain	9.01 [7.18]	7.91 [7.11]	**0.009***
Maximum Shear Strain	27.79 [14.43]	22.03 [21.00]	**<0.001***
Age (years)	37 [18.3]	66 [11]	**<0.001***
BMI (kg/m^2)	25.1 [7.2]	24.4 [5.0]	0.666
Systolic Blood Pressure (SBP) (mmHg)	126.5 [20]	131 [23]	0.218
Diastolic Blood Pressure (DBP) (mmHg)	77.5 [15]	81 [15]	0.133
Total Cholesterol(mg/dL)	185.5 [44]	208 [39]	**<0.001***
High-density lipoprotein cholesterol (HDL-C) (mg/dL)	53 [23]	54[19]	0.957
Low-density lipoprotein cholesterol (LDL-C) (mg/dL)	112 [41.8]	128 [30]	**<0.001***
Triglycerides(mg/dL)	79.5 [49.3]	87 [47]	**0.018***
High-sensitivity C-Reactive Protein (hs-CRP) (mg/L)	1.1 [2.6]	0.9 [2.6]	0.613
Hemoglobin A1c (mg/dL)	5.3 [0.4]	5.6 [0.4]	**<0.001***

Table 6.3. Group Statistics for 10-year ASCVD risk groups. Reported as Median [IQR].
*p-value < 0.05

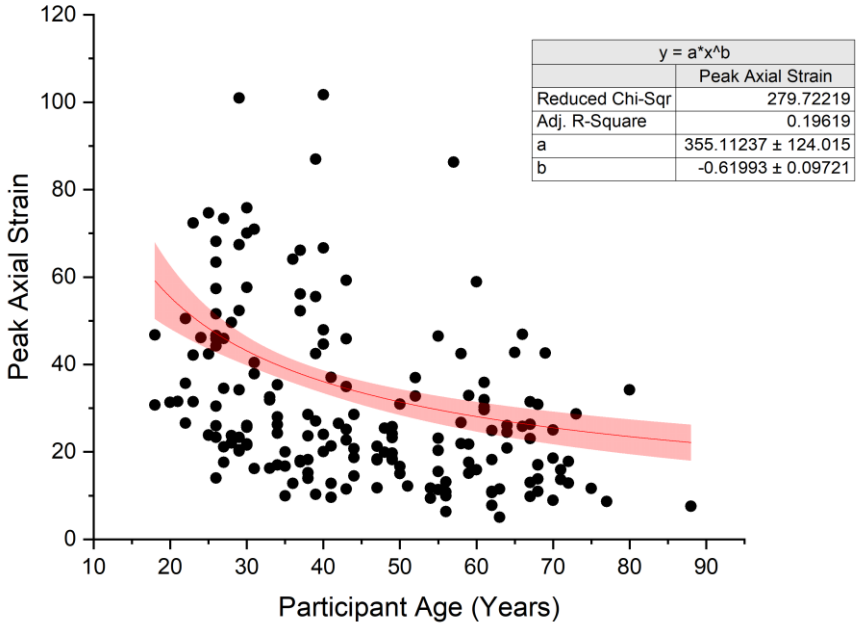

Figure 6.2. Plot of Axial Strain vs Participant Age.

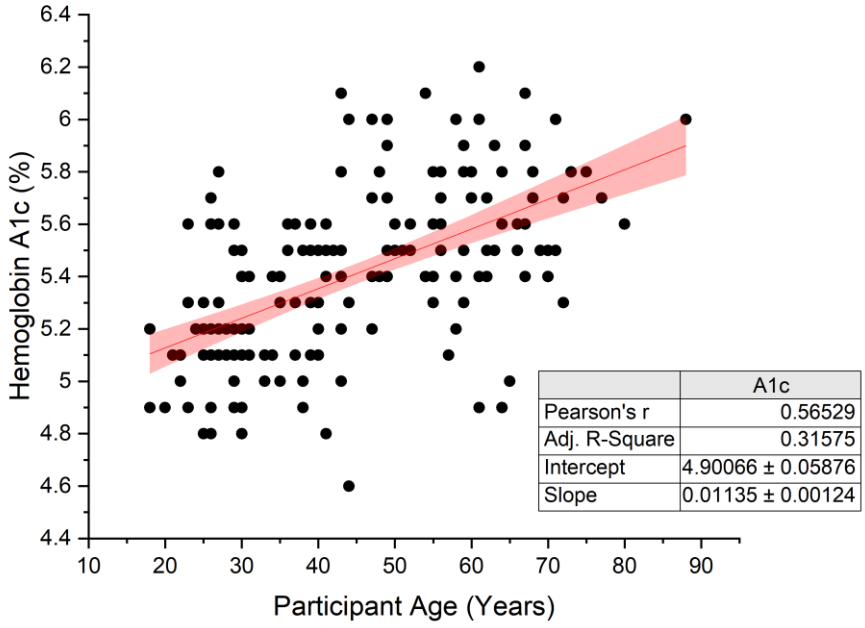

Figure 6.3. Plot of Hemoglobin A1c vs Participant Age.

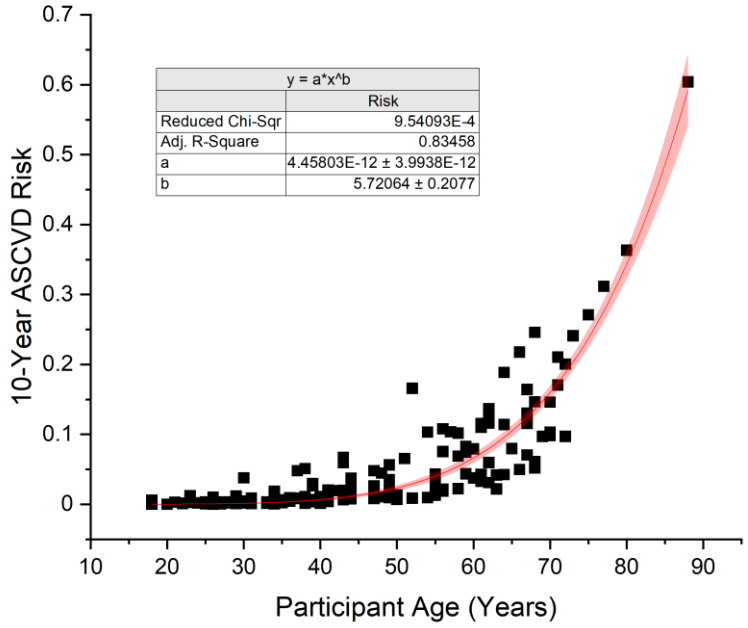

Figure 6.4. Plot of 10-year ASCVD Risk Score vs Participant Age.

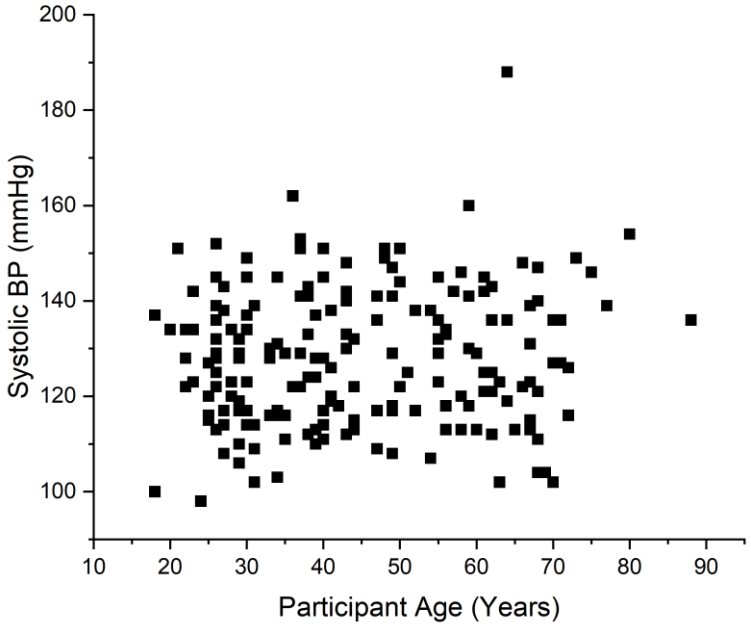

Figure 6.5. Plot of Systolic Blood Pressure vs Participant Age.

6.4 Discussion

6.4.1 Comparison of Atherosclerotic Plaque Groups

Among the 169 participants in the carotid plaque groups (60% female, aged 18–88 years, mean age 45), 25% (n=42) had carotid atherosclerosis. The carotid atherosclerosis group exhibited significantly lower maximum axial strain (25.56 [16.92] vs 32.43 [26.08]; $p<0.001$) and maximum shear strain (20.74 [11.49] vs 27.50 [21.72]; $p=0.013$), indicating increased arterial stiffness. Participants with atherosclerosis were significantly older (60.5 [12] vs 38 [21] years; $p<0.001$) and exhibited increased values of total cholesterol (211.5 [44] vs 184 [45] mg/dL; $p<0.001$), HDL-C (57.5 [21] vs 52 [20] mg/dL; $p=0.040$), LDL-C (134 [39] vs 111 [42] mg/dL; $p<0.001$), and hemoglobin A1c (5.6% [0.4%] vs 5.4% [0.4%]; $p<0.001$). These findings highlight that increased arterial stiffness in the carotid atherosclerosis group is associated with older age and elevated lipid profiles, which are well-established cardiovascular risk factors. The observed differences in strain indices suggest that carotid plaque presence correlates with reduced vascular compliance, emphasizing the clinical relevance of strain measurements for assessing arterial health in subjects with atherosclerosis.

6.4.2 Comparison of Hemoglobin A1c Groups

Among the 181 participants who underwent HbA1c testing, 17% (n=30) had elevated HbA1c levels. The elevated HbA1c group demonstrated significantly lower maximum axial strain (23.43 [15.05] vs 25.60 [26.81]; $p=0.017$), maximum lateral strain (7.65 [5.64] vs 9.01 [6.88]; $p=0.034$), and maximum shear strain (22.53 [15.82] vs 26.82 [19.91]; $p=0.019$), indicating increased arterial stiffness. Notably, the elevated HbA1c group was significantly older (61 [17.5] vs 39 [26] years; $p<0.001$) but did not differ significantly in BMI (24.4 [3.9] vs 25.1 [5.8]; $p=0.767$) or blood pressure (SBP: 129.5 [24.3] vs 128 [22] mmHg, $p=0.545$; DBP: 82 [17] vs 79 [15] mmHg,

p=0.148). No significant differences were observed in total cholesterol (203.5 [53] vs 190 [47] mg/dL; p=0.329), HDL-C (51.5 [16.3] vs 54 [22] mg/dL; p=0.426), LDL-C (125.5 [47.5] vs 114 [40] mg/dL; p=0.401), triglycerides (88.5 [35.5] vs 81 [48] mg/dL; p=0.081), or high-sensitivity C-reactive protein (hs-CRP) (0.9 [2.4] vs 1.2 [2.5] mg/L; p=0.976). These findings suggest that increased arterial stiffness in the elevated HbA1c group is more strongly associated with age rather than differences in BMI, blood pressure, or lipid profiles. The absence of significant differences in cholesterol levels and inflammatory markers between groups indicates that hyperglycemia may independently contribute to arterial stiffness.

6.4.3 Comparison of 10-year Risk Groups

In this study, we examined the relationship between cardiovascular risk and carotid arterial strain indices among 181 participants, of whom 27% (n=49) had an estimated cardiovascular risk greater than 5%. Our findings revealed that participants in the high-risk group exhibited significantly lower maximum axial strain (18.20 [17.50] vs 26.14 [25.96]; p<0.001), maximum lateral strain (7.91 [7.11] vs 9.01 [7.18]; p=0.009), and maximum shear strain (22.03 [21.00] vs 27.79 [14.43]; p<0.001). These results indicate increased arterial stiffness among individuals with elevated cardiovascular risk, supporting previous literature [29-34] that associates reduced carotid strain with arterial wall changes linked to atherosclerosis and cardiovascular disease.

Age emerged as a significant determinant, as the high-risk group was notably older (66 [11] vs 37 [18.3] years; p<0.001), consistent with the well-established association between advancing age and increased cardiovascular risk. However, BMI and blood pressure did not differ significantly between groups, suggesting that the observed differences in strain may not solely result from these traditional risk factors.

Participants in the high-risk group also exhibited increased levels of total cholesterol (208 [39] vs 185.5 [44] mg/dL; p<0.001), LDL-C (128 [30] vs 112 [41.8] mg/dL; p<0.001), triglycerides (87 [47] vs 79.5 [49.3]; p=0.018), and hemoglobin A1c (5.6 [0.4] vs 5.3 [0.4]; p<0.001). Elevated LDL-C and triglycerides are well-known contributors to atherosclerosis, and elevated HbA1c reflects metabolic dysregulation commonly seen in patients with increased cardiovascular risk.[17, 18] Interestingly, no significant differences were found in HDL-C (54 [19] vs 53 [23] mg/dL; p=0.957) or hs-CRP (0.9 [2.6] vs 1.1 [2.6] mg/L; p=0.613), suggesting that lipid abnormalities and glucose regulation may play a more prominent role in arterial stiffness within this cohort.

The results underscore the potential utility of strain indices as biomarkers for cardiovascular risk, particularly in the context of aging and metabolic health.

6.4.4 Findings and Limitations

Age is known to be a major risk factor in both plaque development and vessel stiffening. Figure 6.2 demonstrates that axial strain exhibits a very gradual exponential decay as age increases ($x^{-0.62}$), indicating a nonlinear relationship between age and strain. This trend supports the notion that aging contributes to arterial stiffening, reducing the elastic properties of the vessel wall. Additionally, Figure 6.3 shows a linear increase in hemoglobin A1c with age, highlighting the metabolic changes that occur with aging and their potential link to increased cardiovascular risk. Furthermore, Figure 6.4 shows that the cardiovascular risk score increases exponentially with age, emphasizing that aging is a dominant factor influencing cardiovascular risk profiles.

It is important to consider that strain is influenced by the blood pressure gradient through the vessel. However, Figure 6.5 shows that systolic blood pressure remains relatively constant across

ages, indicating that while blood pressure adds variability to the relationship between age and strain, it does not act as a confounding factor. This finding suggests that the age-related decrease in strain is not driven primarily by blood pressure differences but rather by intrinsic changes in vascular properties.

A key limitation of this analysis is the use of the 10-year ASCVD risk score, which is only validated for individuals aged 40 to 79. As a result, risk estimates for participants under 40 fall outside the score's intended range and should be interpreted with caution. While these estimates can serve as rough indicators of short-term cardiovascular risk—and are generally low in younger individuals due to the model's strong dependence on age—they are not formally verified. Furthermore, there is currently no universally accepted risk metric that spans all adult age groups. Future studies may benefit from incorporating additional markers, such as strain imaging, to improve risk prediction across the lifespan. It may also be useful in future work to stratify cohorts by short-term (10-year) and long-term (lifetime or 30-year) risk to better capture age-specific risk profiles.

In conclusion, our study demonstrates that individuals with elevated cardiovascular risk exhibit reduced carotid strain indices, likely reflecting increased arterial stiffness. These findings suggest that atherosclerosis is associated with reduced carotid artery strain indices, reinforcing the role of arterial stiffness in atherosclerotic vascular pathology. These results align with prior research demonstrating that chronic atherosclerosis leads to increased arterial stiffness, thereby reducing strain measurements. The observed metabolic alterations further indicate that atherosclerosis contributes to systemic vascular remodeling. However, age-related effects on arterial stiffening must be considered when interpreting these results. Future studies should aim for a more balanced

representation of individuals within each age group (e.g., carotid plaque and no plaque, high cardiovascular risk and low cardiovascular risk) and incorporate longitudinal analyses to differentiate atherosclerosis-induced stiffening from age-related arterial changes.

6.5 References

[1] K. Kobiyama, and K. Ley, "Atherosclerosis," *Circ Res,* vol. 123, no. 10, pp. 1118-1120, Oct 26, 2018.

[2] S. Jebari-Benslaiman, U. Galicia-García, A. Larrea-Sebal, J. R. Olaetxea, I. Alloza, K. Vandenbroeck, A. Benito-Vicente, and C. Martín, "Pathophysiology of Atherosclerosis," *Int J Mol Sci,* vol. 23, no. 6, Mar 20, 2022.

[3] D. A. Chistiakov, A. A. Melnichenko, V. A. Myasoedova, A. V. Grechko, and A. N. Orekhov, "Mechanisms of foam cell formation in atherosclerosis," *J Mol Med (Berl),* vol. 95, no. 11, pp. 1153-1165, Nov, 2017.

[4] M. R. Bennett, S. Sinha, and G. K. Owens, "Vascular Smooth Muscle Cells in Atherosclerosis," *Circ Res,* vol. 118, no. 4, pp. 692-702, Feb 19, 2016.

[5] A. C. Newby, and A. B. Zaltsman, "Fibrous cap formation or destruction — the critical importance of vascular smooth muscle cell proliferation, migration and matrix formation," *Cardiovascular Research,* vol. 41, no. 2, pp. 345-360, 1999.

[6] J. F. Bentzon, F. Otsuka, R. Virmani, and E. Falk, "Mechanisms of plaque formation and rupture," *Circ Res,* vol. 114, no. 12, pp. 1852-66, Jun 06, 2014.

[7] V. Fuster, B. Stein, J. A. Ambrose, L. Badimon, J. J. Badimon, and J. H. Chesebro, "Atherosclerotic plaque rupture and thrombosis. Evolving concepts," *Circulation,* vol. 82, no. 3 Suppl, pp. Ii47-59, Sep, 1990.

[8] T. J. Guzik, and R. M. Touyz, "Oxidative Stress, Inflammation, and Vascular Aging in Hypertension," *Hypertension,* vol. 70, no. 4, pp. 660-667, Oct, 2017.

[9] Y. Higashi, "Roles of Oxidative Stress and Inflammation in Vascular Endothelial Dysfunction-Related Disease," *Antioxidants (Basel),* vol. 11, no. 10, Sep 30, 2022.

[10] J. J. Wentzel, Y. S. Chatzizisis, F. J. H. Gijsen, G. D. Giannoglou, C. L. Feldman, and P. H. Stone, "Endothelial shear stress in the evolution of coronary atherosclerotic plaque and vascular remodelling: current understanding and remaining questions," *Cardiovascular Research,* vol. 96, no. 2, pp. 234-243, 2012.

[11] P. H. Stone, A. U. Coskun, Y. Yeghiazarians, S. Kinlay, J. J. Popma, R. E. Kuntz, and C. L. Feldman, "Prediction of sites of coronary atherosclerosis progression: In vivo profiling

of endothelial shear stress, lumen, and outer vessel wall characteristics to predict vascular behavior," *Curr Opin Cardiol,* vol. 18, no. 6, pp. 458-70, Nov, 2003.

[12] P. A. Cahill, and E. M. Redmond, "Vascular endothelium - Gatekeeper of vessel health," *Atherosclerosis,* vol. 248, pp. 97-109, May, 2016.

[13] N. O. Fomenko, and O. O. Larin, "Investigating the Impact of Atherosclerotic Plaque Size on Human Arterial Wall Stress-Strain Hysteresis Loop and Deformed State Pattern," *Strength of Materials,* vol. 56, no. 5, pp. 999-1009, 2024.

[14] A. Karimi, M. Navidbakhsh, A. Shojaei, and S. Faghihi, "Measurement of the uniaxial mechanical properties of healthy and atherosclerotic human coronary arteries," *Mater Sci Eng C Mater Biol Appl,* vol. 33, no. 5, pp. 2550-4, Jul 01, 2013.

[15] Y. Jiang, K. Kohara, and K. Hiwada, "Association between risk factors for atherosclerosis and mechanical forces in carotid artery," *Stroke,* vol. 31, no. 10, pp. 2319-24, Oct, 2000.

[16] Y. H. Lee, M. H. Shin, J. S. Choi, J. A. Rhee, H. S. Nam, S. K. Jeong, K. S. Park, S. Y. Ryu, S. W. Choi, B. H. Kim, G. J. Oh, and S. S. Kweon, "HbA1c is significantly associated with arterial stiffness but not with carotid atherosclerosis in a community-based population without type 2 diabetes: The Dong-gu study," *Atherosclerosis,* vol. 247, pp. 1-6, Apr, 2016.

[17] Y. Li, Y. Liu, S. Liu, M. Gao, W. Wang, K. Chen, and L. Huang, "Diabetic vascular diseases: molecular mechanisms and therapeutic strategies," *Signal Transduct Target Ther,* vol. 8, no. 1, pp. 152, Apr 10, 2023.

[18] M. M. van der Bruggen, B. Spronck, T. Delhaas, K. D. Reesink, and C. G. Schalkwijk, "The Putative Role of Methylglyoxal in Arterial Stiffening: A Review," *Heart Lung Circ,* vol. 30, no. 11, pp. 1681-1693, Nov, 2021.

[19] W. T. Wang, P. F. Hsu, C. C. Lin, Y. J. Wang, Y. Z. Ding, T. L. Liou, Y. W. Wang, S. S. Huang, T. M. Lu, P. H. Huang, J. W. Chen, W. L. Chan, S. J. Lin, and H. B. Leu, "Hemoglobin A1C Levels are Independently Associated with the Risk of Coronary Atherosclerotic Plaques in Patients without Diabetes: A Cross-Sectional Study," *J Atheroscler Thromb,* vol. 27, no. 8, pp. 789-800, Aug 01, 2020.

[20] X. Wang, D. C. Jackson, C. C. Mitchell, T. Varghese, S. M. Wilbrand, B. G. Rocque, B. P. Hermann, and R. J. Dempsey, "Classification of Symptomatic and Asymptomatic Patients with and without Cognitive Decline Using Non-invasive Carotid Plaque Strain Indices as Biomarkers," *Ultrasound Med Biol,* vol. 42, no. 4, pp. 909-18, Apr, 2016.

[21] N. H. Meshram, D. Jackson, T. Varghese, C. C. Mitchell, S. M. Wilbrand, R. J. Dempsey, and B. P. Hermann, "A Cross-Sectional Investigation of Cognition and Ultrasound-Based Vascular Strain Indices," *Arch Clin Neuropsychol,* vol. 35, no. 1, pp. 46-55, Jan 24, 2019.

[22] H. Shi, C. C. Mitchell, M. McCormick, M. A. Kliewer, R. J. Dempsey, and T. Varghese, "Preliminary in vivo atherosclerotic carotid plaque characterization using the accumulated

axial strain and relative lateral shift strain indices," *Phys Med Biol,* vol. 53, no. 22, pp. 6377-94, Nov 21, 2008.

[23] M. McCormick, T. Varghese, X. Wang, C. Mitchell, M. A. Kliewer, and R. J. Dempsey, "Methods for robust in vivo strain estimation in the carotid artery," *Phys Med Biol,* vol. 57, no. 22, pp. 7329-53, Nov 21, 2012.

[24] N. H. Meshram, and T. Varghese, "GPU Accelerated Multilevel Lagrangian Carotid Strain Imaging," *IEEE Trans Ultrason Ferroelectr Freq Control,* vol. 65, no. 8, pp. 1370-1379, Aug, 2018.

[25] D. C. Goff, D. M. Lloyd-Jones, G. Bennett, S. Coady, R. B. D'Agostino, R. Gibbons, P. Greenland, D. T. Lackland, D. Levy, C. J. O'Donnell, J. G. Robinson, J. S. Schwartz, S. T. Shero, S. C. Smith, P. Sorlie, N. J. Stone, P. W. Wilson, H. S. Jordan, L. Nevo, J. Wnek, J. L. Anderson, J. L. Halperin, N. M. Albert, B. Bozkurt, R. G. Brindis, L. H. Curtis, D. DeMets, J. S. Hochman, R. J. Kovacs, E. M. Ohman, S. J. Pressler, F. W. Sellke, W. K. Shen, G. F. Tomaselli, and A. C. o. C. A. H. A. T. F. o. P. Guidelines, "2013 ACC/AHA guideline on the assessment of cardiovascular risk: a report of the American College of Cardiology/American Heart Association Task Force on Practice Guidelines," *Circulation,* vol. 129, no. 25 Suppl 2, pp. S49-73, Jun 24, 2014.

[26] J. An, Y. Zhang, H. Zhou, M. Zhou, M. M. Safford, P. Muntner, A. E. Moran, and K. Reynolds, "Incidence of Atherosclerotic Cardiovascular Disease in Young Adults at Low Short-Term But High Long-Term Risk," *J Am Coll Cardiol,* vol. 81, no. 7, pp. 623-632, Feb 21, 2023.

[27] J. D. Berry, K. Liu, A. R. Folsom, C. E. Lewis, J. J. Carr, J. F. Polak, S. Shea, S. Sidney, D. H. O'Leary, C. Chan, and D. M. Lloyd-Jones, "Prevalence and progression of subclinical atherosclerosis in younger adults with low short-term but high lifetime estimated risk for cardiovascular disease: the coronary artery risk development in young adults study and multi-ethnic study of atherosclerosis," *Circulation,* vol. 119, no. 3, pp. 382-9, Jan 27, 2009.

[28] A. K. Marma, J. D. Berry, H. Ning, S. D. Persell, and D. M. Lloyd-Jones, "Distribution of 10-year and lifetime predicted risks for cardiovascular disease in US adults: findings from the National Health and Nutrition Examination Survey 2003 to 2006," *Circ Cardiovasc Qual Outcomes,* vol. 3, no. 1, pp. 8-14, Jan, 2010.

[29] C. D. Rodríguez-Ariza, A. Cabrera-Villamizar, A. L. Rodríguez-Pulido, S. Callegari, N. A. Ossa Rodríguez, M. Pinilla-Roncancio, S. M. Moreno López, and C. A. Sánchez-Vallejo, "External validation of the ACC/AHA ASCVD risk score in a Colombian population cohort," *Sci Rep,* vol. 13, no. 1, pp. 6139, Apr 15, 2023.

[30] A. Bulum, G. Ivanac, F. Mandurić, L. Pfeifer, M. Bulum, E. Divjak, S. Radoš, and B. Brkljačić, "Contribution of UltraFast™ Ultrasound and Shear Wave Elastography in the Imaging of Carotid Artery Disease," *Diagnostics (Basel),* vol. 12, no. 5, May 8, 2022.

[31] X. Xu, B. Wang, C. Ren, J. Hu, D. A. Greenberg, T. Chen, L. Xie, and K. Jin, "Age-related Impairment of Vascular Structure and Functions," *Aging Dis,* vol. 8, no. 5, pp. 590-610, Oct, 2017.

[32] J. D. Cameron, C. Rajkumar, B. A. Kingwell, G. L. Jennings, and A. M. Dart, "Higher systemic arterial compliance is associated with greater exercise time and lower blood pressure in a young older population," *J Am Geriatr Soc,* vol. 47, no. 6, pp. 653-6, Jun, 1999.

[33] L. J. Chalmers, K. C. Copeland, C. N. Hester, D. A. Fields, and A. W. Gardner, "Paradoxical increase in arterial compliance in obese pubertal children," *Angiology,* vol. 62, no. 7, pp. 565-70, Oct, 2011.

[34] A. W. Gardner, and D. E. Parker, "Association between arterial compliance and age in participants 9 to 77 years old," *Angiology,* vol. 61, no. 1, pp. 37-41, 2010.

Chapter 7: Cardiovascular Disease Risk Assessment Incorporating Lagrangian Strain Indices

7.1 Background

7.1.1 Strain Imaging in Cardiovascular Risk Assessment

Strain imaging is a valuable technique for assessing arterial wall mechanics and has been increasingly utilized in evaluating cardiovascular risk.[1, 2] Unlike traditional imaging methods that primarily measure vessel dimensions, strain imaging captures the dynamic deformation of arterial walls during the cardiac cycle. This biomechanical approach provides insights into vessel compliance and stiffness, which are critical markers of cardiovascular health.

Research has shown that arterial segments without atherosclerotic plaque exhibiting greater strain tend to be more compliant and more elastic in younger subjects, whereas regions with reduced strain indicate stiffness and potential pathological changes due to aging, diabetes. [3, 4] However, when plaque deposition is significant, plaque stiffness has to be evaluated in addition to arterial wall stiffness. This relationship is particularly important in assessing carotid plaque stability, as plaques with higher strain due to the presence of softer and lipid-rich plaque deposition are often more prone to rupture.[4, 5] Additionally, areas of reduced strain in plaque-free regions may reflect underlying vascular stiffness, potentially indicating an elevated risk of atherosclerosis development.[6, 7]

Our group has been actively developing noninvasive Lagrangian strain imaging techniques to better quantify the mechanical properties of the carotid artery wall and atherosclerotic carotid plaque. [8, 9] This method tracks the deformation of arterial segments throughout the cardiac cycle, offering precise measurements of wall strain and compliance. Previous studies by our team have

demonstrated the utility of Lagrangian strain in identifying carotid plaque vulnerability, highlighting its potential role in refining cardiovascular risk assessment. [5, 10-17]

Atherosclerotic cardiovascular disease (ASCVD) risk scores [18] for human subjects prone to cardiovascular or cerebrovascular disease is done based on medical history, blood pressure and a fasting lipid panel [18]. Both 10-year (40-79 years) and lifetime (20-59 years) risk for heart disease and stroke can be determined. We propose to incorporate risk-assessment based on ultrasound based quantitative metrics developed in our laboratory to improve assessment of ASCVD risk.

Several machine learning classifiers such as Random Forest, Support Vector Machine (SVM), XGBoost, among several approaches have been reported in the literature. We propose to utilize one of the models to assess ASCVD risk based on axial, lateral and shear strain indices, intima-media thickness (IMT), Doppler velocities, age, gender, ASCVD score, hemoglobin A1c, fasting lipid panel values, high-sensitivity C-reactive protein (hs-CRP), blood pressure, and cardiovascular disease (CVD) family history, for risk stratification in otherwise normal asymptomatic human subjects.

7.1.2 Random Forests: An Overview

Random Forests are ensemble learning methods that construct a multitude of decision trees during training and output the mode of the classes (for classification) or mean prediction (for regression) from all individual trees. The algorithm was introduced by Breiman (2001)[19] as a way to improve prediction accuracy by reducing overfitting, a common problem with individual decision trees.

One of the core techniques in Random Forests is bagging (Bootstrap Aggregating), where multiple trees are trained on different subsets of the data. Each tree is built using a random sample of

features, which enhances diversity among the trees and improves generalization. Due to this randomized approach, Random Forests are generally robust to noise and can effectively handle large datasets with high-dimensional feature spaces.

In healthcare applications, Random Forests have been widely used to predict patient outcomes, classify disease states, and assess health risks. For example, they have been applied to predict cardiovascular events based on electronic health record (EHR) data and to identify risk factors for chronic diseases [20, 21]. The model's ability to rank the importance of individual features makes it particularly valuable for interpreting risk factors in clinical studies.

7.1.3 XGBoost: An Overview

XGBoost (eXtreme Gradient Boosting) is a powerful and efficient machine learning algorithm widely used for classification, regression, and ranking tasks. It is based on gradient boosting, an ensemble learning method that builds additive models by training weak learners (typically decision trees) in a sequential manner. XGBoost is particularly known for its scalability, high performance, and ability to handle structured data effectively[22].

One of the key advantages of XGBoost is its implementation efficiency, which leverages second-order gradient information and optimizes model performance through techniques like tree pruning and parallel processing. It also supports regularization, which helps reduce overfitting—a common issue in complex healthcare datasets where the number of features can be large relative to the number of samples.

7.1.4 Applications of XGBoost in Health Risk Assessment

XGBoost has been extensively applied in the field of health risk prediction due to its robustness in handling mixed data types (numerical, categorical) and its capacity to model complex, non-linear relationships. For example, XGBoost has been successfully used to predict cardiovascular events by incorporating demographic, clinical, and laboratory variables [23]. In another study, XGBoost demonstrated superior performance compared to traditional logistic regression models when predicting the risk of type 2 diabetes [21].

More recently, XGBoost has been applied in the context of CVD risk assessment. Researchers have utilized XGBoost to estimate 10-year ASCVD risk by combining standard clinical variables with novel biomarkers, demonstrating that XGBoost-based models can outperform existing risk calculators [24]. Additionally, XGBoost has been employed to predict the presence of atherosclerotic plaques using ultrasound-derived metrics, including strain measurements and IMT, showing promising results in identifying high-risk individuals [21, 25].

7.1.5 Comparison with Similar Models: Random Forests

XGBoost and Random Forests share common ground as ensemble learning methods based on decision trees. While Random Forests aggregate the outputs of many independent decision trees to reduce variance and improve generalization, XGBoost builds trees sequentially with gradient boosting, reducing both bias and variance. This key difference makes XGBoost particularly effective when the data exhibits complex, non-linear relationships.

Another notable distinction lies in how the models handle errors. Random Forests use bootstrapping and random feature selection to prevent overfitting, whereas XGBoost directly

minimizes a loss function using gradient descent, making it more flexible in capturing interactions between features.

In healthcare applications, Random Forests are often preferred when model interpretability is a priority, as the contribution of individual features can be assessed through feature importance scores. In contrast, XGBoost generally achieves higher accuracy but at the cost of increased model complexity. Studies comparing the two methods have shown that XGBoost tends to outperform Random Forests in predicting health risks, particularly when data is high-dimensional or contains complex interactions [26, 27] .

7.1.6 Justification for Using XGBoost

The decision to use XGBoost in the current study was driven by several factors:

1. **Handling of Heterogeneous Data:** The dataset used for cardiovascular risk assessment contains both continuous variables (e.g., strain, blood pressure) and binary variables (e.g., plaque presence), which XGBoost can process effectively.
2. **Performance and Scalability:** Given the volume of data and the need for accurate risk prediction, XGBoost's efficiency and high predictive accuracy make it well-suited for this application.
3. **Proven Success in Similar Studies:** Previous studies have demonstrated that XGBoost is not only theoretically suitable but also empirically effective in predicting cardiovascular outcomes and health risks.

By leveraging the strengths of XGBoost, this study aims to develop a novel cardiovascular risk metric that integrates ultrasound-based strain data with traditional clinical measures to enhance risk stratification in a clinical setting.

7.2 Methods

7.2.1 Lagrangian Strain Estimation

Lagrangian strain estimation has been extensively reported in the literature, initially introduced by Shi et al. (2008)[28] and further detailed by McCormick et al. (2012).[15] Subsequent adaptations for GPU acceleration were made by Meshram et al. (2018)[11], significantly enhancing computational efficiency.

The algorithm leverages radiofrequency (RF) data acquired using Acuson S2000 or S3000 systems with an 18L6 transducer (Siemens Medical Solutions, Malvern, PA, USA) to compute strain distributions and quantitative indices within specified regions. The process begins with binary segmentations of the arterial wall from RF-derived B-mode images, followed by displacement tracking via a three-level pyramidal hierarchy. The accumulated displacements yield the Lagrangian strain tensor, from which scalar strain indices are derived through Eigen analysis.

For computational implementation, the GPU-based algorithm utilizes an NVIDIA K40 GPU with CUDA programming, as per the methods outlined by Meshram et al. (2018)[11]. Manual binary segmentation of carotid walls was conducted by a trained sonographer to maintain accuracy.

7.2.2 Data Collection and Preprocessing

The study cohort consisted of 181 healthy individuals (75 males and 106 females) aged between 18 and 88 years, recruited from the University of Wisconsin-Madison between December 2021 and January 2025. Participants were included if they were not receiving active treatment for hypertension or hyperlipidemia. Data collection involved demographic details, clinical history, and laboratory measurements, including age, sex, body mass index (BMI), smoking status, blood pressure, fasting lipid profiles (total cholesterol, LDL-C, HDL-C, triglycerides), hs-CRP, and hemoglobin A1c levels. Additionally, trained physicians assessed the presence of carotid plaque, and 10-year ASCVD risk scores were calculated according to AHA guidelines.[29] Participants provided informed consent under a protocol approved by the University of Wisconsin-Madison Institutional Review Board.

The 10-year risk of a first major ASCVD event for each participant was estimated using the Pooled Cohort Equations, which follow the formula:

$$\textbf{Eq 7.1.} \qquad \text{Risk} = 1 - S^0(10)^{e^{\left(\Sigma\beta_i X_i - \text{Mean}(\Sigma\beta_i X_i)\right)}}$$

In this equation, $\boldsymbol{S_0}(10)$ denotes the baseline survival probability at 10 years, and the summation term $\Sigma\beta_i X_i$ epresents a weighted combination of risk factors, including age, lipid levels, blood pressure, smoking status, diabetes, and treatment status. The coefficients and survival rates are specific to sex and race as defined in the ACC/AHA guidelines [29].

However, this risk model is only validated for adults aged 40 to 79 years. For individuals younger than 40, the predictive accuracy of the 10-year ASCVD score is uncertain, largely due to the model's heavy weighting on age, which typically results in near-zero risk estimates in younger populations. Although lifetime risk estimations are available, they are only validated for adults

between 20 and 59 years of age [29], leaving a gap in validated risk prediction across the entire adult lifespan.

Previous studies have nonetheless applied the 10-year ASCVD equation to younger populations [30-32], and this analysis follows that precedent by including all individuals, regardless of age. Still, it is essential to recognize that individuals under 40 fall outside the model's validated range and are likely to be classified as low-risk. This limitation highlights the potential role of additional biomarkers—such as strain-based imaging metrics—in developing more inclusive and sensitive risk assessment tools for all age groups.

Data cleaning involved removing duplicate entries and handling missing values by imputation where necessary. Binary variables (e.g., presence of plaque, hypertension, and diabetes) were converted from textual labels ('yes', 'no') to numeric binary format (1, 0). Continuous variables were normalized using the StandardScaler from Scikit-learn to ensure comparability across features.

7.2.3 Predictive Models

Two predictive models were developed:

1. **Plaque Presence Prediction:**
    - Features: Strain, cholesterol, blood pressure, age, BMI
    - Target: Presence of right and left carotid artery plaque
    - Model: XGBoost Regressor (XGBRegressor) to predict the presence of plaque.
2. **10-Year Cardiovascular Risk Estimation (Estimating ASCVD 10-year risk):**
    - Features: Strain, age, BMI, systolic blood pressure

- Target: Estimated 10-year cardiovascular risk score
- Model: XGBoost Regressor to predict continuous risk scores.

7.2.4 Model Training and Evaluation

Data were split into training and testing sets (80% training, 20% testing) using stratified sampling to maintain class balance. Features were scaled using the StandardScaler. The XGBRegressor was used for classification of plaque presence and for the continuous ASCVD risk prediction. Both models were optimized using hyperparameter tuning with cross-validation to prevent overfitting.

Model performance was evaluated using accuracy, precision, recall, and F1-score for plaque presence prediction (plaque on either side), and mean absolute error (MAE) and root mean squared error (RMSE) for ASCVD risk estimation. Both models used the XGBRegressor: one for classification of plaque presence and the other for continuous ASCVD risk prediction. Additionally, ROC AUC was calculated for binary predictions to assess discriminatory ability.

7.3 Results

7.3.1 Baseline Participant Characteristics

The study population comprised 181 participants (75 males and 106 females), aged 18 to 88 years (median age: 42 years). The median BMI was 24.9 kg/m², with a range from 17.5 to 51. Systolic blood pressure had a median of 128 mmHg (range: 98-188), while diastolic blood pressure had a median of 79 mmHg (range: 61-102). The median total cholesterol level was 193 mg/dL, with HDL-C at 53 mg/dL and LDL-C at 115 mg/dL. Triglyceride levels had a median of 82 mg/dL. Inflammatory marker levels were relatively low, with a median hs-CRP of 1.2 mg/L. Glycemic control appeared within normal limits, with a median hemoglobin A1c of 5.4 mg/dL. Among the

cohort, 21.5% presented with carotid plaque, while the median estimated 10-year ASCVD risk score was 1.1%.

	N	Median (inter-quartile range)	Range
Age, y	181	42 (29)	18-88
Sex (n, %)	181		
Male		75 (41.4%)	
Female		106 (58.6%)	
Body-mass Index (kg/m^2)	181	24.9 (5.6)	17.5-51
Systolic Blood Pressure (mmHg)	181	128 (22)	98-188
Diastolic Blood Pressure (mmHg)	181	79 (18)	61-102
Total Cholesterol (mg/dL)	181	193 (46)	114-316
High-density lipoprotein cholesterol (mg/dL)	181	53 (22)	25-109
Low-density lipoprotein cholesterol (mg/dL)	181	115 (40)	59-223
Triglycerides (mg/dL)	181	82 (44)	26-527
High-sensitivity C-Reactive Protein (mg/L)	181	1.2 (2.5)	0.299-17.9
Hemoglobin A1c (mg/dL)	181	5.4 (0.4)	4.6-6.2
Diagnosed Hypertension (Yes) (n, %)		8 (4.4%)	
Diagnosed Diabetes (Yes) (n, %)		2 (1.1%)	
Diagnosed Dyslipidemia (Yes) (n, %)		21 (11.6%)	
Carotid Plaque Presence (Yes) (n, %)		39 (21.5%)	
10year ASCVD risk score (%)	181	1.1% (5.29%)	0.01%-60.41%
Max Absolute Principal Strain peak strain value	181	36.4 (31.2)	11.9-149.3
Max Shear Strain peak strain value	181	52.8 (44.8)	18.3-204.3
Lateral Strain peak strain value	181	8.9 (6.9)	2.9-36.2
Shear Strain peak strain value	181	24.0 (19.1)	7.5-92.7
Axial Strain peak strain value	181	24.9 (23.3)	5.0-101.7

Table 7.1. Participant characteristics of the volunteer dataset (N=181)

7.3.2 Plaque Prediction

The XGBoost model used for predicting plaque presence was optimized with the following hyperparameters: colsample_bytree: 0.8, learning rate: 0.01, max depth: 3, number of estimators: 100, and subsample: 0.8. These hyperparameters were determined to balance model complexity and generalization performance.

7.3.2.1 *Model Performance*

The model's cross-validation R^2 scores ranged from 0.0355 to 0.2842, with a mean R^2 of 0.1234, indicating moderate predictive capability. The mean squared error (MSE) was calculated as 0.278, and the RMSE was 0.527, highlighting the degree of variance in predictions. The model's R^2 score of 0.108 indicates that approximately 10.8% of the variability in plaque presence could be explained by the input features. Furthermore, the Pearson correlation between predicted and true values was 0.374, suggesting a moderate linear relationship between predictions and actual outcomes. If a binary threshold is used, where values >50% are considered to be true, the Pearson correlation coefficient is 0.417.

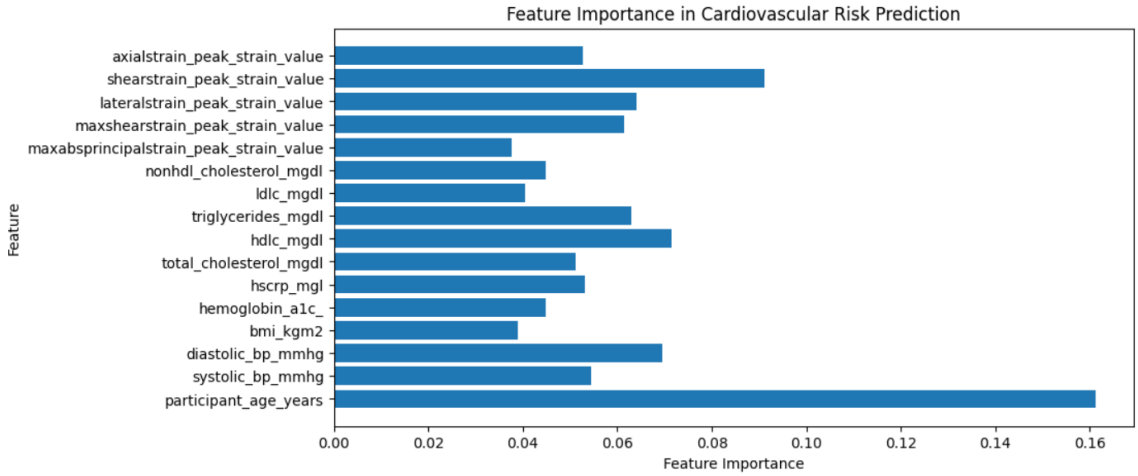

Figure 7.1. Feature Importance for Carotid Plaque prediction model

7.3.2.2 *Prediction Results*

An example of the prediction output includes both ground truth and predicted risk values. For instance, Record ID 153 had a ground truth of 1 (plaque present) with a predicted risk of plaque of 76%, while Record ID 42, which had no plaque, was predicted to have a 20% risk. Using a binary threshold, 82% of predicted cases in the test set agreed with the ground truth.

7.3.3 ASCVD Prediction

The XGBoost model used for predicting 10-year ASCVD risk was optimized with the following hyperparameters: colsample_bytree: 1.0, learning rate: 0.05, max depth: 3, number of estimators: 100, and subsample: 1.0. These parameters were chosen to maximize accuracy while maintaining model stability.

7.3.3.1 *Model Performance*

The cross-validation R^2 scores for ASCVD risk prediction ranged from 0.559 to 0.830, with a mean R^2 of 0.658. The model's MSE was calculated as 0.001, with an RMSE of 0.030, indicating highly accurate predictions. The R^2 score of 0.724 demonstrates that approximately 72.4% of the variance in ASCVD risk could be explained by the model. The Pearson correlation coefficient between predicted and actual values was 0.867, suggesting a strong linear relationship.

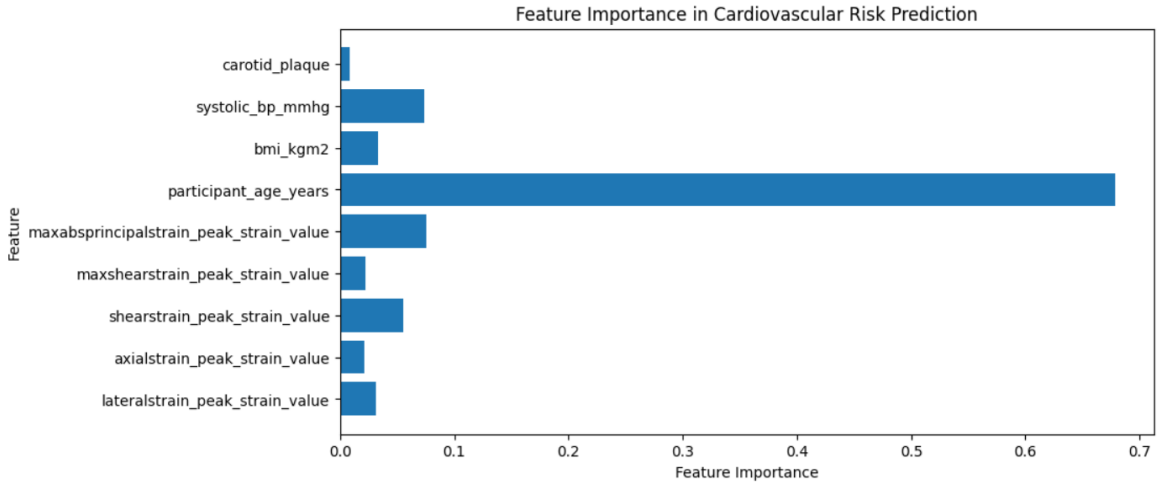

Figure 7.2. Feature Importance for 10-year risk prediction model

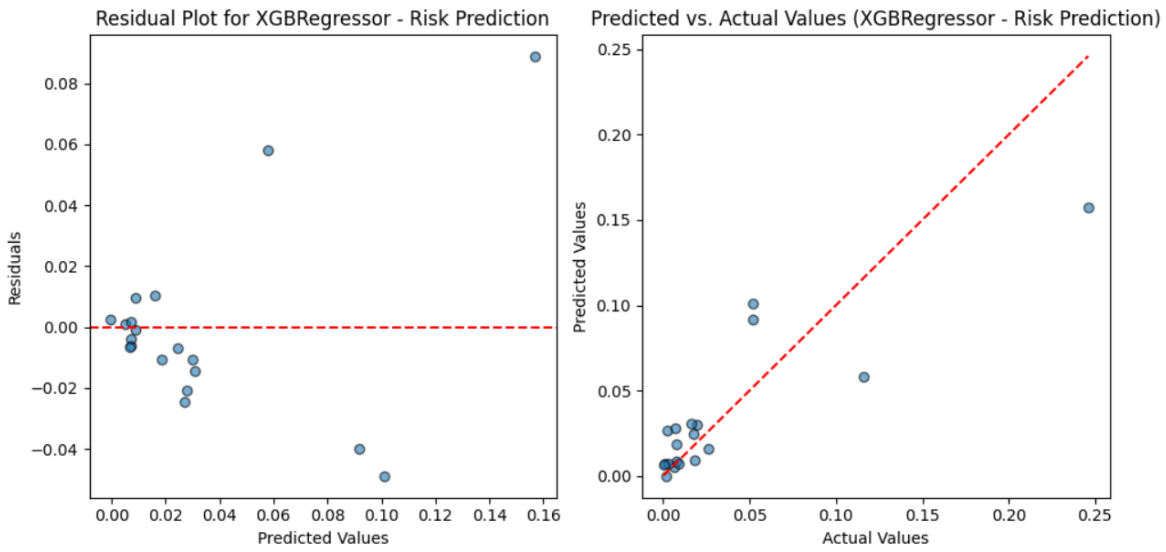

Figure 7.3. Residual and Predicted vs Actual plots for 10-year risk prediction model

7.3.3.2 *Prediction Results*

Example prediction outputs include ground truth and predicted ASCVD risk values. For instance, Record ID 153, which had a ground truth risk of 12%, was predicted to have a 6% risk, while Record ID 42, with a ground truth risk of 1%, was accurately predicted as having a 1% risk.

7.4 Discussion

7.4.1 Plaque Prediction

The XGBoost model used to predict plaque presence demonstrated moderate performance, as indicated by a mean R^2 of 0.123 and a relatively low Pearson correlation of 0.374 between predicted and actual values. These results suggest that the model captures some patterns related to plaque presence, but its predictive power is limited. In the test dataset (N=28), it correctly predicted outcomes for 23 volunteers (82%), but only predicted plaque presence in 3 out of the 6 (50%) cases with confirmed plaque. The variability in the cross-validation R^2 scores (ranging from 0.036 to 0.284) indicates potential inconsistencies in the model's generalization across different subsets

of the data. Age had the highest feature importance while shear strain was the highest importance amongst the strain values. This is notable considering previous research indicated that axial strain of the carotid walls was significantly correlated to the most cardiovascular risk factors.

One possible reason for the model's limited accuracy is the inherent complexity of predicting plaque presence, which may be influenced by a multitude of factors not captured by the selected features. Additionally, the binary nature of the plaque presence outcome (plaque or no plaque) inherently reduces predictive resolution compared to continuous risk scores. Another challenge is the potential imbalance in the dataset, where the occurrence of plaque is less frequent since this cohort was primarily comprised of normal asymptomatic volunteers with no history of blood pressure, blood thinners or cholesterol medications, leading the model to favor the majority class. Results in this category could improve on with patients with significant stenosis scheduled for carotid artery stenting (CAS) or carotid endarterectomy (CEA) that were analyzed earlier in the plaque segmentation chapters (references).[5, 10, 12, 13, 33-35]

7.4.2 ASCVD Risk Prediction

In contrast, the XGBoost model for estimating 10-year ASCVD risk demonstrated significantly better performance, with a mean R^2 of 0.658 and a strong Pearson correlation of 0.867. This high correlation reflects the model's capacity to accurately predict continuous risk scores, indicating that the selected features (strain, age, BMI, systolic blood pressure) effectively capture the risk profile. Moreover, the narrow range of cross-validation R^2 scores (0.559 to 0.830) highlights the model's stability and consistent performance. Once again, age is the highest importance to the model, though in this instance it could be due in part by the use of age in the calculation of the

ASCVD risk score. We also notably see that once again, shear strain is of higher importance than axial and lateral strain.

The superior performance of the ASCVD model compared to the plaque prediction model may be attributed to the more continuous nature of the risk score, which allows for finer predictive distinctions. Additionally, the features used for ASCVD prediction may be more closely related to cardiovascular risk, as they encompass both physiological measurements and established risk factors.

7.4.3 Comparative Analysis and Model Selection

The discrepancy between the two models highlights the challenge of predicting binary cardiovascular outcomes compared to estimating continuous risk scores. While the plaque prediction model provides some insight into the presence or absence of plaque, its limited accuracy suggests that it may not be sufficiently reliable for clinical use without further improvement in its current form. (See above statement at start of discussion section) Ideally the model would benefit from an increased sample of individuals with plaque presence. Conversely, the ASCVD risk prediction model exhibits robust performance and aligns well with existing methods for risk assessment, but it would also benefit from an increased sample size.

XGBoost's ability to handle heterogeneous data types (both binary and continuous) makes it a suitable choice for cardiovascular risk modeling. However, the relatively poor performance in plaque prediction is likely due to the cohort used. An expanded dataset to include a better distribution of participants with plaque presence in addition to the integration of longitudinal data of the same participants would aid in better refinement of both models.

7.4.4 Study Limitations and Future Directions

A key limitation of this study is the reliance on a limited set of clinical and imaging features, which may not fully capture the underlying complexity of cardiovascular risk. Moreover, the cross-sectional nature of the dataset may reduce the generalizability of the models to different populations. Future work could include longitudinal data to better model changes in risk over time. It would also be aided by adding additional data sets for subjects who are at increased ASCVD risk. With limited examples of individuals with diabetes, hypertension, and significant imbalances in cases with plaque compared to those without, it would be beneficial to look at a more varied dataset compared to a fairly healthy one such as this cohort.

The potential for overfitting, especially in the plaque prediction model, should be addressed by further regularization and cross-validation techniques. Exploring more complex ensemble models, such as stacking or hybrid approaches that integrate multiple algorithms, could also improve performance.

In conclusion, while the ASCVD prediction model shows promising accuracy and stability, the plaque prediction model requires further refinement by incorporating subjects with higher ASCVD scores in the XGBoost model training along with CAS and CEA patients. Future research should focus on enhancing feature selection, incorporating multi-modal data, and improving model interpretability to make the results clinically applicable.

7.5 References

[1] B. D. Hoit, “Strain and strain rate echocardiography and coronary artery disease,” *Circ Cardiovasc Imaging,* vol. 4, no. 2, pp. 179-90, Mar, 2011.

[2] S. F. Arnăutu, V. I. Morariu, D. A. Arnăutu, and M. C. Tomescu, "The Predictive Value of Carotid Artery Strain and Strain-Rate in Assessing the 3-Year Risk for Stroke and Acute Coronary Syndrome in Patients with Metabolic Syndrome," *Rev Cardiovasc Med,* vol. 23, no. 4, pp. 146, Apr, 2022.

[3] C. Zou, Y. Jiao, X. Li, C. Zheng, M. Chen, and C. Hu, "Role of ultrasonography in the evaluation of correlation between strain and elasticity of common carotid artery in patients with diabetic nephropathy," *Int J Clin Exp Med,* vol. 8, no. 10, pp. 17765-72, 2015.

[4] J. Ohayon, A. M. Gharib, A. Garcia, J. Heroux, S. K. Yazdani, M. Malvè, P. Tracqui, M. A. Martinez, M. Doblare, G. Finet, and R. I. Pettigrew, "Is arterial wall-strain stiffening an additional process responsible for atherosclerosis in coronary bifurcations?: an in vivo study based on dynamic CT and MRI," *Am J Physiol Heart Circ Physiol,* vol. 301, no. 3, pp. H1097-106, Sep, 2011.

[5] N. H. Meshram, T. Varghese, C. C. Mitchell, D. C. Jackson, S. M. Wilbrand, B. P. Hermann, and R. J. Dempsey, "Quantification of carotid artery plaque stability with multiple region of interest based ultrasound strain indices and relationship with cognition," *Phys Med Biol,* vol. 62, no. 15, pp. 6341-6360, Jul 17, 2017.

[6] H. H. G. Hansen, A. H. M. Bekkers, I. C. L. van den Munckhof, E. van der Kolk, F. J. A. Meijer, M. van der Graaf, J. H. W. Rutten, and C. L. de Korte, "Ultrasound Strain Imaging for Characterizing Atherosclerotic Plaque in the Carotid Arteries of Asymptomatic Subjects," *Ultrasound Med Biol,* vol. 51, no. 2, pp. 321-329, Feb, 2025.

[7] N. M. van Popele, D. E. Grobbee, M. L. Bots, R. Asmar, J. Topouchian, R. S. Reneman, A. P. Hoeks, D. A. van der Kuip, A. Hofman, and J. C. Witteman, "Association between arterial stiffness and atherosclerosis: the Rotterdam Study," *Stroke,* vol. 32, no. 2, pp. 454-60, Feb, 2001.

[8] W. Ge, C. G. Krueger, A. Weichmann, D. Shanmuganayagam, and T. Varghese, "Displacement and strain estimation for evaluation of arterial wall stiffness using a familial hypercholesterolemia swine model of atherosclerosis," *Med Phys,* vol. 39, no. 7, pp. 4483-92, Jul, 2012.

[9] R. A. Mukaddim, Y. Liu, M. Graham, J. C. Eickhoff, A. M. Weichmann, M. C. Tattersall, C. E. Korcarz, J. H. Stein, T. Varghese, K. W. Eliceiri, and C. Mitchell, "In Vivo Adaptive Bayesian Regularized Lagrangian Carotid Strain Imaging for Murine Carotid Arteries and Its Associations With Histological Findings," *Ultrasound Med Biol,* vol. 49, no. 9, pp. 2103-2112, Sep, 2023.

[10] R. J. Dempsey, T. Varghese, D. C. Jackson, X. Wang, N. H. Meshram, C. C. Mitchell, B. P. Hermann, S. C. Johnson, S. E. Berman, and S. M. Wilbrand, "Carotid atherosclerotic plaque instability and cognition determined by ultrasound-measured plaque strain in asymptomatic patients with significant stenosis," *J Neurosurg,* vol. 128, no. 1, pp. 111-119, Jan, 2018.

[11] N. H. Meshram, and T. Varghese, "GPU Accelerated Multilevel Lagrangian Carotid Strain Imaging," *IEEE Trans Ultrason Ferroelectr Freq Control,* vol. 65, no. 8, pp. 1370-1379, Aug, 2018.

[12] N. H. Meshram, D. Jackson, T. Varghese, C. C. Mitchell, S. M. Wilbrand, R. J. Dempsey, and B. P. Hermann, "A Cross-Sectional Investigation of Cognition and Ultrasound-Based Vascular Strain Indices," *Arch Clin Neuropsychol,* vol. 35, no. 1, pp. 46-55, Jan 24, 2019.

[13] N. H. Meshram, C. C. Mitchell, S. M. Wilbrand, R. J. Dempsey, and T. Varghese, "In vivo carotid strain imaging using principal strains in longitudinal view," *Biomed Phys Eng Express,* vol. 5, no. 3, 2019.

[14] M. McCormick, N. Rubert, and T. Varghese, "Bayesian regularization applied to ultrasound strain imaging," *IEEE Trans Biomed Eng,* vol. 58, no. 6, pp. 1612-20, Jun, 2011.

[15] M. McCormick, T. Varghese, X. Wang, C. Mitchell, M. A. Kliewer, and R. J. Dempsey, "Methods for robust in vivo strain estimation in the carotid artery," *Phys Med Biol,* vol. 57, no. 22, pp. 7329-53, Nov 21, 2012.

[16] X. Wang, C. C. Mitchell, T. Varghese, D. C. Jackson, B. G. Rocque, B. P. Hermann, and R. J. Dempsey, "Improved Correlation of Strain Indices with Cognitive Dysfunction with Inclusion of Adventitial Layer with Carotid Plaque," *Ultrason Imaging,* vol. 38, no. 3, pp. 194-208, May, 2016.

[17] S. E. Berman, X. Wang, C. C. Mitchell, B. Kundu, D. C. Jackson, S. M. Wilbrand, T. Varghese, B. P. Hermann, H. A. Rowley, S. C. Johnson, and R. J. Dempsey, "The relationship between carotid artery plaque stability and white matter ischemic injury," *Neuroimage Clin,* vol. 9, pp. 216-22, 2015.

[18] N. D. Wong, M. J. Budoff, K. Ferdinand, I. M. Graham, E. D. Michos, T. Reddy, M. D. Shapiro, and P. P. Toth, "Atherosclerotic cardiovascular disease risk assessment: An American Society for Preventive Cardiology clinical practice statement," *Am J Prev Cardiol.,* vol. 10:100335, 2022.

[19] L. Breiman, "Random Forests," *Machine Learning,* vol. 45, no. 1, pp. 5-32, 2001.

[20] J. B. Lusk, E. C. O'Brien, B. G. Hammill, F. Li, B. Mac Grory, M. R. Patel, N. J. Pagidipati, and N. P. Shah, "Random Survival Forest Machine Learning for the Prediction of Cardiovascular Events Among Patients With a Measured Lipoprotein(a) Level: A Model Development Study," *Circ Genom Precis Med,* vol. 18, no. 1, pp. e004629, Feb, 2025.

[21] C. Z. Wu, L. Y. Huang, F. Y. Chen, C. H. Kuo, and D. F. Yeih, "Using Machine Learning to Predict Abnormal Carotid Intima-Media Thickness in Type 2 Diabetes," *Diagnostics (Basel),* vol. 13, no. 11, May 23, 2023.

[22] T. Chen, and C. Guestrin, *XGBoost: A Scalable Tree Boosting System*, 2016.

[23] S. F. Weng, J. Reps, J. Kai, J. M. Garibaldi, and N. Qureshi, "Can machine-learning improve cardiovascular risk prediction using routine clinical data?," *PLoS One,* vol. 12, no. 4, pp. e0174944, 2017.

[24] A. Ward, A. Sarraju, S. Chung, J. Li, R. Harrington, P. Heidenreich, L. Palaniappan, D. Scheinker, and F. Rodriguez, "Machine learning and atherosclerotic cardiovascular disease risk prediction in a multi-ethnic population," *NPJ Digit Med,* vol. 3, pp. 125, 2020.

[25] F. Commandeur, P. J. Slomka, M. Goeller, X. Chen, S. Cadet, A. Razipour, P. McElhinney, H. Gransar, S. Cantu, R. J. H. Miller, A. Rozanski, S. Achenbach, B. K. Tamarappoo, D. S. Berman, and D. Dey, "Machine learning to predict the long-term risk of myocardial infarction and cardiac death based on clinical risk, coronary calcium, and epicardial adipose tissue: a prospective study," *Cardiovasc Res,* vol. 116, no. 14, pp. 2216-2225, Dec 1, 2020.

[26] W. Hong, X. Zhou, S. Jin, Y. Lu, J. Pan, Q. Lin, S. Yang, T. Xu, Z. Basharat, M. Zippi, S. Fiorino, V. Tsukanov, S. Stock, A. Grottesi, and Q. Chen, "A Comparison of XGBoost, Random Forest, and Nomograph for the Prediction of Disease Severity in Patients With COVID-19 Pneumonia: Implications of Cytokine and Immune Cell Profile," *Front Cell Infect Microbiol,* vol. 12, pp. 819267, 2022.

[27] K. Davagdorj, V. H. Pham, N. Theera-Umpon, and K. H. Ryu, "XGBoost-Based Framework for Smoking-Induced Noncommunicable Disease Prediction," *Int J Environ Res Public Health,* vol. 17, no. 18, Sep 07, 2020.

[28] H. Shi, C. C. Mitchell, M. McCormick, M. A. Kliewer, R. J. Dempsey, and T. Varghese, "Preliminary in vivo atherosclerotic carotid plaque characterization using the accumulated axial strain and relative lateral shift strain indices," *Phys Med Biol,* vol. 53, no. 22, pp. 6377-94, Nov 21, 2008.

[29] D. C. Goff, D. M. Lloyd-Jones, G. Bennett, S. Coady, R. B. D'Agostino, R. Gibbons, P. Greenland, D. T. Lackland, D. Levy, C. J. O'Donnell, J. G. Robinson, J. S. Schwartz, S. T. Shero, S. C. Smith, P. Sorlie, N. J. Stone, P. W. Wilson, H. S. Jordan, L. Nevo, J. Wnek, J. L. Anderson, J. L. Halperin, N. M. Albert, B. Bozkurt, R. G. Brindis, L. H. Curtis, D. DeMets, J. S. Hochman, R. J. Kovacs, E. M. Ohman, S. J. Pressler, F. W. Sellke, W. K. Shen, G. F. Tomaselli, and A. C. o. C. A. H. A. T. F. o. P. Guidelines, "2013 ACC/AHA guideline on the assessment of cardiovascular risk: a report of the American College of Cardiology/American Heart Association Task Force on Practice Guidelines," *Circulation,* vol. 129, no. 25 Suppl 2, pp. S49-73, Jun 24, 2014.

[30] J. An, Y. Zhang, H. Zhou, M. Zhou, M. M. Safford, P. Muntner, A. E. Moran, and K. Reynolds, "Incidence of Atherosclerotic Cardiovascular Disease in Young Adults at Low Short-Term But High Long-Term Risk," *J Am Coll Cardiol,* vol. 81, no. 7, pp. 623-632, Feb 21, 2023.

[31] J. D. Berry, K. Liu, A. R. Folsom, C. E. Lewis, J. J. Carr, J. F. Polak, S. Shea, S. Sidney, D. H. O'Leary, C. Chan, and D. M. Lloyd-Jones, "Prevalence and progression of subclinical atherosclerosis in younger adults with low short-term but high lifetime estimated risk for

cardiovascular disease: the coronary artery risk development in young adults study and multi-ethnic study of atherosclerosis," *Circulation,* vol. 119, no. 3, pp. 382-9, Jan 27, 2009.

[32] A. K. Marma, J. D. Berry, H. Ning, S. D. Persell, and D. M. Lloyd-Jones, "Distribution of 10-year and lifetime predicted risks for cardiovascular disease in US adults: findings from the National Health and Nutrition Examination Survey 2003 to 2006," *Circ Cardiovasc Qual Outcomes,* vol. 3, no. 1, pp. 8-14, Jan, 2010.

[33] X. Wang, D. C. Jackson, C. C. Mitchell, T. Varghese, S. M. Wilbrand, B. G. Rocque, B. P. Hermann, and R. J. Dempsey, "Classification of Symptomatic and Asymptomatic Patients with and without Cognitive Decline Using Non-invasive Carotid Plaque Strain Indices as Biomarkers," *Ultrasound Med Biol,* vol. 42, no. 4, pp. 909-18, Apr, 2016.

[34] M. J. Kiernan, R. Al Mukaddim, C. C. Mitchell, J. Maybock, S. M. Wilbrand, R. J. Dempsey, and T. Varghese, "Lumen segmentation using a Mask R-CNN in carotid arteries with stenotic atherosclerotic plaque," *Ultrasonics,* vol. 137, pp. 107193, Feb, 2024.

[35] M. Kiernan, R. A. Mukaddim, C. Mitchell, J. Maybock, S. Wilbrand, R. Dempsey, and T. Varghese, *Utilizing a mask R-CNN for segmentation of the carotid lumen in subjects with plaque deposition*, p.^pp. MI: SPIE, 2024.

Chapter 8: Conclusions and Future Work

8.1 Summary

In Chapter 3 we developed and evaluated Mask R-CNN–based models for localizing and segmenting the carotid lumen (3.4.1) and atherosclerotic plaques (3.4.2). For lumen detection, a single-channel RF–derived B-mode model outperformed multi-channel variants (which incorporated SVD or MimickNet images), achieving a mean IoU of 0.84 for bounding boxes and 0.79 for segmentation—improving on past work (0.81/0.75) and showing only ~10 % overestimation in box area. Multi-channel approaches struggled when the jugular vein was prominent or under acoustic shadowing; incorporating MimickNet helped slightly but did not surpass B-mode alone. About 75.6 % of single-channel predictions met stringent acceptability criteria (≤10 % underestimation and ≤25 pixel midpoint error), whereas two- and three-channel models showed greater variability. We hypothesize that higher-frame-rate data and adaptive SVD filtering—or re-weighting channels during training—could enhance performance.

For plaque segmentation, nine independent Mask R-CNN models were compared by varying the maximum number of training and testing bounding boxes. Limiting predictions to two boxes at test time yielded the best mean Dice (0.64) and IoU (0.49) for segmentation, by reducing false positives when most images contain only one or two plaques. Combining model outputs into a consensus mask modestly improved Dice to 0.76 but still fell short of lumen segmentation accuracy, likely due to higher plaque variability in appearance.

Chapter 4 explored relationships between carotid intima-media thickness (IMT) and Lagrangian strain indices in 80 healthy volunteers (median age 35). We found no strong correlations between IMT and strain, suggesting these metrics assess distinct aspects of arterial health. IMT correlated

positively with traditional CVD risk factors (age, BMI, lipids, HbA1c), whereas axial, lateral, and shear strain showed the expected negative association with age and HbA1c while—counterintuitively—showing positive correlations with total cholesterol and BMI. We attribute these unexpected directions to the cohort's overall health (only 2.5 % had high cholesterol; 29 % overweight/obese vs. 73.6 % US average) and potential early arterial remodeling (increased compliance before later stiffening). We hypothesize that metabolic hormones (e.g., insulin, leptin) may enhance compliance in young adults. [1]

Building on Chapter 4, Chapter 5 repeated the strain analysis in 181 volunteers (median age 42). The larger sample resolved some prior anomalies: total cholesterol's correlation with strain weakened and flipped to the expected direction even though their relationship was no longer significant, though BMI–strain relationships remained inconsistent. As before, strain indices declined with age and rose with systolic blood pressure, indicating sensitivity to mechanical changes. We discussed that cohort healthiness (low visceral adiposity, subthreshold cholesterol) and non-linear vascular remodeling may underlie persistent BMI findings. [2, 3] We also proposed that fat distribution (visceral vs. subcutaneous) and unmeasured confounders (fitness, inflammation) [4] could moderate these associations, calling for longitudinal studies to map compliance trajectories over time.

In Chapter 6 we stratified 169 participants by carotid plaque presence, elevated HbA1c, and estimated 10-year cardiovascular risk (>5 %). Plaque-positive individuals (25 %) showed significantly lower axial and shear strain, older age, and higher lipids and HbA1c, confirming reduced compliance in atherosclerosis. Elevated HbA1c participants (17 %) also exhibited decreased strain but unlike the plaque group did not differ in lipids or blood pressure, suggesting hyperglycemia independently stiffens arteries with age as a major confounder. High-risk subjects

(27 %) similarly had markedly lower strain and elevated LDL, triglycerides, and HbA1c but stable HDL and hs-CRP, highlighting strain's promise as a biomarker of cumulative metabolic and age-related vascular changes. We noted an exponential decay of axial strain with age, minimal SBP variation across ages, and emphasized the need for balanced age-group representation and longitudinal analyses to disentangle age vs. disease effects.

Chapter 7 presented two XGBoost models: one for binary plaque presence, the other for continuous 10-year ASCVD risk. The plaque model achieved modest accuracy (mean $R^2 = 0.123$, Pearson $\rho = 0.374$) and correctly classified 82 % overall but only 50 % of true plaque cases—likely hampered by data imbalance and feature limitations. Age emerged as the top predictor, followed by shear strain. In contrast, the ASCVD risk model performed strongly ($R^2 = 0.658$, $\rho = 0.867$), reflecting the benefit of continuous targets and well-established risk factors. Here again age dominated feature importance; shear strain outranked axial and lateral measures. We conclude that while the ASCVD estimator is promising, the plaque classifier requires more balanced cohorts (including high-risk or symptomatic patients) and possibly ensemble or longitudinal approaches.

Across these chapters, we progressed from automated image-based vessel and plaque detection (Chapter 3) through biomechanical characterization of arterial health (Chapters 4–6) to predictive modeling of disease presence and risk (Chapter 7). Consistently, single-channel B-mode imaging and Lagrangian strain indices have shown strong utility for segmentation and risk assessment, while multi-channel imaging and plaque detection pose greater challenges. Our findings advocate for larger, more diverse cohorts; longitudinal designs; and integrated modeling to realize automated, strain-based tools for comprehensive cardiovascular risk stratification.

8.2 Follow-up Work

8.2.1 Lumen and Wall Segmentation

High-frame-rate and adaptive SVD filtering techniques will be used to reacquire carotid ultrasound data at ultrafast frame rates. Adaptive SVD filtering will be implemented to preserve lumen-wall contrast and plaque texture information. This approach aims to improve the performance of multi-channel R-CNN models while reducing false lumen-like anechoic regions that currently degrade SVD-based inputs. To further enhance model training, the dataset will be augmented with challenging cases, including poorly visualized carotid arteries, prominent jugular veins, and acoustic shadowing. This expansion will help multi-channel networks better distinguish carotid lumen from surrounding tissue and adjacent vessels. Additionally, channel weighting strategies will be introduced to address the negative impact of weaker SVD or MimickNet streams, such as loss weighting or attention mechanisms that emphasize the RF-derived B-mode channel during training. An automated approach for plaque ROI initialization will be developed by integrating lumen segmentation outputs to automatically determine plaque bounding boxes. This will enable downstream plaque segmentation without requiring manual box annotations. Moreover, the development of a modified Mask R-CNN will continue, aiming to jointly segment lumen and plaque by using lumen detections to constrain the plaque search space and improve localization accuracy.

8.2.2 Plaque Segmentation

To ensure comprehensive plaque detection, a diverse dataset will be collected, including carotid ultrasound sequences from patients exhibiting various plaque morphologies (near-wall, far-wall, calcified, mixed) and a broad range of disease severities. The optimal bounding box count will be systematically explored, evaluating training limits (1–5) with a larger dataset to balance false

positives and negatives. Dynamic adaptation of testing thresholds based on per-image model confidence will also be investigated. Consensus-based fusion techniques will be refined by incorporating per-model uncertainty estimates and weighted voting, aiming to reduce false positives while maintaining sensitivity to subtle plaques.

8.2.3. Lagrangian Strain and IMT Relationships

Prospective, longitudinal studies will be conducted to track carotid strain indices and IMT changes over time within the same subjects. This approach will help differentiate between early adaptive remodeling and progressive stiffening. The cohort will be balanced across age groups, with stratified representation based on BMI, cholesterol, and blood pressure to investigate potential non-linear associations and validate hypotheses related to early increased compliance. An expanded metabolic profiling protocol will be implemented, including markers such as inflammation, insulin, leptin, and visceral adiposity, to explore metabolic influences on observed strain-risk paradoxes.

8.2.4 Clinical Group Comparisons and Risk Stratification

Efforts will be made to achieve balanced subgroup populations, ensuring equal representation among individuals with conditions such as plaque/no-plaque, elevated/normal HbA1c, and high/low ASCVD risk groups within each age bracket. This will help control for age-related confounding factors. In addition to strain measurements, hemodynamic variables like pulse-wave velocity and central blood pressure will be included to assess how pressure gradients influence local wall strain.

8.2.5 Machine Learning for Plaque and Risk Prediction

To improve binary plaque prediction and risk generalization, the XGBoost training set will be enriched with data from patients presenting significant stenosis, post-CAS/CEA findings, and

higher ASCVD scores. Feature engineering will focus on including anthropometric data (e.g., visceral fat), laboratory metrics (e.g., inflammatory cytokines), and imaging characteristics (e.g., plaque echogenicity). To enhance predictive stability, ensemble and hybrid modeling approaches, such as stacking and boosting, will be evaluated. Longitudinal data will also be leveraged to forecast future strain declines, plaque progression, and clinical events, facilitating dynamic risk updates and proactive interventions.

This follow-up roadmap aims to build on current research by leveraging higher-quality data acquisition, enriched cohorts, advanced model fusion techniques, and thorough clinical validation. The ultimate goal is to develop robust, automated tools for assessing carotid health.

8.3 References

[1] J. B. Tryggestad, and K. R. Short, "Arterial compliance in obese children: implications for cardiovascular health," *Exerc Sport Sci Rev,* vol. 42, no. 4, pp. 175-82, Oct, 2014.

[2] J. Mao, S. Gan, S. Gong, Q. Zhou, F. Yu, H. Zhou, H. Lu, Q. Li, and Z. Deng, "Visceral fat area is more strongly associated with arterial stiffness than abdominal subcutaneous fat area in Chinese patients with type 2 diabetes," *Diabetol Metab Syndr,* vol. 16, no. 1, pp. 123, Jun 05, 2024.

[3] K. Sutton-Tyrrell, A. Newman, E. M. Simonsick, R. Havlik, M. Pahor, E. Lakatta, H. Spurgeon, and P. Vaitkevicius, "Aortic stiffness is associated with visceral adiposity in older adults enrolled in the study of health, aging, and body composition," *Hypertension,* vol. 38, no. 3, pp. 429-33, Sep, 2001.

[4] P. M. Ridker, M. V. Moorthy, N. R. Cook, N. Rifai, I. M. Lee, and J. E. Buring, "Inflammation, Cholesterol, Lipoprotein(a), and 30-Year Cardiovascular Outcomes in Women," *N Engl J Med,* vol. 391, no. 22, pp. 2087-2097, Dec 05, 2024.